Technical Physics Letters, Vol. 31, No. 2, 2005, pp. 101–102. Translated from Pis'ma v Zhurnal Tekhnicheskoĭ Fiziki, Vol. 31, No. 3, 2005, pp. 27–30.

Modeling Nonlinear High-Gradient Diffusion in Semiconductors

L. A. Kondrachenko[a], A. É. Rassadin[b], and A. S. Chistyakov[c]

[a] *Nizhni Novgorod State University, Nizhni Novgorod, Russia*
[b] *"Polet" Research and Production Corporation, Nizhni Novgorod, Russia*
[c] *NKS Company, Nizhni Novgorod, Russia*

Received August 5, 2004

Abstract—A nonlinear phenomenological equation is proposed for the description of shallow (≤1 μm) impurity diffusion in semiconductors and is solved by numerical methods. A comparison to the results of measurements of the diffusion of arsenic in silicon show good agreement between the proposed theory and experiment.

It is well known that the dopant concentration profiles obtained upon shallow diffusion of impurities in semiconductors (to a depth below 1 μm) significantly differ from the distributions predicted by solutions of the linear diffusion equation [1]. On the other hand, the dopant concentration profiles obtained in the early original experiments using diffusion from a constant source were described by the usual erfc function [2, 3]. The only distinction separating those experiments from later investigations consists in the depth of diffusion reached and the impurity concentration gradients employed. Therefore, it is reasonable to suggest that anomalous concentration profiles are at least partly related to the fact that, in the case of shallow diffusion, the thermodynamic system is far from the equilibrium state and the linear relations of the thermodynamics of irreversible processes [4] may fail to provide a correct quantitative description of the system. We believe that it would be natural to describe shallow diffusion of impurities in semiconductors in terms of a nonlinear theory taking into account the influence of the concentration gradient on the diffusion flux.

Let us expand the flux of a substance in terms of the concentration gradient. Taking into account the tensor dimension and restricting the expansion to the first nonzero term, we obtain [5]

$$\mathbf{J} = -D\nabla C - F(\nabla C)^3, \qquad (1)$$

where D is the diffusion coefficient, C is the concentration, and F is the coefficient of nonlinearity. As can be seen from this relation, the diffusion flux increases for $F > 0$ and decreases for $F < 0$.

In the absence of sources and sinks, the equation of continuity in the case of one-dimensional diffusion can be written as

$$\frac{\partial C}{\partial t} = \left[D + 3F\left(\frac{\partial C}{\partial x}\right)^2\right]\frac{\partial^2 C}{\partial x^2}, \qquad (2)$$

where the expression in square brackets can be considered as an effective diffusion coefficient, which tends to D as $\frac{\partial C}{\partial x} \longrightarrow 0$.

Since the exact solution to Eq. (2) is unknown, we have used numerical methods to study the behavior of this solution for the problem of diffusion from a constant source such that $C(0, t) = C_s$, $C(x, 0) = 0$, $x > 0$, and $t > 0$. The impurity concentration profiles calculated on a computer exhibit nonmonotonic character and tend to the erfc function with increasing diffusion time.

In experiments, the influence of the impurity concentration gradient can be revealed in a sufficiently large interval of diffusion times. At a relatively short annealing time (i.e., a small depth of diffusion), the nonlinear term gives a significant contribution that can be distinguished in comparison to the results obtained for a large time of diffusion at the same temperature and the same surface concentration of the impurity.

The experiments were performed in the Si–As system, where arsenic diffused from a surface oxide film into boron-doped single crystal silicon (KDB-0.005 grade). Subsequent layer-by-layer analysis of the arsenic concentration was performed using the standard sheet resistance technique for the diffusion time varied from five minutes to several hours and an annealing temperature of 1273 and 1423 K. The content of arsenic anhydride in the source corresponded to the surface concentration of arsenic on a level of about 10^{-20} cm^{-3}.

1063-7850/05/3102-0101$26.00 © 2005 Pleiades Publishing, Inc.

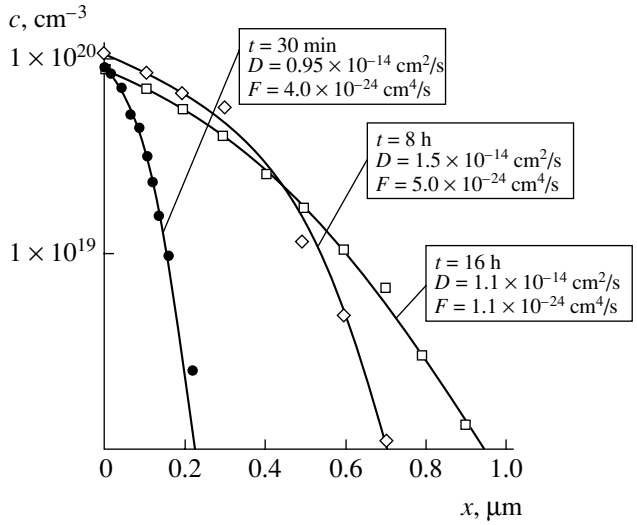

Arsenic concentration profiles upon diffusion in silicon at $T = 1273$ K for various times. Solid curves represent the numerical solutions of Eq. (2) calculated for the indicated values of D and F; points show the experimental data.

The choice of arsenic as the diffusant was related to the fact that (i) the ion radius of arsenic is almost equal to that of silicon and (ii) arsenic at a concentration of about 10^{-20} cm^{-3} exhibits no complexation, incomplete ionization, or other undesired effects [6, 7]. Under these conditions, it was possible to believe that any deviations from the linear behavior in our experiments were caused by the influence of the impurity concentration gradient.

The results of determination of the arsenic concentration profiles in silicon for an annealing temperature of $T = 1273$ K and three times of diffusion are presented in the figure, where solid curves represent the numerical solutions of Eq. (2) and points show the experimental data. The D and F values in the model equation were determined by fitting; the initial values of the diffusion coefficient were taken from the review [1]. As can be seen, the experimental points almost perfectly fit to the corresponding theoretical curves.

Using the well-known formula for the diffusion length, $l_D = 2\sqrt{Dt}$, we have estimated the effective diffusion coefficient given by the expression in square brackets in Eq. (2). It was found that this value exhibits an almost twofold decrease when the diffusion (annealing) time is increased from 30 min to 8 h. This behavior also agrees with the theory. The experimental results will be described in more detail in the subsequent publication.

To summarize, the preliminary results showed a good agreement of the theory and experiment and provided the first data on the coefficient of nonlinearity F, which has proved to be nonzero for the diffusion of arsenic in silicon.

REFERENCES

1. *Atomic Diffusion in Semiconductors*, Ed. by D. Shaw (Plenum Press, London, 1973).
2. C. S. Fuller and J. T. Ditzenberger, J. Appl. Phys. **27**, 544 (1956).
3. A. D. Kurtz and C. L. Gravel, J. Appl. Phys. **29**, 1456 (1958).
4. S. R. De Groot and P. Mazur, *Nonequilibrium Thermodynamics* (North-Holland, Amsterdam, 1962).
5. L. A. Kondrachenko, in *Proceedings of the 1st All-Union Seminar on Low-Temperature Doping of Semiconductors and Multilayer Structures for Microelectronics, Ustinov, 1987*, p. 28.
6. D. C. Deppe and N. Holonyack, J. Appl. Phys. **64**, R93 (1988).
7. E. Antoncik, Appl. Phys. A **58**, 117 (1994).

Translated by P. Pozdeev

Technical Physics Letters, Vol. 31, No. 2, 2005, pp. 103–105. Translated from Pis'ma v Zhurnal Tekhnicheskoĭ Fiziki, Vol. 31, No. 3, 2005, pp. 31–35.

A High-Power Low-Pressure Iodine Lamp Pumped by Glow Discharge

A. K. Shuaibov, I. A. Grabovaya, and L. L. Shimon

Uzhgorod National University, Uzhgorod, Ukraine

e-mail: ishev@univ.uzhgorod.ua

Received June 24, 2004

Abstract—We present the working characteristics of a high-power UV–VUV electric-discharge lamp filled with a working mixture of helium and iodine vapor (He–I_2) at a low pressure (0.1–1.5 kPa) and pumped by a dc glow discharge at a power of 15–200 W. The power of the total output UV radiation and the main emission peak at λ = 206.2 nm were studied as dependent on the electric power supplied to the glow discharge and on the partial pressure of helium in the He–I_2 mixture. The emission characteristics of the glow discharge plasma were studied in the spectral range from 200 to 350 nm. In this range, the lamp is operating predominantly on a resonance emission line of excited iodine atoms (λ = 206.2 nm, FWHM = 0.10–0.12 nm) and on a system of electronic-vibrational bands of excited iodine molecules with the main peak at λ = 342 nm. The contribution of the resonance emission due to excited iodine atoms to the total UV emission from the glow discharge plasma does not exceed 50%. The optimum partial pressure of helium is within 400–800 Pa. The total UV radiation power of the lamp operating in the optimum regime reaches 25 W at an efficiency of $\eta \le 15\%$. © *2005 Pleiades Publishing, Inc.*

Electric-discharge sources of spontaneous radiation in the ultraviolet (UV) and vacuum ultraviolet (VUV) spectral range, employing the emission from excited excimer molecules and halogen dimers, are of considerable interest for applications in microelectronics, high-energy chemistry, photobiology, and medicine [1–3]. The most powerful and effective sources of stationary or quasi-stationary emission from excimer molecules are offered by glow discharge and RF discharge plasmas in mixtures of inert gases with chlorine molecules [4, 5]. Unfortunately, the operating life of such lamps for a single portion of the working gas–vapor mixture does not exceed 50–100 h, which is related to a high chemical activity of chlorine with respect to electrodes and quartz shells of the discharge tubes. This situation stimulates investigations into the emission characteristics of glow-discharge plasmas in mixtures of inert gases with less reactive halogens such as iodine molecules. The lamps filled with iodine vapor and pumped by electrodeless RF or microwave discharge [6, 7] radiate predominantly in the region of a resonance atomic emission line of iodine at λ = 206.2 nm.

Previously, we studied a lamp filled with a Xe–I_2 mixture and pumped by dc glow discharge [8] and established that the contributions due to the emission at 253 nm [XeI(B–X)] and 342 nm [I_2(B–X)] account for not less than half of the total radiation power. The operating life of such iodine lamps pumped by dc glow discharge in a sealed-off regime reaches 300–1000 h [8, 9]. However, the conditions of formation of excited iodine atoms and molecules in He–I_2 mixtures ad their relative contributions to the total UV emission in a dc glow discharge supplied with a power of up to 200 W have not been studied so far.

This Letter presents the results of investigations aimed at optimization of the output characteristics of an electric-discharge UV lamp employing a low-pressure helium–iodine working mixture.

The dc glow discharge was initiated in a quartz discharge tube with an internal diameter of 14 mm and an interelectrode distance of 500 mm. The device was equipped with cylindrical electrodes made of nickel foil. High-purity crystalline iodine was contained in a special finger behind the anode.

The emission spectrum of glow discharge plasma was analyzed by a monochromator (MDR-2) and detected by a photomultiplier (FEU-106). The detector was calibrated with respect to the relative spectral sensitivity using standard lamps of the SI 8-200U and DVS-25 types covering the wavelength range λ = 200–1000 nm. The envelope of the resonance emission line of iodine atoms (λ = 206.2 nm) was studied using a holographic grating (2400 lines/mm). The discharge was power supplied from a high-voltage rectifier ($I_{ch} \le$ 80 mA; $U_{ch} \le$ 10 kV). Prior to being filled with a working gas–vapor mixture, the discharge tube was evacuated to a residual pressure of 5–10 Pa. The quartz tube was air-cooled by a ventilator, so that the temperature of the finger with iodine was close to room temperature. The tube temperature did not exceed 35–40°C, so that the saturated iodine pressure was within 130–200 Pa [10]. The total UV power was measured using a power meter of

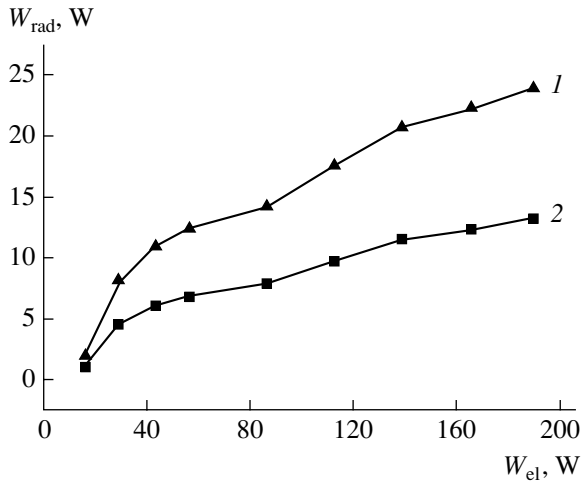

Fig. 1. The power of (*1*) the total output UV radiation and (*2*) the resonance atomic iodine emission line at 206.2 nm as a function of the electric power supplied to dc glow discharge in the He–I_2 lamp at P(He) = 400 Pa.

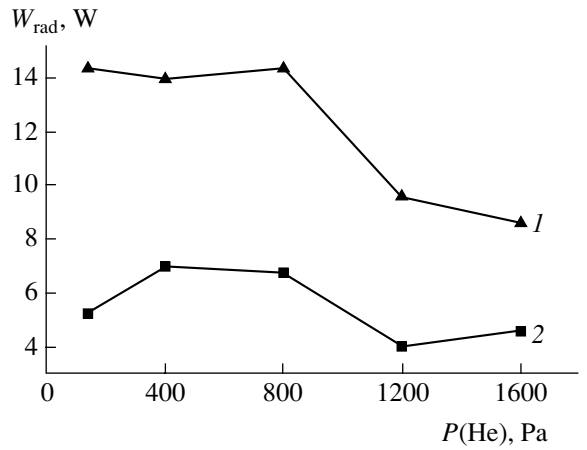

Fig. 2. The power of (*1*) the total output UV radiation and (*2*) the resonance atomic iodine emission line at 206.2 nm as a function of the partial pressure of helium in the working He–I_2 mixture.

the Quartz-01 type as described in [11]. The electric power supplied to the discharge was varied from 15 to 200 W. The current–voltage characteristics of the discharge corresponded to the subnormal and normal stages of dc glow discharge.

The emission spectrum of glow discharge plasma in a working mixture of helium with iodine vapor lamp consists of a narrow resonance emission line due to excited iodine atoms at 206.2 nm and a system of broad emission bands due to excited iodine molecules with the main peak at 342 nm. The total power of the output UV radiation is approximately equally distributed between the atomic emission line at 206.2 nm and the molecular emission band at 342 nm [I_2(B–X)]. The full width at half maximum (FWHM) of the emission line at 206.2 nm was within 0.10–0.12 nm, which is close to the width ($\Delta\lambda$ = 0.1 nm) of the iodine emission line at 253.8 nm observed for a low-pressure HgI lamp.

Figure 1 shows plots of the total output UV radiation power and the atomic iodine emission peak versus electric power supplied to dc glow discharge in a He–I_2 mixture at a partial helium pressure of P(He) = 400 Pa. As can be seen, the maximum increase in the output UV radiation power is achieved in the region of W_{el} = 15–50 W. Further increase in the supplied electric power was accompanied by an approximately linear growth in the output UV radiation power, without signs of saturation.

We have studied the output UV radiation power as a function of the partial pressure of helium in the working mixture. It was found that the optimum value of P(He) in the discharge, which ensured the maximum UV emission from excited iodine atoms, was 130 Pa. For the maximum UV emission from iodine molecules, the pressure of helium must be within 130–800 Pa (Fig. 2).

The absolute output UV radiation power via the side surface of the discharge tube measured in a spectral interval from 200 to 350 nm amounted to 15–25 W at an efficiency of $\eta \le 15\%$. The working life with respect to the UV emission in a gasostatic operation mode was not less than 400–500 h.

In conclusion, we have established that an electric-discharge lamp filled with a mixture of helium and iodine vapor at a low pressure radiates in the region of a resonance emission line of iodine atoms peaked at λ = 206.2 nm (FWHM ~ 0.1 nm) and a system of broad emission bands due to iodine molecules with the main maximum at 342 nm. The total power of the output UV radiation is approximately equally distributed between the atomic and molecular emission. The optimum partial pressure of helium in the discharge, which ensured the maximum UV emission from excited iodine atoms, is 130 Pa; for the maximum UV emission from iodine molecules, the pressure of helium must be within 130–800 Pa. The total output UV radiation power of the lamp reaches 25 W at an efficiency of $\eta \le 15\%$.

REFERENCES

1. I. W. Boyd and J.-Y. Zhang, Mater. Res. Soc. Symp. Proc. **617**, J4.4.1 (2000).
2. E. A. Sosnin, L. V. Lavrent'ev, Ya. V. Masterova, and V. F. Tarasenko, in *Modern Problems in Medicine and Biology: A Collection of Scientific Works* (Tomsk, 2003), Vol. 2, pp. 225–227 [in Russian].
3. E. A. Sosnin, L. V. Lavrent'ev, E. A. Kuznetsova, and M. V. Erofeev, in *Proceedings of the Regional Scientific–Practical Conference on Modern Problems and Achievements of Agricultural Science in Livestock Breeding, Plant Growing, and Economics (Dedicated to 10th Anni-*

versary of the Tomsk State Agricultural University), Tomsk, 2003, pp. 102–106.

4. M. I. Lomaev, V. S. Skakun, E. A. Sosnin, *et al.*, Usp. Fiz. Nauk **173**, 201 (2003) [Phys. Usp. **46**, 193 (2003)].
5. A. K. Shuaibov, A. I. Dashchenko, and I. V. Shevera, Fiz. Plazmy **30**, 475 (2004) [Plasma Phys. Rep. **30**, 437 (2004)].
6. U. Gross, A. Ubelis, P. Spietz, and J. Burrows, J. Phys. D **33**, 1588 (2000).
7. G. Revalde, J. Silinsh, A. Skudra, and J. Jansons, Proc. SPIE **4747**, 369 (2002).
8. A. K. Shuaibov, L. L. Shimon, and I. A. Grabovaya, Pis'ma Zh. Tekh. Fiz. **29** (20), 77 (2003) [Tech. Phys. Lett. **29**, 871 (2003)].
9. M. I. Lomaev and V. F. Tarasenko, Proc. SPIE **4747**, 390 (2002).
10. A. I. Efimov, L. P. Belorukova, I. V. Vasil'kova, and V. P. Chechev, *Properties of Inorganic Compounds: A Handbook* (Khimiya, Leningrad, 1983) [in Russian].
11. A. K. Shuaibov, L. L. Shimon, A. I. Dashchenko, and I. V. Shevera, Prib. Tekh. Éksp., No. 1, 104 (2002).

Translated by P. Pozdeev

Technical Physics Letters, Vol. 31, No. 2, 2005, pp. 106–107. Translated from Pis'ma v Zhurnal Tekhnicheskoĭ Fiziki, Vol. 31, No. 3, 2005, pp. 36–39.

Luminescence of Bulk and Thin-Film Single Crystals of Gadolinium Gallium Garnet Excited by UV Radiation

N. V. Vasil'eva, K. S. Gochelashvili, M. E. Zemskov, V. A. Kondratyuk, and V. V. Randoshkin

Institute of General Physics, Russian Academy of Sciences, Moscow, 117924 Russia

e-mail: natashav@ok.ru

Received June 15, 2004; in final form, September 1, 2004

Abstract—A difference between the luminescence spectra of bulk and thin-film single crystals of $Gd_3Ga_5O_{12}$ gadolinium gallium garnet excited by UV radiation from a deuterium lamp has been studied. The films were grown by liquid phase epitaxy from supercooled melts based on the $PbO–B_2O_3$ and $Bi_2O_3–B_2O_3$ solid solution systems. © *2005 Pleiades Publishing, Inc.*

Previously, we have reported [1–4] that the optical absorption spectra of the epitaxial films of $Gd_3Ga_5O_{12}$ gadolinium gallium garnet (GGG) exhibit additional bands in comparison to the spectra of bulk GGG single crystals. In particular, the films grown from a melt based on the $PbO–B_2O_3$ solid solution system at a small supercooling as compared to that for the GGG substrate were characterized by an additional absorption band centered at $\lambda = 280$ nm. The spectra of samples grown at a higher supercooling displayed two additional absorption bands peaked at $\lambda = 325$ and 550 nm. The GGG films grown from a $Bi_2O_3–B_2O_3$ solution melt exhibit an additional absorption band with a maximum at $\lambda = 280$ nm.

The aim of this study was to compare the effects of UV radiation on a bulk GGG single crystal and epitaxial films grown from $Gd_2O_3–Ga_2O_3–PbO–B_2O_3$ and $Gd_2O_3–Ga_2O_3–Bi_2O_3–B_2O_3$ solution melts on (111)-oriented GGG single crystal substrates with a thickness of 500 μm. The parameters of samples are presented in the table, where T_g is the growth temperature and $2h$ is the total thickness of epitaxial films grown on both sides of the substrate.

The samples were exposed to UV radiation of a deuterium lamp of the DDS-30 type. The light beam, which was passed through a quartz prism and a slit, was normally incident on the sample surface. The spectrum of exciting radiation is presented in Fig. 1. The edge face of the sample was close to the entrance slit of an MDR-12 monochromator. The width of the entrance slit was equal to the sample thickness. The sample luminescence was analyzed by the monochromator and detected by an FEU-100 photomultiplier with a working wavelength range of $\lambda = 170–840$ nm. The spectrum of emission from the sample edge was recorded using an ENDIM two-coordinate recorder with the sweep rate synchronized with the wavelength scan rate in the monochromator.

Figure 2 shows the typical UV-excited luminescence spectra observed from the GGG single crystal samples. The spectrum of a GGG substrate (Fig. 2, curve *0*) exhibits emission bands peaked at $\lambda = 590$, 591, 593, 618, 693, and 706 nm. These luminescence bands cannot be assigned to Gd^{3+} ions [5]. The nature of the optically active centers responsible for the observed emission is still unclear and requires additional investigation.

The above luminescence bands are not observed if the substrate surface is covered with an epitaxial film grown from either $Gd_2O_3–Ga_2O_3–PbO–B_2O_3$ (Fig. 2, curve *1*) or $Gd_2O_3–Ga_2O_3–Bi_2O_3–B_2O_3$ (Fig. 2, curve *2*) solution melts. The epitaxial film/substrate structures exhibit broad luminescence bands of low intensity

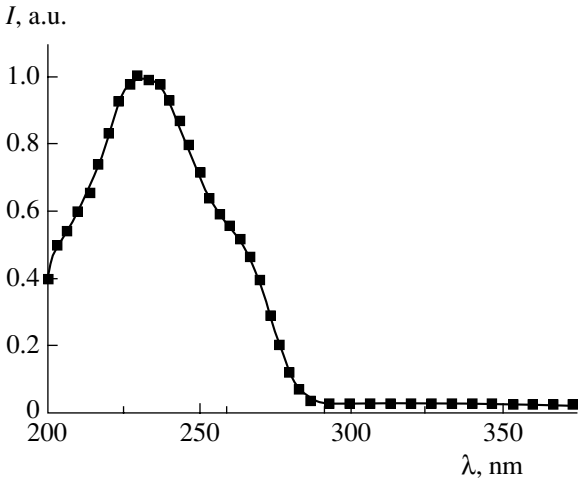

Fig. 1. The spectrum of UV radiation used to excite luminescence in the GGG samples.

1063-7850/05/3102-0106$26.00 © 2005 Pleiades Publishing, Inc.

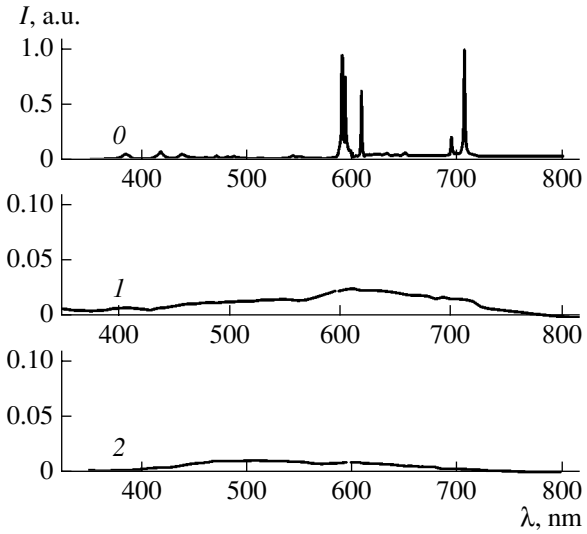

Fig. 2. The typical UV-excited luminescence spectra of a GGG substrate (curve *0*) and of the substrate surface covered with an epitaxial film grown from either Gd_2O_3–Ga_2O_3–PbO–B_2O_3 (curve *1*) or Gd_2O_3–Ga_2O_3–Bi_2O_3–B_2O_3 (curve *2*) solution melts.

(note that the ordinate scale for curve *0* is different from that for curves *1* and *2*). A difference between the luminescence spectra of the bulk substrate (Fig. 2, curve *0*) and the film/substrate structures (Fig. 2, curves *1* and *2*) can be explained only by the fact that the exciting radiation is completely absorbed by the epitaxial film.

Apparently, the exciting UV radiation is absorbed in the epitaxial film by the impurity ions of lead and bismuth, which are absent in the substrate. Moreover, the UV radiation is absorbed within a thin transition layer at the film/air interface, where the concentration of impurity ions is higher by a factor of ten and above as compared to that in the epitaxial film volume [6–8]. Thus, the observed luminescence (Fig. 2, curves *1* and *2*) is caused by the centers related to the impurity ions present in the epitaxial layer,

Parameters of epitaxial GGG films

Sample No.	Solvent	T_g, °C	$2h$, μm	Impurity
1	PbO–B_2O_3	966	10	Pb^{2+}
2	Bi_2O_3–B_2O_3	898	16	Bi^{3+}

The results of our experiments have to be taken into account in developing UV radiation imagers, scintillators for α and β radiation, and electro- and X-ray luminescent screens with high spatial resolution.

REFERENCES

1. V. V. Randoshkin, N. V. Vasil'eva, A. M. Saletskiĭ, *et al.*, Pis'ma Zh. Tekh. Fiz. **25** (17), 18 (1999) [Tech. Phys. Lett. **25**, 683 (1999)].
2. V. V. Randoshkin, N. V. Vasil'eva, A. V. Vasil'ev, *et al.*, Fiz. Tverd. Tela (St. Petersburg) **43**, 1594 (2001) [Phys. Solid State **43**, 1659 (2001)].
3. V. V. Randoshkin, N. V. Vasil'eva, V. G. Plotnichenko, *et al.*, Pis'ma Zh. Tekh. Fiz. **26** (10), 22 (2000) [Tech. Phys. Lett. **26**, 412 (2000)].
4. V. V. Randoshkin, N. V. Vasil'eva, V. G. Plotnichenko, *et al.*, Neorg. Mater. **40**, 1 (2004).
5. V. V. Randoshkin, N. V. Vasil'eva, V. G. Plotnichenko, *et al.*, Fiz. Tverd. Tela (St. Petersburg) **46**, 1001 (2004) [Phys. Solid State **46**, 1030 (2004)].
6. V. V. Randoshkin, A. N. Shaposhnikov, G. V. Shaposhnikova, and A. V. Shirkov, Pis'ma Zh. Tekh. Fiz. **10** (4), 224 (1984) [Sov. Tech. Phys. Lett. **10**, 93 (1984)].
7. N. A. Groshenko, A. M. Prokhorov, V. V. Randoshkin, *et al.*, Fiz. Tverd. Tela (Leningrad) **27**, 1712 (1985) [Sov. Phys. Solid State **27**, 1029 (1985)].
8. V. V. Randoshkin and A. Ya. Chervonenkis, *Applied Magnetooptics* (Énergoatomizdat, Moscow, 1990) [in Russian].

Translated by P. Pozdeev

Technical Physics Letters, Vol. 31, No. 2, 2005, pp. 108–111. Translated from Pis'ma v Zhurnal Tekhnicheskoĭ Fiziki, Vol. 31, No. 3, 2005, pp. 40–47.

Calculation of the Velocity of a Molecular Gas Slipping Round a Spherical Surface of Small Curvature

A. V. Latyshev, V. N. Popov*, and A. A. Yushkanov

Pomorskiĭ State University, Arkhangelsk, Russia

**e-mail: popov.vasily@pomorsu.ru*

Received June 18, 2004

Abstract—Exact analytical methods are applied to description of the thermal and isothermal slip of a molecular gas along a hard spherical surface with a relatively small curvature. The thermal and isothermal slip coefficients of the gas are determined in an approximation linear with respect to the Knudsen number. The problem is solved within the framework of the generalized Bhatnagar–Gross–Kruck (BGK) model of the Boltzmann kinetic equation taking into account the rotational degrees of freedom. The values of the thermal and isothermal slip coefficients have been numerically calculated for several molecular gases. It is shown that the obtained slip coefficients depend on the Prandtl number. *© 2005 Pleiades Publishing, Inc.*

Introduction. Description of the properties and behavior of molecular gases is basically more difficult than that of a monoatomic gas [1]. This difficulty is related to the fact that processes taking place in molecular gases have to be described taking into account not only translational movement of the molecules, but their rotational motion and vibrational degrees of freedom as well. The boundary conditions for the equations of hydrodynamics describing the regime of flow with slip in a monoatomic gas streamlining a curved surface have been studied in sufficient detail using both exact and approximate methods. The situation is not as satisfactory in the case of boundary conditions for the problem of the description of a molecular gas slipping round a curved surface. Exact analytical solutions of such problems have not been reported in open publications so far.

The aim of this study was to obtain exact analytical solutions to the problem of description of the thermal and isothermal slip of a molecular gas along a hard spherical surface with a relatively small curvature (for a Knudsen number on the order of 0.03–0.4). The approach is based on the Bhatnagar–Gross–Kruck (BGK) model of the Boltzmann kinetic equation generalized to the case of rotational degrees of freedom of the gas molecules [2]. It is assumed that the vibrational degrees of freedom are frozen, while the rotational motions are described based on the classical kinetic theory of gases. The results of calculations show that this approach to description of the behavior of molecular gases is valid in a sufficiently broad range of gas temperatures (approximately from 10 to 1000 K).

Formulation of the problem. Main equations. Consider a spherical aerosol particle suspended in a flow of a rarefied molecular gas and let a temperature gradient ∇T be set far from the particle surface. The collisions of molecules in the Knudsen layer (a thin boundary layer of gas immediately adjacent to the streamlined surface, with a thickness equal to the mean free path of the gas molecules) with the nonuniformly heated particle surface give rise to a macroscopic motion of gas along the surface, which is called thermal slip.

Let a spherical coordinate system be related to the center of curvature of the particle, with the polar axis oriented parallel to the temperature gradient. Then, owing to the axial symmetry of the system under consideration, the tangential component of the mass flow velocity U_θ will be nonzero. Since the spherical surface is impermeable, the radial component of the mass flow velocity of the gas on the surface is zero: $U_r|_S = 0$.

Let the tangential component of the gas flow vary slowly in the direction of the normal to the surface rather than remaining constant. This nonuniform mass flow velocity profile in the Knudsen layer leads to an additional slip of the gas along the surface, which is called isothermal slip.

Thus, the quantities $k_1 = \partial U_\theta/\partial r|_\infty$ and $k_2 = (1/R)(\partial \ln T/\partial\theta)|_\infty$ are nonzero in the problem under consideration. In what follows, these values are assumed to be small. In this case, the problems admits linearization, whereby the distribution of gas molecules with respect to coordinates and velocities can be represented as

$$f = f^{(0)}[1 + Y(\mathbf{r}, \mathbf{C}, \nu)],$$

where $f^{(0)}$ is the local equilibrium distribution function in the gas volume far from the aerosol particle surface; $\mathbf{r} = 3\sqrt{\pi}\,\mathrm{Pr}/(4\lambda)\mathbf{r}'$ (for the isothermal slip); $\mathbf{r} = \sqrt{\pi}\,\mathrm{Pr}/(2\lambda)\mathbf{r}'$ (for the thermal slip); $\mathbf{r}'$ is the dimensional radius vector; λ is the mean free path of gas molecules,

1063-7850/05/3102-0108$26.00 © 2005 Pleiades Publishing, Inc.

which is related to the kinematic viscosity by the relation $\lambda = \nu_g(\pi m/2k_BT_w)^{1/2}$; Pr is the Prandtl number; $\mathbf{C} = \mathbf{V}\sqrt{m/2k_BT_w}$; $\nu = \omega\sqrt{J/2k_BT_w}$; $\mathbf{v}$ and ω are the translational velocity and rotational frequency of the gas molecules, respectively; T_w is the particle (wall) surface; k_B is the Boltzmann constant; and m and J are the mass and the moment of inertia of a gas molecule, respectively.

Let $Y(\mathbf{r}, \mathbf{C}, \nu)$ be a solution of the equation [3]

$$C_r\frac{\partial Y}{\partial r} + Y(\mathbf{r}, \mathbf{C}, \nu) + k\Big[C_\theta\frac{\partial Y}{\partial\theta} + \frac{C_\varphi}{\sin\theta}\frac{\partial Y}{\partial\varphi} + (C_\theta^2 + C_\varphi^2)\frac{\partial Y}{\partial C_r} + (C_\varphi^2\cot\theta - C_rC_\theta)\frac{\partial Y}{\partial C_\theta} - (C_\varphi C_\theta\cot\theta + C_rC_\varphi)\frac{\partial Y}{\partial C_\varphi}\Big] = \int k(\mathbf{C}, \nu; \mathbf{C}', \nu')Y(\mathbf{r}, \mathbf{C}', \nu')d\Omega, \quad (1)$$

where $l = 2$ and $d\Omega = 2\pi^{-3/2}\exp(-C^2 - \nu^2)\nu d\nu d^3C$ for a diatomic gas; $l = 5/2$ and $d\Omega = \pi^{-3}\exp(-C^2 - \nu^2)d^3\nu d^3C$ for a polyatomic gas with $N \geq 3$ atoms in the molecule; $k = 4\mathrm{Kn}/(3\sqrt{\pi}\,\mathrm{Pr})$ for the isothermal slip; $k = 2\mathrm{Kn}/(\sqrt{\pi}\,\mathrm{Pr})$ for the thermal slip; $\mathrm{Kn} = \lambda/R'$ is the Knudsen number; R' is the dimensional radius of the aerosol particle; and

$$k(\mathbf{C}, \nu; \mathbf{C}', \nu') = 1 + 2\mathbf{C}\mathbf{C}' + \frac{1}{l + 1/2}(C^2 + \nu^2 - k - 1/2)(C'^2 + \nu'^2 - l - 1/2).$$

Following Sone [4], let us seek the function $Y(\mathbf{r}, \mathbf{C}, \nu)$ in the form of an expansion with respect to a small parameter k:

$$Y(\mathbf{r}, \mathbf{C}, \nu) = Y_1(\mathbf{r}, \mathbf{C}, \nu) + kY_2(\mathbf{r}, \mathbf{C}, \nu) + \ldots. \quad (2)$$

By the same token, the hydrodynamic characteristics of the gas flow are also expanded into series with respect to k. In particular, the tangential component of the mass flow velocity can be written as

$$U_\theta = U_\theta^{(1)} + kU_\theta^{(2)} + \ldots, \quad (3)$$

where $U = U'\sqrt{m/2k_BT_w}$ is the dimensionless mass flow velocity of the gas.

Substituting expression (2) into Eq. (1) and equating the coefficients at k, we eventually obtain the following equations for the functions $Y_1(\mathbf{r}, \mathbf{C}, \nu)$ and $Y_2(\mathbf{r}, \mathbf{C}, \nu)$:

$$C_r\frac{\partial Y_1}{\partial r} + Y_1(\mathbf{r}, \mathbf{C}, \nu) = \int k(\mathbf{C}, \nu; \mathbf{C}', \nu')Y_1(\mathbf{r}, \mathbf{C}', \nu')d\Omega, \quad (4)$$

$$C_r\frac{\partial Y_2}{\partial r} + Y_2(\mathbf{r}, \mathbf{C}, \nu) = \int k(\mathbf{C}, \nu; \mathbf{C}', \nu')Y_2(\mathbf{r}, \mathbf{C}', \nu')d\Omega - \Big[(C_\theta^2 + C_\varphi^2)\frac{\partial Y_1}{\partial C_r} + (C_\varphi^2\cot\theta - C_rC_\theta)\frac{\partial Y_1}{\partial C_\theta} - (C_\varphi C_\theta\cot\theta) + C_rC_\varphi)\frac{\partial Y_1}{\partial C_\varphi}\Big] - C_\theta\frac{\partial Y_1}{\partial\theta}. \quad (5)$$

Let us find a solution to Eqs. (4) and (5) in the form of the expansions

$$Y_1(\mathbf{r}, \mathbf{C}, \nu) = C_\theta\varphi_1(x, C_r) + C_\theta(C_\theta^2 + C_\varphi^2 + \nu^2 - l - 1)\varphi_2(x, C_r), \quad (6)$$

$$Y_2(\mathbf{r}, \mathbf{C}, \nu) = C_\theta\psi_1(x, C_r) + C_\theta(\nu^2 - l + 1)\psi_2(x, C_r) + \sum_{k=3}^{\infty} b_k(C_\theta, C_\varphi)\psi_k(x, C_r, \nu), \quad (7)$$

where $x = r - R$ and C_θ together with $b_k(C_\theta, C_\varphi)$ form a complete set of orthogonal polynomials in velocity space. To simplify the notation, we omit θ in the arguments of functions entering into $Y_1(\mathbf{r}, \mathbf{C}, \nu)$ and $Y_2(\mathbf{r}, \mathbf{C}, \nu)$. By the orthogonality of C_θ and $b_k(C_\theta, C_\varphi)$ in velocity space, we imply the zero of the integral

$$\int_{-\infty}^{\infty}\int_{-\infty}^{\infty}\exp(-C_\theta^2 - C_\varphi^2)C_\theta b_k(C_\theta, C_\varphi)dC_\theta dC_\varphi.$$

Substituting expressions (6) and (7) into Eqs. (4) and (5), multiplying the obtained relations by $\nu C_\theta\exp(-C_\theta^2 - C_\varphi^2 - \nu^2)$ for a diatomic gas ($C_\theta\exp(-C_\theta^2 - C_\varphi^2 - \nu^2)$ for a polyatomic gas), and integrating with respect to C_θ and C_φ from $-\infty$ to $+\infty$ and with respect to ν from 0 to $+\infty$ for the diatomic gas (C_θ and C_φ from $-\infty$ to $+\infty$, and ν from $-\infty$ to $+\infty$ for the polyatomic gas), we eventually arrive at the following

Slip coefficients of some molecular gases as functions of the Prandtl number

Gas	Pr	$C_m^{(0)}$	$C_m^{(1)}$	$K_{TS}^{(0)}$	β'
Cl_2	0.64	1.1945	1.1567	1.1436	2.3467
CO	0.74	1.0331	1.0004	1.0354	2.1247
CH_4	0.75	1.0193	0.9871	1.0216	2.0964
SO_2	0.85	0.8994	0.8709	0.9014	1.8498
NH_3	0.93	0.8220	0.7960	0.8239	1.6906
H_2O	1.01	1.7569	0.7330	0.7586	1.5567

set of equations for the functions $\varphi_i(x, \mu)$ and $\psi_i(x, \mu)$ ($i = 1, 2$; $\mu = C_r$):

$$\mu\frac{\partial\varphi_1}{\partial x} + \varphi_1(x, \mu) = \frac{1}{\sqrt{\pi}}\int_{-\infty}^{\infty}\exp(-\tau^2)\varphi_1(x, \tau)d\tau, \quad (8)$$

$$\mu\frac{\partial\varphi_2}{\partial x} + \varphi_2(x, \mu) = 0, \quad (9)$$

$$\mu\frac{\partial\psi_1}{\partial x} + \psi_1(x, \mu) = \frac{1}{\sqrt{\pi}}\int_{-\infty}^{\infty}\exp(-\tau^2)\psi_1(x, \tau)d\tau$$

$$+ \mu\varphi_1(x, \mu) - 2\frac{\partial\varphi_1}{\partial\mu} + 2\mu\varphi_2(x, \mu) - 4\frac{\partial\varphi_2}{\partial\mu}, \quad (10)$$

$$\mu\frac{\partial\psi_2}{\partial x} + \psi_2(x, \mu) = 4\mu\varphi_2(x, \mu) - 2\frac{\partial\varphi_2}{\partial\mu}.$$

Assuming that the gas molecules exhibit diffuse reflection from the aerosol particle surface and taking into account the relations

$$f^{(0)} = f^0\Big[1 + 2C_\theta U_\theta(\infty) + (C^2 - \nu^2 - l - 1/2)\tau(\infty)$$

$$-(C^2 - \nu^2 - l - 1/2)\left(C_r\frac{\partial\ln T}{\partial r} + \frac{C_\theta}{r}\frac{\partial\ln T}{\partial\theta}\right) - 2C_rC_\theta\frac{\partial U_\theta}{\partial r}\Big],$$

$$U_\theta(\infty) = U_\theta(0) + \frac{\partial U_\theta}{\partial r}(r - R),$$

$$\tau(\infty) = \varepsilon_T + \frac{\partial\ln T}{\partial r}(r - R) + \frac{\partial\ln T}{\partial\theta}\theta,$$

$$f^0 = \left(\frac{m}{2\pi k_B T_w}\right)^{3/2}\frac{J}{k_B T_w}\exp(-C^2 - \nu^2)$$

for the diatomic gas [3] and

$$f^0 = \left(\frac{m}{2\pi k_B T_w}\right)^{3/2}\frac{(J_1J_2J_3)^{1/2}}{(2\pi k_B T_w)^{3/2}}\exp(-C^2 - \nu^2)$$

for the polyatomic gas (J_1, J_2, J_3 are the projections of the moment of inertia of the gas molecules), we can write the boundary conditions for the unknown functions as

$$\varphi_1(0, \mu) = -2U_\theta^{(1)}\big|_S + 2\mu k_1 + \left(\mu^2 - \frac{1}{2}\right)k_2, \quad \mu > 0, \quad (11)$$

$$\varphi_1(\infty, \mu) = 0, \quad \mu < 0; \quad (12)$$

$$\varphi_2(0, \mu) = k_2, \quad \mu > 0, \quad \varphi_2(\infty, \mu) = 0, \quad \mu < 0, \quad (13)$$

$$\psi_1(0, \mu) = -2U_\theta^{(2)}\big|_S; \quad \mu > 0, \quad \psi_1(\infty, \mu) = 0, \quad \mu < 0; \quad (14)$$

$$\psi_2(0, \mu) = 0, \quad \mu > 0, \quad \psi_2(\infty, \mu) = 0, \quad \mu < 0.$$

Thus, the solution of the problem of description of the slip of a rarefied molecular gas along a relatively weakly curved surface reduces to the solution of the system of equations (8)–(10) with the boundary conditions (11)–(14).

Main results. The system of equations (8)–(10) with the boundary conditions (11)–(14) does not explicitly contain the rotational frequencies and fully coincides with an analogous set of equations and boundary conditions derived previously [5, 6] for the thermal and isothermal slip of a monoatomic gas at a spherical surface within the framework of the BGK model of the Boltzmann kinetic equation. Taking into account relation (3) and using the solution found in [5, 6], we obtain

$$U_\theta\big|_S = U_\theta^{(1)}\big|_S + kU_\theta^{(2)}\big|_S + \ldots,$$
$$U_\theta^{(1)}\big|_S = -Q_1k_1 - (Q_1 + 1/2)k_2/2, \quad (15)$$

$$U_\theta^{(2)}\big|_S = -k_1(Q_3 + Q_1Q_2)k_2. \quad (16)$$

where $Q_1 = -1.01619$, $Q_2 = -1.2663$, and $Q_3 = -1.8207$ are the Loyalka integrals [7].

Passing to the dimensional variables in expressions (15) and (16), we obtain [8]

$$U'_\theta\big|_S = 0.7645\mathrm{Pr}^{-1}\lambda(1 - 0.7403\mathrm{Pr}^{-1}\mathrm{Kn})\frac{\partial U'_\theta}{\partial r'}\bigg|_\infty$$
$$+ 0.7662\mathrm{Pr}^{-1}\nu_g(1 - 1.5723\mathrm{Pr}^{-1}\mathrm{Kn})\frac{\partial\ln T}{R'\partial\theta}\bigg|_\infty. \quad (17)$$

Thus, in the case when a molecular gas flow streamlines a spherical surface with slip, we have $C_m^{(0)} = 0.7645\mathrm{Pr}^{-1}$, $C_m^{(1)} = 0.7403\mathrm{Pr}^{-1}$, $K_{TS}^{(0)} = 0.7662\mathrm{Pr}^{-1}$, and $\beta' = 1.5723\mathrm{Pr}^{-1}$. The values of the slip coefficients for some molecular gases are presented in the table. Note that, in contrast, the monoatomic gases are characterized by the coefficients $C_m^{(0)} = 1.1466$, $C_m^{(1)} = 1.1104$,

$K_{TS}^{(0)} = 1.1499$, and $\beta' = 2.3590$ [5, 6], which are independent of the Prandtl number.

Conclusions. The thermal and isothermal slip coefficients for a rarefied molecular gas flowing with slip round a hard spherical surface have been obtained in an approximation linear with respect to the Knudsen number. It is found that, in contrast to the cases of temperature jump [2] and the second-order thermal slip [9], making allowance for the rotational degrees of freedom of the gas molecules within the framework of a model equation proposed in [3] leads to equations and boundary conditions describing the thermal and isothermal slip of the molecular gas along the curved surface, which are the same at those for a monoatomic gas. On the other hand, it is shown that the thermal and isothermal slip coefficients for the molecular gas significantly depend on the Prandtl number.

REFERENCES

1. V. M. Zhdanov and M. Ya. Alievskiĭ, *The Processes of Transfer and Relaxation in Molecular Gases* (Nauka, Moscow, 1989) [in Russian].
2. A. V. Latyshev and A. A. Yushkanov, Prikl. Mat. Mekh. **66**, 845 (2002).
3. A. V. Latyshev and A. A. Yushkanov, *Exact Solutions to Boundary-Value Problems for Molecular Gases*, Available from VINITI, No. 1725-V98.
4. Y. Sone, in *Proceedings of the 6th International Symposium on Rarefied Gas Dynamics* (Academic, New York, 1969), Vol. 1, pp. 243–253.
5. A. V. Latyshev, V. N. Popov, and A. A. Yushkanov, Sib. Zh. Industr. Mat. **5** (11), 103 (2002).
6. A. V. Latyshev, V. N. Popov, and A. A. Yushkanov, Poverkhnost, No. 6, 111 (2003).
7. S. K. Loyalka, Transp. Theory Stat. Phys. **4**, 55 (1975).
8. A. V. Latyshev, V. N. Popov, and A. A. Yushkanov, *Nonuniform Kinetic Problems: Method of Singular Integral Equation (A Monograph)* (Pomorsk. Univ., Arkhangelsk, 2004) [in Russian].
9. V. N. Popov, Pis'ma Zh. Tekh. Fiz. **28** (19), 10 (2002) [Tech. Phys. Lett. **28**, 800 (2002)].

Translated by P. Pozdeev

Technical Physics Letters, Vol. 31, No. 2, 2005, pp. 112–114. Translated from Pis'ma v Zhurnal Tekhnicheskoĭ Fiziki, Vol. 31, No. 3, 2005, pp. 48–54.

Long-Term Oscillatory Relaxation of Local Atomic Concentrations in Amorphous Magnets

S. K. Godovikov

Research Institute of Nuclear Physics, Moscow State University, Moscow, Russia

Received June 9, 2004

Abstract—It is established for the first time that iron-containing amorphous metal glasses feature an oscillatory process of local atomic migration with a characteristic time of up to several years. © *2005 Pleiades Publishing, Inc.*

Amorphous metal glasses offer a good model of atomic chaos in which, according to modern notions [1], a certain spatiotemporal order can spontaneously appear for some reason. However, no such phenomena have been previously reported for these materials. This study was undertaken in order to elucidate the situation.

The experiments were performed on samples of an iron-based ferromagnetically ordered amorphous alloy with the composition $Fe_{74}Si_{13}B_9Cu_1Nb_3$, which is widely used in electrical engineering. The samples were studied using ^{57}Fe Mössbauer spectroscopy, which is the most expedient method for probing the atomic structure of such materials. The initial perturbation of the ion subsystem was introduced by sharply changing the strength E of an electric field applied to a sample, which models a situation frequently encountered in real technical devices.

A sample was prepared from an amorphous metal ribbon with a thickness of 2×10^{-2} mm obtained by means of melt spinning. The ribbon was cut into pieces, which were glued onto a mylar film so as to obtain a Mössbauer absorber in the form of a disk with a diameter of 25 mm. The electrical impact on the sample was effected in a narrow gap (0.4 mm wide) of a capacitor to which a voltage of 25 kV was applied. The absorber, sandwiched between Teflon spacers, did not exhibit breakdown, but it was subject to a pulsed field variation at a rate of $dE/dt \sim 10^8$ kV/(cm s) when the capacitor plates were shorted. This impact caused an instantaneous displacement of metal ions from their equilibrium positions. Then, the state of the sample was monitored over a long period of time (about two years) by Mössbauer spectroscopy. Each spectrum was recorded for 2–5 h at $T = 293$ K.

Figures 1a and 1b show the typical Mössbauer spectra measured in the initial state and upon the electric impact, respectively. All the spectra measured during the two-year period of observations fall between these typical curves. The anticipated periodic variations with time have been actually observed, as manifested by oscillations between the two typical forms. The changes are most pronounced at the edges of the spectrum, especially on the left side, where an almost flat step (a) transforms into a peak (b) and vice versa.

In order to elucidate the physical meaning of these changes, the spectra were mathematically processed in

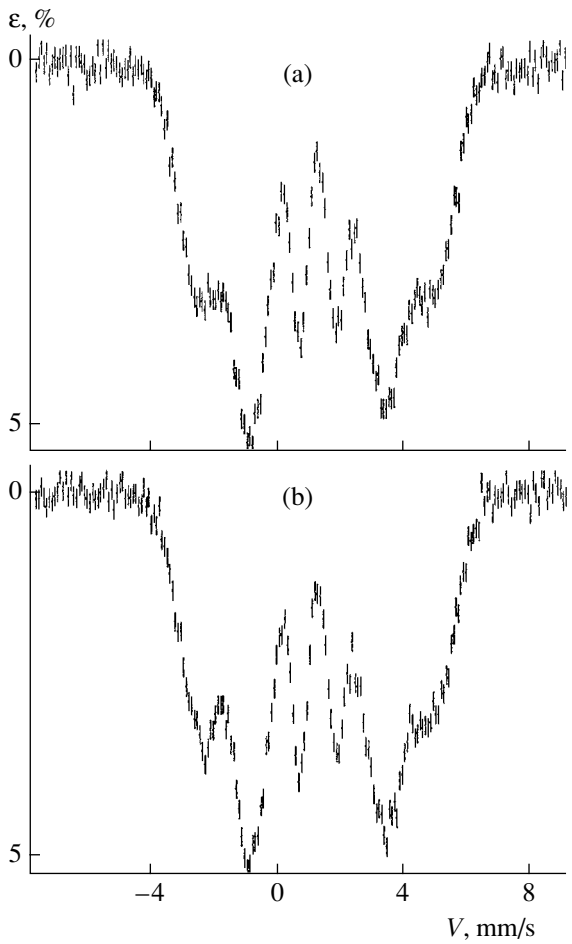

Fig. 1. Mössbauer spectra of a $Fe_{74}Si_{13}B_9Cu_1Nb_3$ amorphous alloy (a) in the initial state and (b) after an electric impact (ε is the relative response signal, V is the source velocity).

1063-7850/05/3102-0112$26.00 © 2005 Pleiades Publishing, Inc.

terms of two different models. Treatment within the framework of the model of a continuous distribution of hyperfine fields H gave the distribution density function $p(H)$, which exhibited peaks at ~100, 200, and 250 kOe on a broad symmetric background. This shape of the distribution was evidence of a certain concentration inhomogeneity and a short-range ordering in the given amorphous alloy. In order to perform an accurate quantitative analysis, the experimental data were processed (based on the established $p(H)$ distribution) within the framework of a discrete model of three Zeeman sextets consisting of arbitrarily wide (0.6–0.9 mm/s) Lorentz lines. Variable parameters were the hyperfine fields (H_1, H_2, H_3), isomer shifts, quadrupole splittings, and relative (percentage) weights of the three sextets (A_1, A_2, A_3). All of these parameters, except for A_1 and A_2, were rather stable in time. In contrast, the values of A_1 and A_2 exhibited opposite oscillations with a large difference in amplitude (up to 22%) and a variable period (from 8 to 16 days) (Fig. 2). The points of maximum mutual approach and divergence of curves *1* and *2* in Fig. 2 correspond to the spectra of types (a) and (b) in Fig. 1. These oscillations may be considered irregular or even stochastic, but the very fact of the existence of the two-parametric process is unambiguously established.

It was also found that these oscillations did not decay even after a one-year period of time, although their amplitude somewhat decreased as compared to that in Fig. 2. Repeated electric impact intensified the oscillations (increased their amplitude again), after which they were self-sustained for another year.

Amorphous metal alloys of the given composition have been thoroughly characterized by various methods, including Mössbauer spectroscopy [2, 3]. In particular, it was established that the hyperfine field parameter H is determined predominantly by the iron content and weakly depends on the metalloid type (Si vs. B). Local alloy compositions were found to correlate with the H values: H = 240–250 kOe corresponds to Fe_3(Si, B, Nb, Cu); $H \approx 100$ kOe corresponds to Fe_{68}(Si, B, Nb, Cu)$_{32}$; and $H_3 \approx 100$ kOe (Si, B, Nb, Cu) is evidence of a small iron content (~30 at. %). This study has also revealed three regions of a short-range order, which can be denoted I–III and correspond to the aforementioned compositions. Region III is characterized by a high structural stability, whereas regions I and II are extremely unstable and mobile. All of these regions have dimensions on the order of several dozens of ångströms.

In order to clarify the physical essence of these relaxation processes, it is necessary to distinguish between the magnetic and atomic phenomena. The stability of the H_1, H_2, and H_3 values indicates that the temporal variations in the local collinear ferromagnetic structure of regions I and II are insignificant. Therefore, the observed dynamics can be related only to the atomic migration leading to oscillations in the local composition. An analysis of the ion radii [4] and atomic masses for elements present in the alloy composition leads to a natural assumption that this migration most probably involves small and light boron ions. It is known [5] that amorphous metal alloys contain a large number of vacancies, so that boron diffusion may proceed via these lattice sites (as in crystalline α-Fe) rather than via interstitial positions.

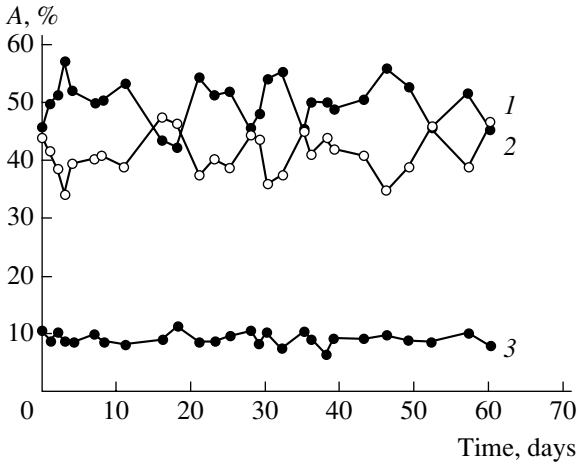

Fig. 2. Long-term variation of the relative weights of three sextets (components of a model Mössbauer spectrum) for an amorphous alloy sample upon electric impact: (*1*) A_1; (*2*) A_2; (*3*) A_3. Experimental errors fall within the circle size.

The clear opposite character of variation of the A_1 and A_2 values suggests the following model of the observed local oscillatory process. In the initial state, the content of regions I and II is approximately the same (about 45%). Electric impact induces an immediate displacement of ions and the corresponding redistribution of pressures at the atomic positions. As a result, boron ions leave some regions II, and this process continues until the concentration of nonmagnetic components in these regions becomes identical to that in regions I. This implies a relative increase in the amount of regions I and the corresponding decrease in the proportion of regions II. As can be seen from the data in Fig. 2, on the fourth day this process involves about 1/4 of regions II. Boron ions do not enter regions I or III and, probably, form associates with each other and with other nonmagnetic ions (invisible for the Mössbauer effect). The resulting strong concentrational inhomogeneity is unstable, and the opposite process gradually develops, whereby boron ions return to regions II, and this cycle is completed after about 15 days (Fig. 2). This model may, in principle, be expanded to include regions I, which will initially accommodate the excess boron ions.

The observed structural relaxation is not terminated upon the first cycle, since the driving force—the elastic and magnetoelastic energy introduced into the amorphous alloy during its rapid quenching from melt and

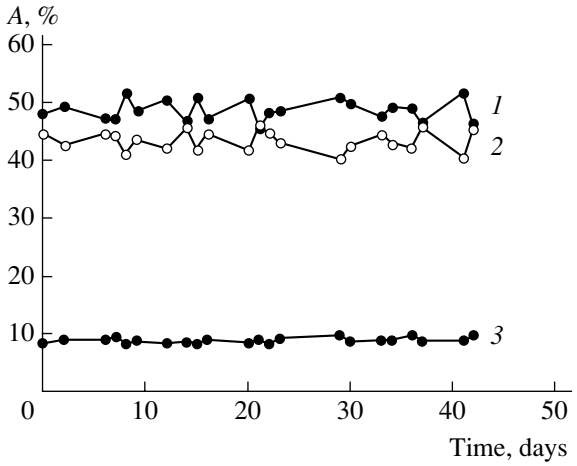

Fig. 3. Long-term variation of the relative weights of three sextets (components of a model Mössbauer spectrum) for an amorphous alloy sample not subjected to electric impact: (*1*) A_1; (*2*) A_2; (*3*) A_3. Experimental errors fall within the circle size.

then during the electric impact—is far from being exhausted. As a result, we observe long-term oscillations of the parameter of local atomic concentrations that can be terminated only by complete ordering of the sample, that is, by crystallization. Any external action producing displacement of ions favors intensification of this oscillatory process. Analogous phenomena were previously observed in a $TbFe_2$ crystal with nonmagnetic impurities [6], which also exhibited oscillations in the local magnetic structure.

In order to elucidate the nature of the observed phenomenon, the same measurements were performed on a sample not subjected to the electric impact. Figure 3 shows the results of the determination of parameters A_1, A_2, and A_3 for the first 40 days. It was found that the opposite changes in A_1 and A_2 are also observed for this sample, but their amplitude is less than half of that for the sample studied upon the electric impact (Fig. 2). This rather unexpected result shows that the process of long-term oscillatory relaxation is inherent in the amorphous alloy from the very beginning and that the electric impact only potentiates the effect.

Thus, the results of this investigation showed that amorphous metal alloys may exhibit structural relaxation at T = 293 K, which has the form of long-term oscillations of the parameter of local atomic concentrations. The amplitude of this process can be increased by an impact action of an external electric field.

Acknowledgments. The author is grateful to E.V. Voronina for her help in data processing.

REFERENCES

1. I. Prigogine and I. Stengers, *Order Out of Chaos: Man's New Dialogue with Nature* (Heinemann, London, 1984).
2. V. A. Makarov, M. A. Artsishevskiĭ, Yu. V. Baldokhin, *et al.*, Fiz. Met. Metalloved., No. 9, 139 (1991).
3. M. Taniwaki and M. Maeda, Mater. Sci. Eng. **99**, 47 (1988).
4. V. S. Urusov, *Energy Crystal Chemistry* (Nauka, Moscow, 1975).
5. H. J. Güntherodt and H. Beck, *Glassy Metals* (Springer-Verlag, Berlin, 1981).
6. S. K. Godovikov, Izv. Ross. Akad. Nauk, Ser. Fiz. **67**, 1000 (2003).

Translated by P. Pozdeev

Technical Physics Letters, Vol. 31, No. 2, 2005, pp. 115–116. Translated from Pis'ma v Zhurnal Tekhnicheskoĭ Fiziki, Vol. 31, No. 3, 2005, pp. 55–59.

Silicon Passivated by Insulating Erbium Oxide Films

M. A. Rodionov and V. A. Rozhkov*

Samara State University, Samara, Russia

**e-mail: rozhkov@ssu.samara.ru*

Received July 27, 2004; in final form, September 17, 2004

Abstract—The recombination properties of silicon passivated by insulating films of erbium oxide (Er_2O_3) have been studied. After deposition of an oxide film, the effective lifetime of nonequilibrium charge carriers, measured by method of nonstationary photoconductivity relaxation, increased by a factor of two to three as compared to the initial value. The rates of the surface recombination of charge carriers at the silicon–oxide interface have been determined. The insulating films of erbium oxide are promising passivating coatings for silicon-based devices and integrations. © *2005 Pleiades Publishing, Inc.*

Rare earth (RE) oxides are among the promising dielectric materials suitable for the formation of antireflection coatings on silicon-based photovoltaic devices. The RE oxides are advantageous over other candidate materials because they are highly transparent in the working spectral range, show high chemical and thermal stability, and possess an optimum index of refraction for these applications. The results of previous investigations [1, 2] showed that RE oxide films deposited onto the surface of silicon reduce the spectral reflection coefficient to 0.01–1.2% and increase the spectral short-circuit photocurrent of a photoelectric converter by more than 50%.

An important requirement for the optical coatings of semiconductor devices is the possibility of obtaining semiconductor–film interfaces characterized by low recombination losses. Investigation of the passivating properties of a series of RE oxides [3] (RE = Ce, Eu, Dy, Sm, Y, Gd, Yb) obtained by thermal oxidation of the corresponding RE element films for 30 min in air at 673 K showed that the surface recombination rate on the passivated silicon surface significantly decreased. The dependence of the lifetime of nonequilibrium charge carriers in silicon on the temperature of passivating heat treatment for RE = Y, Dy, and Gd was studied in [4]. Another promising coating for passivation of the surface of silicon and related devices is offered by a two-layer structure of ytterbium and dysprosium oxides [5].

The recombination characteristics of a silicon surface covered by a layer of erbium oxide have not been studied so far. In order to fill this gap, we have determined the effective lifetime and the rate of surface recombination of nonequilibrium charge carriers in silicon plates passivated by erbium oxide films.

The substrates were cut from (100)-oriented polished single crystal silicon wafers (KEF-20 grade) and had the dimensions $10 \times 5 \times 0.36$ mm. Prior to RE oxide film formation, a part of the silicon substrates were only rinsed for 10 min in acetone, while the other samples were deprived of natural oxide by etching in an aqueous solution of hydrofluoric acid ($HF–H_2O$, 1 : 10), and some of these samples were then boiled in a hydrogen peroxide–ammonia–water mixture ($NH_4OH–H_2O_2–H_2O$, 1 : 1 : 3). After each treatment, the substrates were repeatedly rinsed in doubly distilled water and dried on a filter paper. Then, the films of erbium were prepared on both sides of silicon substrates by thermal deposition in vacuum. The RE metals were evaporated from a molybdenum crucible in a residual vacuum of $(2–3) \times 10^{-5}$ Torr (VUP-5 vacuum system). Finally, the RE metal films were oxidized by heating in air for 40 min at 600°C, and the ohmic contacts were formed by vacuum deposition of dysprosium and aluminum pads via masks (see inset to the figure).

The effective lifetime τ_{ef} of charge carriers was determined by the conventional method of nonstation-

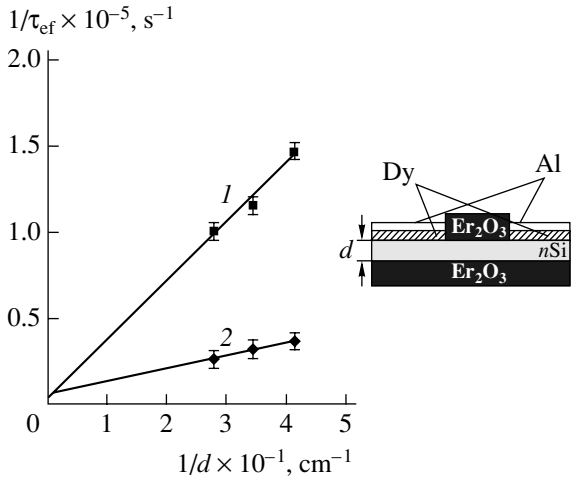

Plots of the effective lifetime of nonequilibrium charge carriers versus thickness of silicon samples (*1*) with a real surface and (*2*) passivated with erbium oxide film. The inset shows a sample configuration.

1063-7850/05/3102-0115$26.00

Effective lifetimes τ_{ef} and surface recombination rates S of nonequilibrium charge carriers in silicon samples differently treated before and after passivation by erbium oxide films

Silicon surface pretreatment	τ_{ef}, μs		S, cm/s	
	without Er_2O_3	with Er_2O_3	without Er_2O_3	with Er_2O_3
Ultrasonic rinsing	10–12	25–30	1500–1800	600–720
HF:H_2O	8–10	20–25	1800–2250	720–900
HF:H_2O + H_2O_2	10–12	31–38	1500–1800	470–580

ary photoconductivity on the samples illuminated by rectangular pulses of light. The method of measurements and the experimental setup were described elsewhere [6]. It was found that the process of photoconductivity relaxation in the samples can be described by a single exponent with one characteristic time. This process is determined entirely by the carrier generation–relaxation processes, while the trapping of nonequilibrium carriers at the silicon–RE oxide interfaces can be ignored. The effective lifetime of nonequilibrium charge carriers in thin samples with a relatively low rate of the surface recombination is described by the relation [7]

$$\frac{1}{\tau_{ef}} = \frac{1}{\tau_0} + \frac{2S}{d},$$

where τ_0 is the lifetime of nonequilibrium charge carriers in the bulk of silicon, d is the sample thickness, and S is the surface recombination rate. Using this equation, the surface recombination rate can be evaluated from the photoconductivity kinetics if the bulk carrier lifetime is known.

For determining the bulk carrier lifetime, we used the dependence of the effective lifetime of nonequilibrium charge carriers on the sample thickness. Two such plots, constructed using the τ_{ef} values measured for the samples of various thickness prepared by etching silicon substrates in a standard etchant (SR-8), are presented in the figure. As can be seen, the experimental data are well rectified in the $1/\tau_{ef}$ versus $1/d$ coordinates. This result is indicative of a constant rate of surface recombination in the samples of various thicknesses. The bulk carrier lifetimes evaluated from these experimental data were $\tau_0 \geq 200$ μs for all samples studied.

The surface recombination rate was evaluated using measured values of the effective lifetime of nonequilibrium charge carriers. The measured values of τ_{ef} did not exceed 38 μs and obeyed the condition $1/\tau_{ef} \gg 1/\tau_0$, which allowed the term $1/\tau_0$ in relation (1) to be ignored. The values of the surface recombination rate S and effective lifetime τ_{ef} of nonequilibrium charge carriers determined for differently pretreated silicon samples measured before and after the erbium oxide film formation are presented in the table.

An analysis of the results shows that deposition of the erbium oxide films increases the effective lifetime of nonequilibrium charge carriers and decreases the surface recombination rate. As can be seen from the comparative data, the S values in the Si–Er_2O_3 structure are lower by one to two orders of magnitude than the analogous values in Si–SiO_2 and Si–SiO_2–Si_3N_4 structures widely used in semiconductor electronics [8, 9].

Thus, the results of our investigation show the high efficiency and good prospects of using insulating erbium oxide films as passivating coatings for silicon-based devices and elements of integrated circuits.

REFERENCES

1. Yu. A. Anoshin, A. I. Petrov, V. A. Rozhkov, *et al.*, Pis'ma Zh. Tekh. Fiz. **18** (10), 54 (1992) [Sov. Tech. Phys. Lett. **18**, 321 (1992)].
2. V. A. Rozhkov and A. I. Petrov, Izv. Vyssh. Uchebn. Zaved., Fiz., No. 7, 99 (1994).
3. A. I. Petrov and V. A. Rozhkov, Pis'ma Zh. Tekh. Fiz. **24** (7), 16 (1998) [Tech. Phys. Lett. **24**, 254 (1998)].
4. V. A. Rozhkov and A. I. Petrov, Fizika Volnovykh Protsessov i Radiotekhnicheskie Sistemy **2**, 69 (1999).
5. M. A. Rodionov, V. A. Rozhkov, and A. V. Pashin, Pis'ma Zh. Tekh. Fiz. **30** (12), 56 (2004) [Tech. Phys. Lett. **30**, 512 (2004)].
6. V. A. Rozhkov and M. A. Rodionov, in *Proceedings of the 2nd International Scientific–Technological Conference "Physics and Technical Applications of Wave Processes," Samara, 2003*, pp. 358–361.
7. A. V. Rzhanov, *Electron Processes on Semiconductor Surfaces* (Nauka, Moscow, 1971) [in Russian].
8. V. G. Litovchenko and A. P. Gorban', *Principles of the Theory of Microelectronic MIS Systems* (Naukova Dumka, Kiev, 1978) [in Russian].
9. A. V. Sachenko, B. A. Novominskiĭ, and A. S. Kalshabekov, in *Proceedings of the 12th All-Union Scientific Conference on Microelectronics, Tbilisi, 1987*, Part 3, p. 143.

Translated by P. Pozdeev

Technical Physics Letters, Vol. 31, No. 2, 2005, pp. 117–119. Translated from Pis'ma v Zhurnal Tekhnicheskoĭ Fiziki, Vol. 31, No. 3, 2005, pp. 60–66.

Time Shift between Unstable Periodic Orbits of Coupled Chaotic Oscillators

A. A. Koronovskiĭ*, M. K. Kurovskaya, and A. E. Hramov,[1]**

State Scientific Center "College," Saratov State University, Saratov, Russia

*e-mail: * alkor@cas.ssu.runnet.ru; ** aeh@cas.ssu.runnet.ru*

Received September 7, 2004

Abstract—The shift Δt between unstable periodic orbits of coupled oscillators occurring in the chaotic synchronization regime has been studied. It is shown that this time shift is the same for all equiphase orbits with various topological parameters and depends on the coupling parameter ε. This dependence obeys the universal power law $\Delta t \sim \varepsilon^n$ with an exponent of $n = -1$. © *2005 Pleiades Publishing, Inc.*

Chaotic synchronization of dynamical systems is among the important basic phenomena extensively studied in recent years [1]. This process is also of considerable practical interest (e.g., for data transfer by means of deterministic chaotic oscillations [2], for solving some problems in biology [3], etc.). According to modern classification, there are several types of chaotic synchronization of coupled oscillators, including generalized, phase, lag, and complete synchronization (see, e.g., [4]). Recently, it has been shown [5, 6] that the phase, generalized, lag, and complete synchronization regimes are closely related, since they are essentially manifestations of the same type of synchronous dynamics referred to as time scale synchronization. The character of a particular synchronous regime (phase, lag, or complete) is determined by the number of synchronized time scales introduced by means of a continuous wavelet transform [7].

In this Letter, we will analyze how the time shift between synchronized unstable saddle periodic orbits (corresponding to the equiphase saddle m:m cycles in the general phase space) changes in the phase spaces of interacting chaotic oscillators depending on the parameter of coupling between the interacting subsystems.

Unstable saddle periodic orbits [8] play an important role in the process of chaotic synchronization (see, e.g., [9–11]). An autonomous chaotic oscillator is characterized by a set of unstable saddle periodic orbits of various periods, which are incorporated into the chaotic attractor. For a small coupling parameter, each of the two mutually coupled chaotic oscillators with slightly different parameters is characterized by its own set of unstable saddle orbits. The saddle orbits with the same topological period m have different temporal periods T (the time required for the imaging point to return to a fixed point of the orbit) and the corresponding different frequencies. Accordingly, unstable two-dimensional toruses exist in the complete phase space formed by the partial phase spaces of the interacting oscillators.

The onset of phase synchronization is accompanied by trapping of the frequencies of unstable periodic orbits (for more detail, see [12]) and by the appearance of resonance saddle cycles (either equiphase or not) on the two-dimensional toruses. It was shown [12] that only equiphase resonance saddle m:n cycles (where m, $n = 1, 2, \ldots$) exist in a broad range of variation of the coupling parameter, including the regions of phase synchronization and lag synchronization. All other resonance saddle cycles (including nonequiphase m:m cycles) exist in a relatively small interval of the coupling parameter and break when this parameter approaches a threshold of the lag synchronization.

There is still an open question concerning the behavior of a time shift between saddle orbits of the partial systems forming a resonance cycle in the general phase space. The interest in answering this question has been inspired by the results obtained recently [13] in the study of a phase shift between synchronized spectral components of interacting chaotic oscillators.

In the regime of lag synchronization, whereby the state vector of one of the two coupled systems has a certain time lag relative to the state vector of another system, $\mathbf{x}_1(t) \approx \mathbf{x}_2(t + \Delta t)$, the time shift between the saddle cycles with topological periods m in the coupled systems (corresponding to an equiphase resonance m:m cycle in the general phase space) also proves to be Δt. However, it is still unclear how this time shift behaves in the regime of phased synchronization.

In order to analyze this problem, let us consider two mutually coupled Rössler systems occurring in the

[1] This author has also appeared under the alternate spelling A.E. Khramov.

1063-7850/05/3102-0117$26.00 © 2005 Pleiades Publishing, Inc.

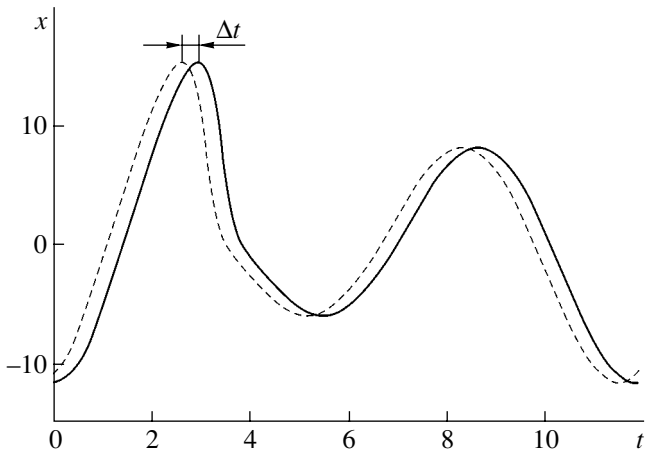

Fig. 1. Time series corresponding to an equiphase resonance saddle *m*:*m* cycle with a topological period of $m = 2$ for a coupling parameter of $\varepsilon = 0.07$ corresponding to a phase synchronization regime. The solid and dashed curves show the saddle orbits in the first and second system, respectively.

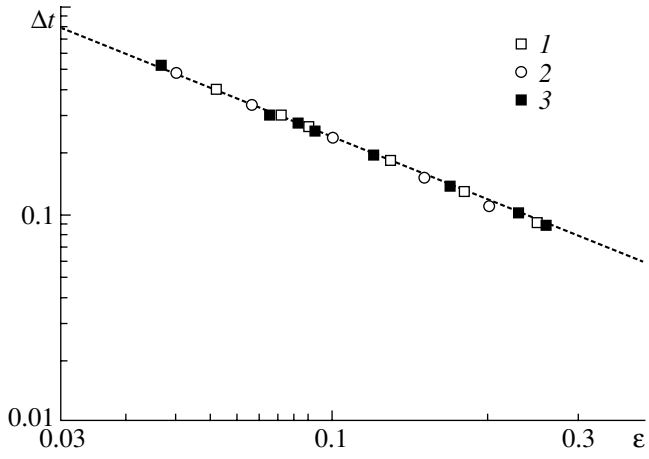

Fig. 2. A double logarithmic plot of the time shift Δt between synchronized saddle periodic orbits versus the coupling parameter ε of coupled Rössler systems (1), for the orbits with the topological periods $m = 1$ (*1*), 2 (*2*), and 3 (*3*). The dashed line corresponds to power law (2) with an exponent of $n = -1$.

dynamical chaos regime:

$$\begin{aligned} \dot{x}_{1,2} &= -\omega_{1,2}y_{1,2} - z_{1,2} + \varepsilon(x_{2,1} - x_{1,2}), \\ \dot{y}_{1,2} &= \omega_{1,2}x_{1,2} + ay_{1,2} + \varepsilon(y_{2,1} - y_{1,2}), \\ \dot{z}_{1,2} &= p + z_{1,2}(x_{1,2} - c), \end{aligned} \tag{1}$$

where ε is the coupling parameter, $\omega_1 = 0.98$, and $\omega_2 = 1.03$. The values of other control parameters were selected as follows: $a = 0.22$, $p = 0.1$, and $c = 8.5$. It is known [14] that two coupled Rössler systems (1) with $0.04 \lesssim \varepsilon \lesssim 0.14$ occur in the regime of phase synchronization; for $\varepsilon > 0.14$, the same systems exhibit lag synchronization.

We have considered equiphase unstable saddle periodic orbits with topological periods, incorporated into chaotic attractors of the interacting chaotic oscillators. The system of equations (1) was numerically integrated using the fourth-order Runge–Kutta method. Unstable saddle periodic orbits were separated using the *SD* method as described by Schmelcher *et al.* [15, 16]. In order to study the time shift between the unstable periodic cycles, it is necessary to find synchronized orbits simultaneously in both coupled systems. For this reason, the *SD* method was applied in a six-dimensional phase space formed by the partial three-dimensional phase spaces of the interacting Rössler oscillators.

Figure 1 shows the time series $x_{1,2}(t)$ corresponding to a saddle equiphase resonance *m*:*m* cycle with a topological period of $m = 2$ for a coupling parameter of $\varepsilon = 0.07$, whereby coupled systems (1) exhibit phase synchronization. As can be seen, there is a certain time shift between the two curves. Let us consider the given equiphase cycle for various values of the coupling parameter. As ε increases, the time shift Δt between the synchronized orbits decreases; upon the onset of a lag synchronization regime, the time shift, as was noted above, coincides with the time lag between the state vectors of the interacting Rössler oscillators. It is important to note that the dependence of Δt on ε obeys a power law,

$$\Delta t \sim \varepsilon^n, \tag{2}$$

where $n = -1$ in the entire range of variation of the coupling parameter, in which the equiphase resonance saddle 2 : 2 cycle exists. In other words, this relationship is valid in both lag and phase synchronization regimes. An analogous behavior is observed for all equiphase synchronized unstable saddle orbits with other topological periods *m*. It should emphasized that the time shift $\Delta t(\varepsilon)$ is the same for all equiphase saddle cycles, irrespective of their topological periods *m*.

Figure 2 shows a double logarithmic plot of the time shift Δt between synchronized unstable equiphase saddle orbits with the topological periods $m = 1$ (*1*), 2 (*2*), and 3 (*3*) versus the coupling parameter ε. From this plot, it is clearly seen that, first, the time shift Δt between the unstable periodic trajectories in the first and second coupled systems as a function of ε is described by the power law (2) with the exponent $n = -1$, irrespective of the topological period. For simplicity, Fig. 2 presents the data only for three equiphase saddle cycles with the minimum topological periods *m*, but the time shift for the cycles with higher topological periods behaves in the same manner. Second, the time shift Δt for a fixed coupling parameter ε is the same for all synchronized equiphase orbits.

Thus, we have analyzed, in a particular case of two mutually coupled Rössler systems, the time shift between synchronized equiphase unstable saddle orbits incorporated into chaotic attractors of coupled oscillators. It is demonstrated that the dependence of this time

shift on the coupling parameter ε is the same for all cycles, irrespective of their topological periods, and is described by the universal power law $\Delta t \sim \varepsilon^{-n}$ with an exponent of $n = -1$.

It should be noted that the obtained results agree well with the conclusions [13] concerning the phase (or time) shift between synchronized spectral components of the Fourier spectra of mutually coupled chaotic oscillators in the course of lag synchronization. At the same time, the problem of interrelation between the behavior of the Fourier components and the dynamics of saddle orbits incorporated into the given chaotic attractor requires further investigation.

Acknowledgments. This study was supported by the Russian foundation for Basic Research, the Program of Support for Leading Scientific Schools in Russia, the Science and Education Center "Nonlinear Dynamics and Biophysics" at the Saratov State University (sponsored by the US Civilian Research and Development Foundation for the Independent States of the Former Soviet Union, CRDF award No. REC-006), the Noncommercial Program Foundation "Dynasty," and the International Center for Basic Research in Physics (Moscow).

REFERENCES

1. A. Pikovsky, M. Rosenblum, and J. Kurths, *Synchronization: A Universal Concept in Nonlinear Sciences* (Cambridge Univ. Press, Cambridge, 2001).
2. A. S. Dmitriev and A. I. Panas, *Dynamical Chaos: Novel Information Carriers for Communication Systems* (Fizmatlit, Moscow, 2002) [in Russian].
3. R. C. Elson *et al.*, Phys. Rev. Lett. **81**, 5692 (1998).
4. V. S. Anishchenko, V. V. Astakhov, T. E. Vadivasova, *et al.*, *Nonlinear Effects in Random and Stochastic Systems* (Inst. Komp'yut. Issled., Moscow, 2003) [in Russian].
5. A. A. Koronovskiĭ and A. E. Hramov, Pis'ma Zh. Éksp. Teor. Fiz. **79**, 391 (2004) [JETP Lett. **79**, 316 (2004)].
6. A. E. Hramov and A. A. Koronovskiĭ, Chaos **14**, 603 (2004).
7. A. A. Koronovskiĭ and A. E. Hramov, *Continuous Wavelet Analysis and Its Applications* (Fizmatlit, Moscow, 2003) [in Russian].
8. P. Cvitanović, Physica D **51**, 138 (1991).
9. N. F. Rulkov, Chaos **6**, 262 (1996).
10. A. Pikovsky, G. Osipov, M. Rosenblum, *et al.*, Phys. Rev. Lett. **79**, 47 (1997).
11. A. Pikovsky, M. Zaks, M. Rosenblum, *et al.*, Chaos **7**, 680 (1997).
12. D. Pazó, M. Zaks, and J. Kurths, Chaos **13**, 309 (2002).
13. A. A. Koronovskiĭ, O. I. Moskalenko, and A. E. Hramov, Pis'ma Zh. Éksp. Teor. Fiz. **80**, 25 (2004) [JETP Lett. **80**, 20 (2004)].
14. M. G. Rosenblum *et al.*, Phys. Rev. Lett. **89**, 264102 (2002).
15. P. Schmelcher and F. K. Diakonos, Phys. Rev. E **57**, 2739 (1998).
16. D. Pingel, P. Schmelcher, and F. K. Diakonos, Phys. Rev. E **64**, 026214 (2001).

Translated by P. Pozdeev

Technical Physics Letters, Vol. 31, No. 2, 2005, pp. 120–121. Translated from Pis'ma v Zhurnal Tekhnicheskoĭ Fiziki, Vol. 31, No. 3, 2005, pp. 67–71.

Wedgelike Twins Modified by Magnetoplastic Effect in Bismuth Crystals

A. I. Pinchook* and S. D. Shavrei

Mozyr State Pedagogical Institute, Mozyr, Gomel oblast, Belarus

**e-mail: apinchook@tut.by*

Received September 14, 2004

Abstract—The simultaneous action of a concentrated mechanical load and a constant magnetic field leads to a change in the shape of wedgelike twins in bismuth crystals. In the absence of a magnetic field, the wedge angle is close to zero, while application of the field makes this angle close to 180°. This change is explained by a sharp increase in the linear density of twinning dislocations at the twin end. The effect is manifested even after a 2-min exposure of a loaded sample to a magnetic field. © *2005 Pleiades Publishing, Inc.*

Previously, we reported for the first time [1] that the simultaneous action of a constant magnetic field and a concentrated load leads to a decrease in the length of wedgelike twins in single crystal bismuth. In order to elucidate the nature of this magnetoplastic effect in the course of twinning, we have studied the shape of twins formed under prolonged action of an external load and a constant magnetic field.

The experiments were performed with single crystals of bismuth (99.97% Bi) having the shape of rectangular prisms with dimensions $5 \times 5 \times 15$ mm. In order to ensure homogeneity of the applied magnetic field, the samples were mounted at the geometric center of an electromagnet core, in a special holder made of nonmagnetic materials. In this position, the sample was situated at a sufficiently large distance (10 cm) from the stainless steel table of a microhardness meter (PMT-3). Direct measurements using a Hall transducer showed that inhomogeneity of the magnetic field along the sample did not exceed 2%. In order to eliminate instrumental artifacts, all steel elements of the PMT-3 device exposed to the magnetic field (Vickers pyramid holder, loads on the indenter rod, etc.) were replaced by parts made of nonferromagnetic materials.

A concentrated load was applied perpendicularly to a freshly cleaved surface of the sample coinciding with a (111) cleavage plane of the bismuth crystal. Loading in this mode gives rise to lenticular twins of the $\{110\}\langle 001\rangle$ system, which readily grow in depth of the crystal under the action of the applied load and form a wedge upon emerging at the free surface. The magnetic induction was $B = 0.2$ T. The time of the crystal loading under the indenter was varied within 0–5 min. The shapes of wedged twins were studied in an electron microscope. Each experimental point corresponds to the results of measurements for the twins formed around 20 marks of a diamond Vickers indenter. The experimental error did not exceed 3%.

In the absence of an applied magnetic field, wedgelike twins in bismuth crystals have wedge angles close to zero. Figure 1 shows the typical shape of wedgelike twins formed in a magnetic field. Examination of the electron micrographs shows that the wedge angle at the twin end is close to 180°. One possible factor leading to a change in the twin shape is the establishment of a thermodynamically equilibrium length of the wedgelike twin. Evidently, the thermodynamic equilibrium of a twin corresponds to a minimum surface energy of the twin. The minimum surface area of the twin–matrix interface corresponds to a twin shape for which the wedge angle increases and the twin length decreases.

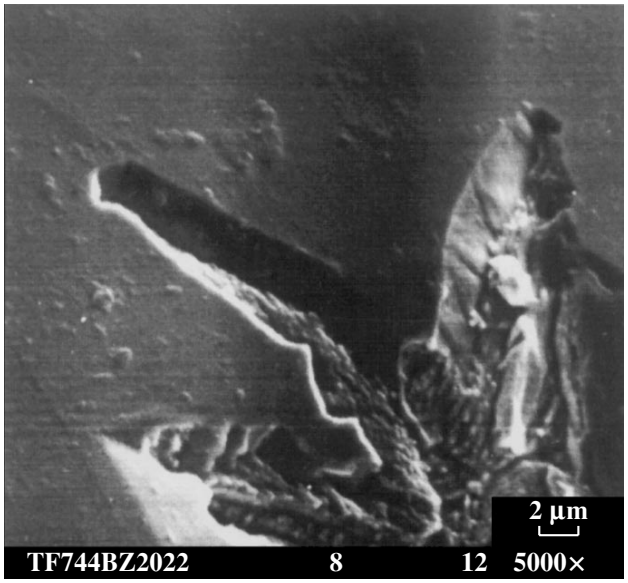

Fig. 1. Electron micrograph showing the typical shape of twins formed in a bismuth crystal loaded in a magnetic field ($B = 0.2$ T; indentation time, 5 min; magnification, ×5000).

1063-7850/05/3102-0120$26.00 © 2005 Pleiades Publishing, Inc.

The thermodynamically equilibrium shape of twins is established as the twinning dislocations bypass stoppers of various types and overcome dry friction forces. According to this mechanism, dislocations have to wait until appropriate thermal fluctuations release them from stoppers. Application of the magnetic field favors the release of a twin contour blocked by a stopper of the paramagnetic type. Under the action of applied load, twinning dislocations occurring in the adjacent twin planes move from the mouth to the end of the twin. At the same time, twinning dislocations at the twin end start moving back under the action of surface tension. Therefore, we may expect that the linear density of twinning dislocations localized at the twin boundary would decrease along the twin, except for a small region at the end where this density is much higher.

Investigation of the twin shape makes it possible to determine variation of the linear density $\rho(x)$ of twinning dislocations as a function of the coordinate x along the twin [2]. This value is defined as [3]

$$\rho(x) = -\frac{1}{a}\frac{dh(x)}{dx},$$

where a is the lattice parameter in the direction perpendicular to the twin plane and $h(x)$ is the twin width. Therefore, by measuring $h(x)$ values on the micrographs, it is possible to determine $\rho(x)$ at each point along the twin. Following the method proposed in [2], we determined $\rho(x)$ by plotting $h(x)$ and graphically differentiating this function. The resulting curve of the linear density of twinning dislocations is presented in Fig. 2.

In the absence of a magnetic field, the linear density of twinning dislocations on a twin boundary is $\rho_0 = 3.5 \times 10^8$ m^{-1}. At the end of a twin with length L (i.e., at $x = L$), this density vanishes ($\rho(L) = 0$). In the applied magnetic field, the linear density of twinning dislocations decreases to $\rho_0 = 2.6 \times 10^8$ m^{-1}. As can be seen from Fig. 2, $\rho(x)$ exhibits a sharp growth in the region of $0.8L \le x \le L$ and is ten times greater than ρ_0 at the twin end.

Without an applied field, the thermodynamically equilibrium twin length is established over several tens of hours [4], while exposure to the field decreases this time to 2 min. Apparently, the magnetic field removes spin prohibition on the interactions between dislocations and point defects, releases twinning dislocations from stoppers of the paramagnetic type, and accelerates the establishment of thermodynamic equilibrium in the system.

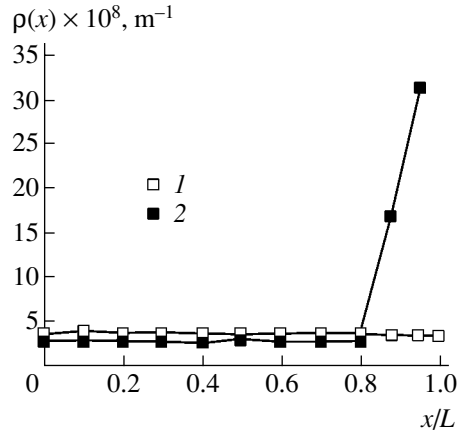

Fig. 2. Variation of the linear density of twinning dislocations $\rho(x)$ along the twin–matrix boundary (*1*) without and (*2*) with an applied magnetic field (B = 0.2 T). Indentation time, 5 min.

Acknowledgments. This study was supported in part by the Foundation for Basic Research of the Belarus Republic, project no. F03-105.

REFERENCES

1. A. I. Pinchuk and S. D. Shavrei, Fiz. Tverd. Tela (St. Petersburg) **43**, 39 (2001) [Phys. Solid State **43**, 39 (2001)].
2. V. P. Soldatov and V. I. Startsev, Dokl. Akad. Nauk SSSR **166**, 588 (1966) [Sov. Phys. Dokl. **11**, 75 (1966)].
3. A. M. Kosevich and L. A. Pastur, Fiz. Tverd. Tela (Leningrad) **3** (1), 1290 (1961) [Sov. Phys. Solid State **3**, 935 (1961)].
4. V. S. Boĭko, R. I. Garber, and L. F. Krivenko, Fiz. Tverd. Tela (Leningrad) **9** (2), 435 (1967) [Sov. Phys. Solid State **9**, 332 (1967)].

Translated by P. Pozdeev

Technical Physics Letters, Vol. 31, No. 2, 2005, pp. 122–124. Translated from Pis'ma v Zhurnal Tekhnicheskoĭ Fiziki, Vol. 31, No. 3, 2005, pp. 72–78.

Plasma Cathode for a Broad-Beam Electron Accelerator

N. V. Gavrilov*, V. V. Osipov, O. A. Bureev, D. R. Emlin, A. S. Kamenetskikh, and V. A. Shitov

Institute of Electrophysics, Ural Division, Russian Academy of Sciences, Yekaterinburg, Russia

**e-mail: gavrilov@iep.uran.ru*

Received July 9, 2004

Abstract—We propose a grid-stabilized plasma cathode based on a slit-contracted low-pressure glow discharge with hollow anode. The area of the plasma cathode is one order of magnitude higher than that in systems where electrons are extracted immediately from plasma in the cathode cavity. Conditions for the discharge initiation, the current switching to the hollow anode, and the obtaining of uniform emission from the plasma cathode are determined. At an accelerating voltage of 160 kV, an electron beam with a 1000×180 mm cross section, a total current of several amperes, and a current pulse duration of up to 10^{-3} s was obtained. The plasma cathode operates under technical vacuum conditions (air, 0.1 Pa) and ensures high stability and reproducibility of the beam current pulses. © *2005 Pleiades Publishing, Inc.*

Creation of a simple and reliable plasma cathode with a large working area, capable of operating in the range of pulse durations from 10^{-5} s to continuous regime and in the range of emission current amplitudes from 0.1 to 10 A and above, opens the way for the development of technological electron-beam-preionization lasers with controlled high peak power and pulse duration. Since the energy efficiency of systems with thermocathodes operating in pulsed regimes is low [1], while the minimum currents of arc plasma emitters [2] are on the order of tens of amperes, it was of interest to study the possibility of utilizing glow discharge, which is capable of operating in both a high-current pulsed regime and a low-current continuous regime.

The lowest working gas pressure necessary to eliminate breakdown of the high-voltage gap is possible in a glow discharge with hollow cathode, at an anode to cathode area ratio $\geq 10^{-2}$ [3]. This condition hinders the creation of a plasma cathode with a large working area (reaching ~100 cm^2 in some known systems of this type [4]). Violation of this relation between the electrode areas limits the working voltage of an electron accelerator on a level determined by the gas breakdown conditions [5]. Use of the anode plasma in a discharge contracted by a small hole leads to considerable inhomogeneity of the plasma, while generation of the anode plasma in a multichannel discharge operation regime is possible only within a limited range of the discharge current [6]. It is also possible to use several cathode chambers with a common hollow anode [7], but the need for providing autonomous electric power and gas supply to each chamber complicates the use and decreases the reliability of such plasma cathode systems.

In this paper, we describe a plasma cathode in which the current of the glow discharge with hollow cathode is flowing to the anode via a long slit. A nearly uniform discharge current distribution along the slit ensures the generation of a homogeneous anode plasma in the slit axis direction, thus making possible the creation of a large-area plasma emitter due to a transverse divergence of the electron flow in the anode discharge region. The transverse inhomogeneity of plasma emission is corrected using a grid with variable transparency.

The proposed electrode system of glow discharge (Fig. 1) comprises hollow cathode *1* with a diameter of

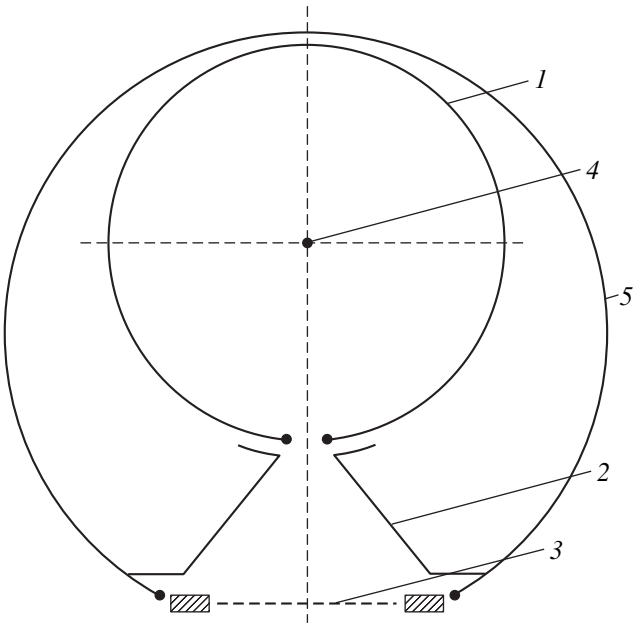

Fig. 1. Schematic diagram of the electrode system of the plasma cathode for an electron accelerator: (*1*) cathode; (*2*) anode; (*3*) grid; (*4*) tungsten filament; (*5*) case.

200 mm and a length of 1000 mm and hollow anode *2*. A part of the anode surface (180 × 1000 mm) is covered by metal grid *3*, which can be insulated from the anode. The discharge is initiated by tungsten wire *4* extended along the cathode axis, which is connected via resistor *R* to a positive output of the discharge power supply source. The cathode has a 1000-mm-long slit with a width varied within h = 10–40 mm. The electrode system of the glow discharge is arranged inside case *5* occurring at the anode potential. The working gas leaks to a cathode cavity. The length of high-voltage gaps in the vacuum chamber is 80–100 mm. The system is evacuated by an oil diffusion pump without a liquid nitrogen trap.

The steady-state discharge is established upon initiation of the glow discharge between the filament and cathode, followed by the discharge development toward the anode. The discharge initiation voltage was 2.6–1.5 kV at a working air pressure of $(4–6) \times 10^{-2}$ Pa. As the overvoltage on the gap (1–2.5 kV) and the gas pressure increase, the discharge delay time decreases from 200 to 50 μs. The time of the discharge current switching to the anode depends on the resistance *R*: as the *R* value is decreased from 1 to 0.1 kΩ, the filament current increases and the switching time decreases to 20–30 μs (Fig. 2). Fast switching at low gas pressures takes place for $R = 0$, but the filament current I_1 in this case increases to 1/3 of the discharge current. The influence of *R* on the time of current switching to the anode is determined by the ion space charge sheath dynamics in the cathode cavity. An increase in the filament current I_1 and the corresponding decrease in the plasma potential (by RI_1) lead to a decrease in the cathode sheath thickness and a potential barrier height in the cathode aperture. This leads to an increase in the current of fast electrons (penetrating into the anode cavity) and in the reverse ion current, which eventually results in breakage of the cathode sheath and in the current switching to the anode [8]. The greater the initial current in the filament circuit and the higher the gas pressure, the faster the discharge switching to the anode. In the steady-state regime, the potential difference between the cathode and anode plasmas is 10–40 V.

The stable operation of discharge with a nearly uniform current distribution along the slit is achieved for slit dimensions such that its area is one order of magnitude greater than that corresponding to the optimum ratio of the anode and cathode surfaces, $S_c/S_a \sim (M_i/m_e)^{1/2}$, where M_i and m_e are the ion and electron masses, respectively [3]. A decrease in the slit width leads to contraction of the discharge; an increase in the slit width leads to a growth in the minimum working gas pressure and the discharge voltage. Stable operation of the glow discharge at a large slit width is also provided by the screening effect of the cathode sheath, whose thickness in the discharge with electron oscillations may exceed that estimated using the Child–Langmuir law.

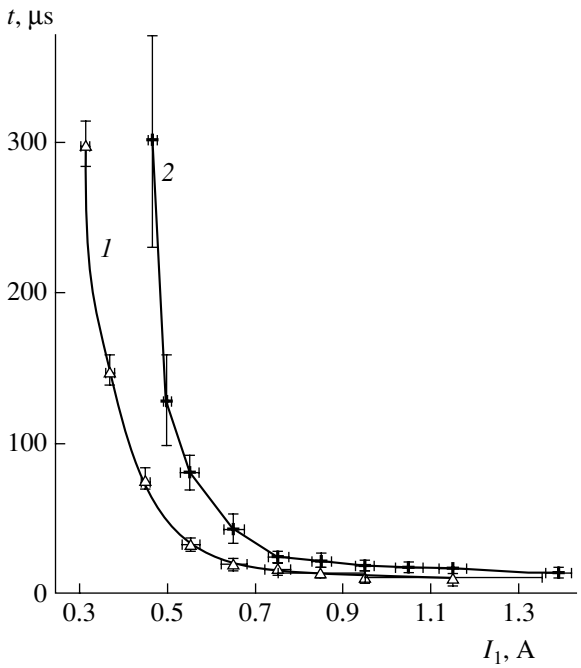

Fig. 2. Plots of the time of discharge current switching to the anode versus filament current in argon at a pressure of (*1*) 5×10^{-2} and (*2*) 2.2×10^{-2} Pa.

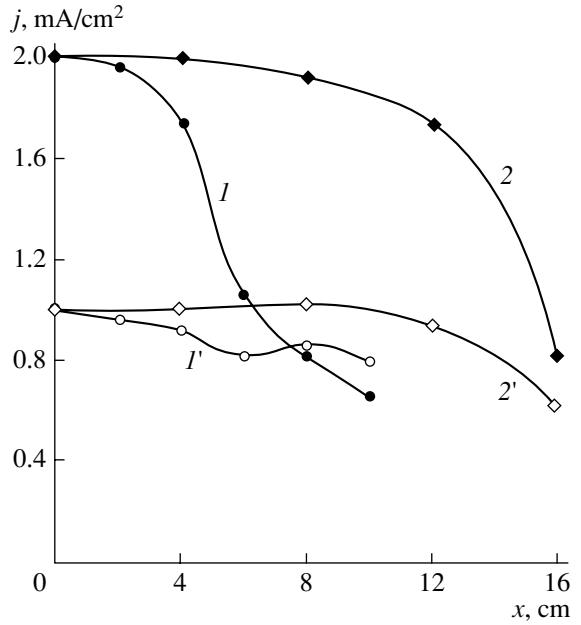

Fig. 3. Transverse (*1*, *1*') and longitudinal (*2*, *2*') electron beam current density profiles: (*1*, *2*) with 0.6 × 0.6 mm mesh grid, beam current 0.65 A; (*1*', *2*') with an additional correcting grid, beam current 0.43 A. Cathode aperture, 40 mm; discharge current 1 A; accelerating voltage 1 kV; accelerating gap width, 4 cm; argon pressure, 0.05 Pa.

Figure 3 shows the electron beam current density profiles obtained in a prototype with a 350 × 200 mm grid. The inhomogeneity of these distributions in the direction parallel to the slit was ~10% of the maximum

current over a distance equal to 0.6 of the cathode length. The full width at half maximum (FWHM) of the transverse profile was 100–120 mm at a slit width of 40–20 mm and a grid–slit spacing of 100 mm. A decrease in this spacing and in the slit width makes the transverse profile more inhomogeneous. Using the grid with variable transparency for the correction of the transverse profile of the emission current density, it is possible to significantly decrease the inhomogeneity of emission (Fig. 3, curves *1*' and *2*').

The proposed system, as well as the arc plasma cathodes with a positive anode potential drop, make possible the grid control of the plasma cathode emission [9]. By applying a pulsed voltage between the grid and the anode, we obtained electron emission current pulses with a current buildup time determined by the front width of the control pulse (several microseconds).

High-voltage tests were performed at a constant accelerating voltage of 160 kV in a periodic-pulsed regime of the electron beam generation at a frequency of 1–10 Hz. The working gas was air at a pressure of 0.06 Pa in the accelerator chamber. For a current pulse duration of 0.4–1 ms, we obtained an electron beam with a total current of several amperes. The current amplitude variation from one pulse to another did not exceed 10%, while the pulse duration instability related to a statistical scatter of the discharge initiation time amounted to several tens of microseconds. The large leading and trailing front durations (>100 μs) can be decreased to several tens of microseconds by optimizing the pulsed transformer and to several microseconds by using the grid control. The electron extraction efficiency, defined as the ratio of the beam current to the glow discharge current, was 0.5 for a grid mesh of 0.2×0.2 mm and an accelerating gap width of 80 mm.

The proposed plasma cathode offers the following advantages: (i) simplicity and reliability of operation; (ii) long working life and stable operation under technical vacuum conditions; (iii) high stability and reproducibility of the pulse shape; (iv) broad range of controlled variation of the pulse duration and beam current amplitude.

REFERENCES

1. S. P. Bugaev, Yu. E. Kreĭndel', and P. M. Shchanin, *Broad Electron Beams* (Énergoatomizdat, Moscow, 1984) [in Russian].
2. N. V. Gavrilov, B. M. Koval'chuk, Yu. E. Kreĭndel', *et al.*, Prib. Tekh. Éksp., No. 3, 152 (1981).
3. A. S. Metel', Zh. Tekh. Fiz. **54**, 241 (1984) [Sov. Phys. Tech. Phys. **29**, 141 (1984)].
4. Yu. A. Mel'nik, A. S. Metel', and G. D. Ushakov, in *Proceedings of the 7th All-Union Symposium on High-Current Electronics, Tomsk, 1988*, Chap. 1, pp. 113–115.
5. Y. R. Bayless, Rev. Sci. Instrum. **46**, 1158 (1975).
6. B. I. Zhuravlev, V. V. Prilepskiĭ, and V. S. Gorlatov, Prib. Tekh. Éksp., No. 3, 215 (1993).
7. V. V. Boĭko, A. I. Kuz'michev, V. N. Sukhanov, *et al.*, in *Proceedings of the 1st All-Union Conference on Plasma Emission Electronics, Ulan-Ude, 1991*, pp. 106–109.
8. *Electron Sources with Plasma Emitter*, Ed. by Yu. E. Kreĭndel' (Nauka, Novosibirsk, 1983), pp. 5–14 [in Russian].
9. V. I. Gushenets, N. N. Koval', Yu. E. Kreĭndel', *et al.*, Zh. Tekh. Fiz. **57**, 2264 (1987) [Sov. Phys. Tech. Phys. **32**, 1371 (1987)].

Translated by P. Pozdeev

Technical Physics Letters, Vol. 31, No. 2, 2005, pp. 125–127. Translated from Pis'ma v Zhurnal Tekhnicheskoĭ Fiziki, Vol. 31, No. 3, 2005, pp. 79–85.

Electron Tunneling in ZnS:Mn Thin-Film Emitters

N. T. Gurin*, D. V. Ryabov, O. Yu. Sabitov, and A. M. Afanas'ev

Ul'yanovsk State University, Ul'yanovsk, Russia

**e-mail: gurinnt@sv.ulsu.ru*

Received August 4, 2004

Abstract—Experimental kinetics of the current and charge transferred via a phosphor layer in ZnS:Mn electroluminescent thin-film emitters have been numerically simulated using a model time dependence of the current of electrons tunneling from the surface states at the insulator–semiconductor interface. It is found that, as the field strength increases, the depth of the surface states changes from ~0.6 to 1.3 eV, the electron tunneling probability increases from 10–15 to 300–400 s^{-1}, and the potential barrier width decreases from 9 to 5.7 nm. © *2005 Pleiades Publishing, Inc.*

Introduction. The optical emission in electroluminescent thin-film (ELTF) devices based on a ZnS:Mn structure of the metal–insulator–semiconductor–insulator–metal (MISIM) type is determined by the tunneling of charge carriers from the surface states in the near-cathode region of the insulator–semiconductor interface in a strong electric field. This is followed by the avalanche multiplication of charge carriers due to impact ionization of the intrinsic structural defects and impurities, with simultaneous impact excitation of Mn^{2+} emitting centers [1]. An exact theoretical description of the process of electron tunneling from the surface states and the parameters of the potential barrier at the insulator–semiconductor interface has not been developed so far. There were attempts to model these processes [2, 3] with neglect of the electron multiplication in the phosphor layer and with the assumption that the surface states correspond to a discrete level with an energy of E_t = 0.8 eV below the conduction band bottom of ZnS:Mn. The results of these simulations qualitatively agree with the published experimental data. The dependence of the tunneling emission rate on the field strength was also modeled in [4], where it was shown that the surface states can be localized on the energy levels 0.6–0.9 eV below the conduction band bottom. Based on qualitative agreement between the results of modeling and the experimental current and voltage kinetics in ELTF emitters excited by a sinusoidal voltage, the energy of the surface states was also evaluated at E_t = 1.05 eV with a possible scatter from 0.9 to 1.2 eV [5]. In [6], the hysteresis in the voltage–luminance characteristics of ELTF emitters was simulated assuming a uniform distribution of the density of surface states in the interval E_t = 0–2 eV and their uniform filling up to the Fermi energy in the equilibrium state.

The aim of this study was to determine the characteristics of the electron tunneling and the parameters of surface states in the near-cathode region of the insulator–semiconductor interface.

In order to determine these characteristics and parameters, we will use the kinetics $I_p(t)$ of the current passing via the phosphor layer. It was demonstrated [7, 8] that the initial region of rapid increase in $I_p(t)$ upon ELTF emitter excitation by a linearly increasing voltage is described by an exponent. In the same region, the time variation of the average field in the phosphor, $F_p(t)$, is almost linear (see region I in Fig. 1), which is evidence for the absence of a significant space charge in the phosphor and a homogeneous field distribution in this layer. Taking into account that the voltage drop across the phosphor layer (~45–120 V) significantly exceeds the E_g/q value (E_g = 3.7 eV is the bandgap width of ZnS:Mn and q is the electron charge), we conclude that the same field $F_p(t)$ acts in the region of a potential barrier in the near-cathode region of the insulator–semiconductor interface.

For a homogeneous field in the phosphor layer, the coefficient α_n of electron impact ionization in this layer can be expressed as

$$\alpha_n = \frac{1}{n_p}\frac{\partial n_p}{\partial x} = \frac{1}{n_p}\frac{\Delta n_p}{\Delta x} = \frac{1}{n_p}\frac{n_p - n_{p0}}{d_p} = \frac{1}{d_p}\left(1 - \frac{1}{M}\right), \quad (1)$$

where n_{p0} and n_p are the densities of electrons entering into the region of impact ionization and leaving this region, respectively; d_p is the phosphor layer thickness; and $M = n_p/n_{p0}$ = const is the electron multiplication coefficient.

Under these conditions, the current of electrons entering into the region of impact ionization (that is, the tunneling current of electrons from the surface states in

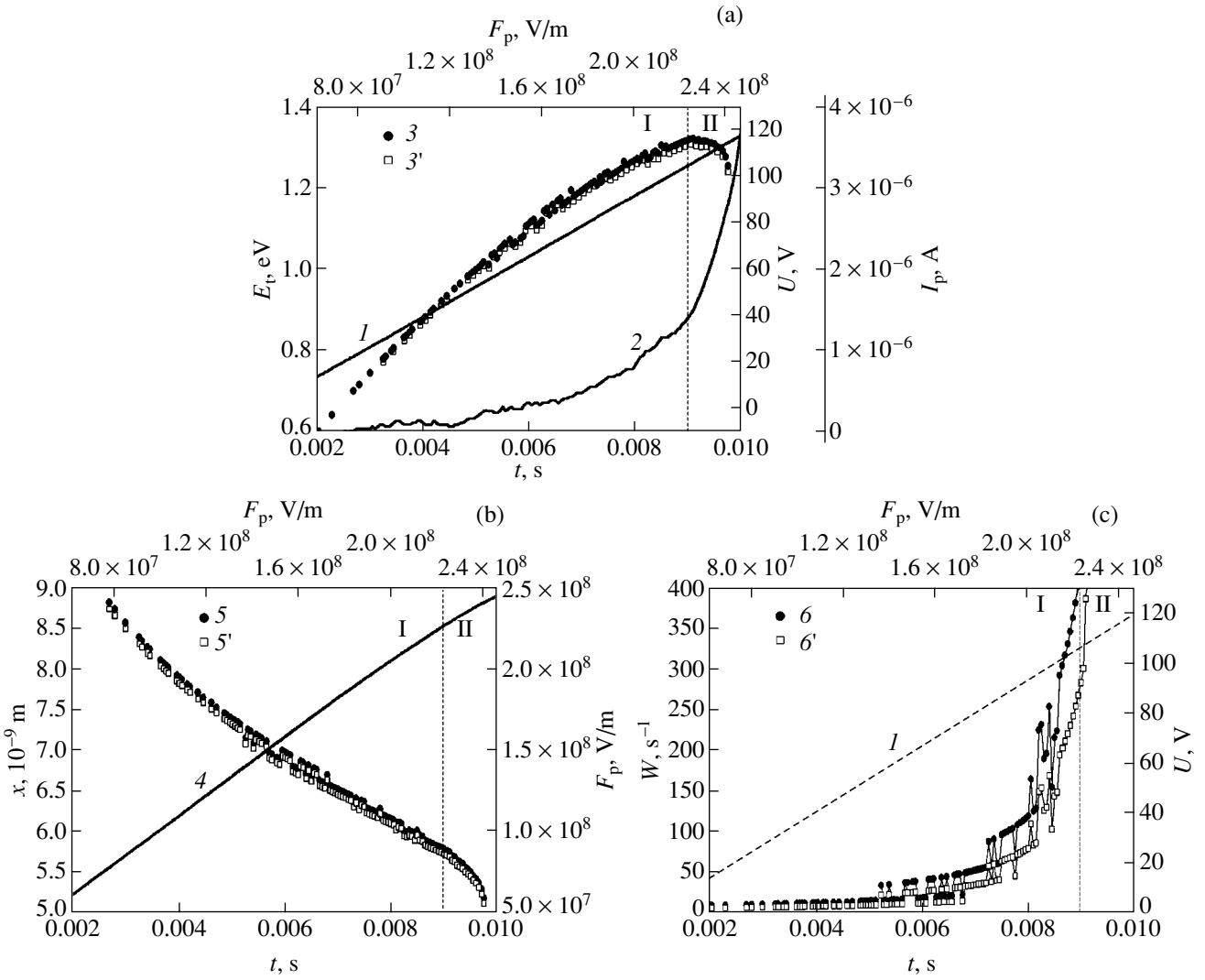

Fig. 1. Time variation of the functions: (*1*) $U(t)$; (*2*) $I_p(t)$; (*3*, *3*') $E_t(t)$; (*4*) $F_p(t)$; (*5*, *5*') $x_t(t)$ (in –Al regime); (*6*, *6*') $W(t)$ in +Al and –Al regimes, respectively. Regions I and II correspond to a linear and sublinear variation of $F_p(t)$, respectively; $M = 1.5$ (*3*, *5*); 1 (*3*', *5*').

the near-cathode region of the insulator–semiconductor interface) is given by the formula

$$I_{p0}(t) = \frac{I_p(t)}{M} = \frac{q}{M}\frac{\partial n_p(t)}{\partial t}. \qquad (2)$$

At the same time, an expression for $I_{p0}(t)$ can be obtained from a kinetic equation describing the tunneling of electrons from the surface states via the potential barrier:

$$I_{p0}(t) = W(t)\left[Q_{ss} - \frac{Q_p(t)}{M}\right], \qquad (3)$$

where $W(t)$ is the probability of tunneling per unit time (i.e., the electron generation rate), which can be determined using a formula successfully used for ZnS-based emitters [5, 9]:

$$W(t) = \frac{qF_p(t)}{2\sqrt{2m^*E_t(t)}}\exp\left[\frac{4\sqrt{2m^*}E_t^{3/2}(t)}{3q\hbar F_p(t)}\right]; \qquad (4)$$

$Q_p(t) = \int_0^t I_p(t)dt$ is the charge passing through the phosphor layer; Q_{ss} is the charge accumulated on the surface states; $m^* = 0.34m_e$ [9] is the effective electron mass for ZnS; m_e is the electron rest mass; and $\hbar$ is the Planck constant.

Owing to a homogeneous distribution of the field $F_p(t)$ in the phosphor layer, we can ignore the formation of a space charge in region I by means of the impact ionization of deep centers (related to the intrinsic defects [11]). Therefore, no additional charge carriers are generated in this layer and, hence, $M \simeq 1$.

Equations (2)–(4) were used for numerical modeling of the experimental kinetics $I_p(t)$. The obtained

functions $Q_p(t)$ and $F_p(t)$ were used to determine the characteristics of electron tunneling, $E_p(t)$ and $W(t)$, and the potential barrier width $x_t(t)$, defined as

$$x_t(t) = \frac{E_t(t)}{qF_p(t)}. \quad (5)$$

The experimental curves were measured using ELTF emitters described in [10, 11]. The samples had a MISIM layer structure, where M layers represent a lower transparent 0.2-μm-thick SnO_2-based electrode deposited onto a glass substrate and the upper nontransparent thin-film Al electrode with a thickness of 0.15 μm and a diameter of 1.5 mm; S is the 0.48-μm-thick electroluminescent ZnS:Mn (0.5 wt %) layer; and I are the 0.17-μm-thick insulating ZrO_2–Y_2O_3 (13 wt %) layers. The ZnS:Mn phosphor layer was obtained by thermal evaporation in a quasi-closed volume in vacuum and deposition onto a substrate heated to 250°C, followed by annealing for 1 h at 250°C. The upper nontransparent metal electrode was also formed by thermal deposition in vacuum, while thin insulating layers were prepared using the electron-beam deposition technique.

The ELTF emitters were excited with alternating-sign voltage pulses of a triangular shape. The excitation signal $U(t)$ represented pairs of triangular pulses with a frequency of 20 Hz. In the first half-period, either a positive or negative excitation half-wave could be applied to the upper electrode, which is referred to as the +Al or –Al regime, respectively. The time interval T_s between excitation pulse trains was T_s = 100 s. The emitter current $I_e(t)$ was measured as described in [7, 8, 10, 12].

The time variation of the average field $F_p(t)$ in the phosphor layer, the current $I_p(t)$, and the charge $Q_p(t)$ passing through this layer during ELTF emitter operation were determined for the first half-period of $U(t)$ as described elsewhere [7, 12], using preset values of capacitances of the insulating films (730 pF) and the phosphor layer (275 pF) determined using an immittance meter of the E7-14 type and the known ELTF emitter geometry. The $I_p(t)$ curves were numerically simulated using the values of $Q_{ss} = (1.7–1.9) \times 10^{-8}Q$ determined previously [11] and two values of the multiplication coefficients, namely, M = 1 and 1.5 (the latter value was obtained [11] for the excitation signal amplitude U = 160 V).

The results of numerical calculations are presented in Fig. 1. In the initial region I, where the current $I_p(t)$ exhibits exponential growth and the function $F_p(t)$ is almost linear (up to ~9 ms), the increase of t or $F_p(t)$ is accompanied by a monotonic increase in the depth of surface states, whereby $E_t(t)$ changes from ~0.6 to ~1.3 eV (see Fig. 1a; an analogous behavior is observed for $E_t(t)$ in the +Al regime). Simultaneously, the potential barrier width $x_t(t)$ in the near-cathode region of the insulator–semiconductor interface decreases from ~9 to ~5.7 nm in both the +Al and –Al regimes (see Fig. 1b), while the tunneling probability $W(t)$ increases from 10 to 300 s^{-1} (in the –Al regime) and from 15 to 400 s^{-1} (in the +Al regime) (see Fig. 1c). These results, on the one hand, agree with the aforementioned data [2–6] and, on the other hand, show evidence for a more complicated character of the energy distribution of surface states as compared to that according to the discrete level model and the model of uniform energy distribution. Note also that our results are indicative of a weak influence of the multiplication coefficient M (varied between 1 and 1.5) on the $E_t(t)$ and $x_t(t)$ functions.

Finally, it should be noted that the validity of formula (4) determining the probability $W(t)$ may suggest that electrons in the surface states are bound to neutral centers [9]. Our data indicate also that all levels in the bandgap of ZnS:Mn, which correspond to the intrinsic defects with energies ≤1.3 eV below the conduction band bottom (e.g., Zn_i^0 (0.10–0.12 eV); Zn_i^+ (0.2 eV); Vs^0 (0.2–1.05 eV) [8]), can be depleted in the region of exponential growth of the current $I_p(t)$ (region I) as a result of electron tunneling from these states to the conduction band of ZnS:Mn.

Acknowledgments. This study was supported by the Presidential Program of Support to the Leading Scientific Schools of Russia, project no. NSh-1428.2003.8.

REFERENCES

1. *Electroluminescent Sources of Light*, Ed. by I. K. Vereshchagin (Énergoatomizdat, Moscow, 1990) [in Russian].
2. E. Bringuier, J. Appl. Phys. **66**, 1314 (1989).
3. K. A. Neyts and P. De Visschere, J. Appl. Phys. **68**, 4163 (1990).
4. D. H. Smith, J. Lumin. **23**, 209 (1981).
5. V. P. Vasil'chenko, Zh. Prikl. Spektrosk. **63**, 461 (1996).
6. W. E. Howard, O. Sahni, and M. Alt, J. Appl. Phys. **53**, 639 (1982).
7. N. T. Gurin, A. V. Shlyapin, and O. Yu. Sabitov, Zh. Tekh. Fiz. **72** (2), 74 (2002) [Tech. Phys. **47**, 215 (2002)].
8. N. T. Gurin, A. V. Shlyapin, and O. Yu. Sabitov, Zh. Tekh. Fiz. **73** (4), 100 (2003) [Tech. Phys. **48**, 479 (2003)].
9. A. N. Georgobiani and P. A. Pipinis, *Tunneling Phenomena in Luminescence of Semiconductors* (Mir, Moscow, 1994) [in Russian].
10. N. T. Gurin and D. V. Ryabov, Pis'ma Zh. Tekh. Fiz. **30** (9), 89 (2004) [Tech. Phys. Lett. **30**, 392 (2004)].
11. N. T. Gurin and D. V. Ryabov, Zh. Tekh. Fiz. **75** (1), 45 (2005) [Tech. Phys. **50**, 44 (2005)].
12. N. T. Gurin, O. Yu. Sabitov, and A. V. Shlyapin, Zh. Tekh. Fiz. **71** (8), 48 (2001) [Tech. Phys. **46**, 977 (2001)].

Translated by P. Pozdeev

Technical Physics Letters, Vol. 31, No. 2, 2005, pp. 128–131. Translated from Pis'ma v Zhurnal Tekhnicheskoĭ Fiziki, Vol. 31, No. 3, 2005, pp. 86–94.

Effect of Implanted Phosphorus Ions on the Crystallization of Amorphous Silicon Films under the Action of Pulsed Excimer Laser Radiation

M. D. Efremov, V. A. Volodin*, S. A. Arzhannikova, S. A. Kochubeĭ, and V. N. Ulasyuk

Institute of Semiconductor Physics, Siberian Division, Russian Academy of Sciences, Novosibirsk, Russia
ELTAN Company, Fryazino, Moscow oblast, Russia
**e-mail: volodin@isp.nsc.ru*

Received August 10, 2004

Abstract—We have studied the effect of implanted phosphorus ions on the crystallization of thin amorphous silicon films under the action of nanosecond radiation pulses of a XeCl excimer laser. The amorphous silicon films with a thickness of 90 nm, obtained by plasmachemical deposition on glass substrates, were implanted with phosphorus ions at a dose of 3×10^{14} and 3×10^{15} cm^{-2}. The subsequent laser treatments were performed using energies both above and below a threshold corresponding to the fusion of amorphous silicon. The structure of the silicon films was studied using Raman scattering spectroscopy. An analysis of the experimental data shows that implanted phosphorus stimulates nucleation, especially in the case of liquid phase crystallization. The results are of interest for the development of the technology of thin-film transistors on nonrefractory substrates. © *2005 Pleiades Publishing, Inc.*

In recent years, large-scale microelectronics has been among the most rapidly developing fields of modern electronics. This is related primarily to the growing production of flat displays and indicators for data visualization. The most promising control elements for both liquid crystal and laser diode displays of the new generation are provided by active matrices of thin-film transistors based on amorphous or polycrystalline silicon. In this context, the problem of shallow impurity activation in thin films of amorphous and polycrystalline silicon with a view to the doping of the source and sink contact regions is still of considerable importance. Traditionally, shallow impurities are activated by means of heat treatment (furnace anneals) under rather high thermal load conditions involving temperatures above 900°C and durations above one hour. Such treatments are inapplicable in the case of cheap nonrefractory glass substrates. In this case, it is possible to apply pulsed treatments using excimer laser radiation [1]. This approach is also advantageous for the creation of ultrashallow *p*–*n* junctions (see, e.g., [2] and references therein). For the creation of thin-film transistors, dopants can be introduced in concentrations on the order of 10^{19} cm^{-3}. As is known, both donor and acceptor impurities in such concentrations influence the kinetics of crystallization exhibited by amorphous silicon in the course of heat treatments [3–5].

The aim of this study was to determine the influence of phosphorus on the crystallization of thin amorphous silicon films under the action of nanosecond radiation pulses of a XeCl excimer laser.

The effects of shallow impurities on the nucleation and crystallization kinetics and the process of impurity activation under the action of pulsed laser radiation were studied on a series of specially prepared structures based on nonrefractory glass substrates. The rear electric contact was formed by vacuum deposition of a thin aluminum film onto glass. Then, an amorphous silicon film with a thickness of 90 nm was obtained by means of plasmachemical deposition. The thickness and optical parameters of this film were determined by ellipsometry using a He–Ne laser (λ = 633 nm). These samples were implanted with phosphorus ions at a dose of 3×10^{14} and 3×10^{15} cm^{-2} at an ion beam energy of 30 keV. The average range of phosphorus ions in the target (calculated using the standard TRIM routine) was about 500 Å, so that the maximum of the implanted ion concentration profile occurred approximately in the middle of the silicon layer. During implantation, 1/3 of the sample surface area was screened and remained undoped (for comparison).

The structures of the sample films were studied by Raman spectroscopy. The measurements were performed at room temperature in the quasi-backscattering geometry. The polarization characteristics of the scattered light were not studied. The Raman spectra were excited using radiation of an Ar laser operating at λ = 514.5 nm.

Both implanted and unimplanted regions of the samples were subjected to pulsed laser treatments performed using a XeCl excimer laser operating at a wavelength of 308 nm. The laser pulse duration (full width

1063-7850/05/3102-0128$26.00

at half maximum) was below 25 ns. The samples were treated in three regimes differing by the energy density per pulse (ρ). In regime *A*, the laser energy density was sufficiently high to melt the material virtually through the entire silicon film thickness (single pulse); in regime *B*, ρ was also above the melting threshold of amorphous silicon, but insufficient to melt it through the entire film thickness (single pulse); in regime *C*, ρ was below the melting threshold of amorphous silicon (ten pulses). According to published data, a threshold energy density sufficient for the onset of nonlocal melting of amorphous silicon is 120–150 mJ/cm^2 [6]. Using the laser processing regime employed in this study, it is possible to perform crystallization of thin amorphous silicon films on nonrefractory (even plastic) substrates [7, 8].

Figure 1 shows the typical Raman spectra of the initial amorphous silicon film (curve *1*) and the films studied immediately after implantation with phosphorus ions at a dose of 3×10^{14} cm^{-2} (curve *2*) and 3×10^{15} cm^{-2} (curve *3*). Owing to the absence of the translational symmetry in amorphous silicon, the optical transitions in this material are not restricted by the law of quasi-momentum conservation. For this reason, the Raman spectrum of amorphous silicon in the optical domain is characterized by the effective density of vibrational states and appears as a broad band with a maximum at 480 cm^{-1} [9]. The intrinsic vibrational modes of silicon nanograins are spatially localized, and the position of their Raman band maximum depends on the nanograin size. As the nanograin size increases above 50 nm, the position of this maximum is virtually the same as that in the spectrum of crystalline silicon (~520 cm^{-1}) [10]. The width of the Raman band is determined by the dispersion of nanograin dimensions and by the uncertainty relationship between the energy and wavenumber, which is related to a finite lifetime of phonons and their spatial localization. The intensity of the "crystalline" component is proportional to the fraction of the nanocrystalline phase.

As can be seen from Fig. 1, the initial film contains no nanocrystalline inclusions. Ion implantation leads to a certain decrease in the Raman signal intensity, while the greater ion dose also produces some shift and broadening of the band. As is known, the width of the "amorphous" band depends on the mean deviation of the Si–Si bond length from that in the ideal tetrahedral configuration [11]. Therefore, the observed broadening can be related to an even greater extent of the disorder resulting from the ion bombardment. According to the results of ellipsometric measurements, the refractive index of the initial film is 3.15, which coincides with the value for hydrogenated amorphous silicon containing about 10–20% of atomic hydrogen. The implantation with phosphorus ions at a dose of 3×10^{15} cm^{-2} led to a certain decrease in the refractive index (to 3.05) and an increase in the absorption coefficient.

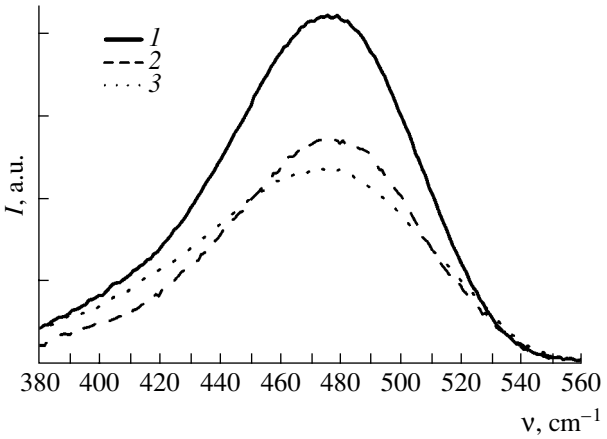

Fig. 1. Raman spectra of amorphous silicon films (*1*) ion the initial state and (*2*, *3*) implanted with 30-keV phosphorus ions at a dose of 3×10^{14} and 3×10^{15} cm^{-2}, respectively.

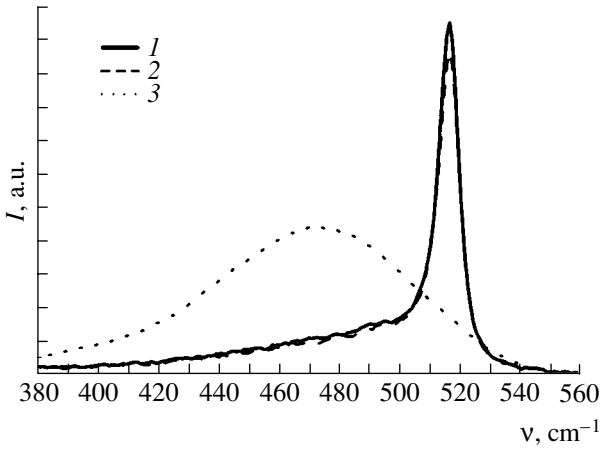

Fig. 2. Raman spectra of (*1*) initial silicon film and (*2*, *3*) films implanted with 30-keV phosphorus ions at a dose of 3×10^{14} and 3×10^{15} cm^{-2}, respectively, measured after pulsed laser treatment in regime *A* (complete melting).

Figures 2 and 3 show the Raman spectra of unimplanted silicon films and the films implanted with different doses of phosphorus ions measured after pulsed laser treatments in the regimes with an energy density above the melting threshold. The main conclusions derived from the Raman spectroscopy data for these laser-treated samples are as follows. In regime *A* (almost complete melting) (Fig. 2), the implantation of phosphorus to an average concentration of 3.3×10^{19} cm^{-3} (corresponding to a dose of 3×10^{14} cm^{-2}) virtually did not influence the crystallization of amorphous silicon films. In contrast, the films implanted at a dose of 3×10^{15} cm^{-2} remained practically amorphous. At the same time, the results of ellipsometric measurements showed that the refractive index of these films increased to 3.15 and the absorption coefficient exhibited an almost twofold growth as compared to that in the initial samples. According to published data, phos-

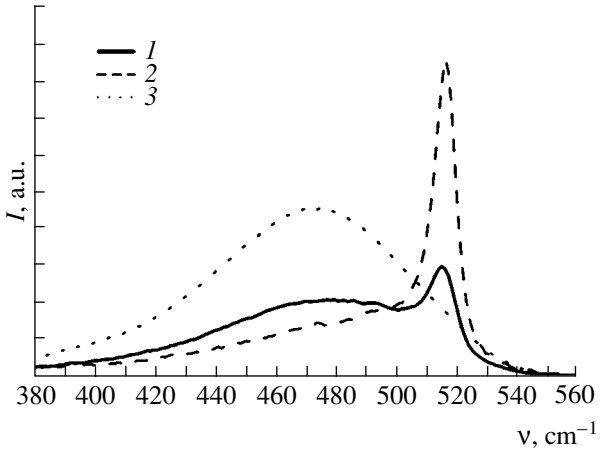

Fig. 3. Raman spectra of (*1*) initial silicon film and (*2, 3*) films implanted with 30-keV phosphorus ions at a dose of 3×10^{14} and 3×10^{15} cm^{-2}, respectively, measured after pulsed laser treatment in regime *B* (partial melting).

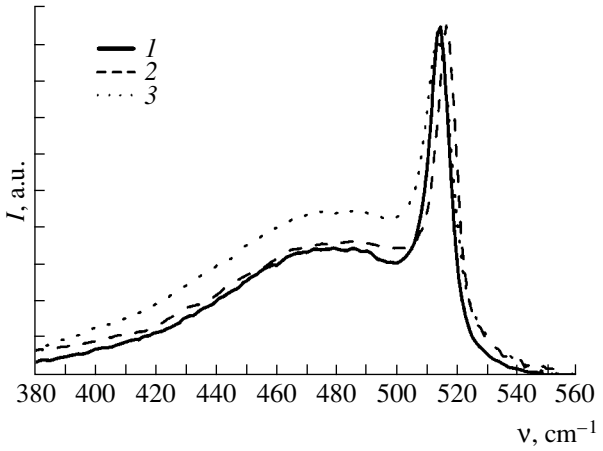

Fig. 4. Raman spectra of (*1*) initial silicon film and (*2, 3*) films implanted with 30-keV phosphorus ions at a dose of 3×10^{14} and 3×10^{15} cm^{-2}, respectively, measured after pulsed laser treatment in regime *C* (below melting threshold).

phorus accelerates crystallization during both furnace and laser anneals, provided that the annealing temperature is below the melting point of silicon [3–5, 12]. Apparently, the role of phosphorus in the process of laser annealing involving the formation of a melted phase is as follows. The average concentration of phosphorus atoms in the film implanted at a higher dose is 3.3×10^{20} cm^{-3}. Assuming that, beginning with a certain critical concentration, each phosphorus atom serves as a center of nucleation of the crystalline phase in the melt, the distance between such nuclei at this implanted dose is about 14 Å. Accordingly, the average grain size should be on the same order of magnitude. However, this value is comparable with (or even smaller than) the correlation length (a parameter of order) in the amorphous silicon (10–15 Å [13]). Therefore, the film will exhibit amorphization (as a result of a very large probability of nucleation) upon supercooling. This process is analogous to the amorphization of silicon taking place as a result of strong heat dissipation in strongly supercooled solutions [14]. Similar behavior is observed in Fig. 3 for the laser treatment in regime *B* (where the laser energy density was also above the melting threshold of amorphous silicon but was insufficient to melt it through the entire film thickness). The only difference from the previous case was that the presence of phosphorus implanted at a dose of 3×10^{14} cm^{-2} led to an increase in the crystallization rate.

It is interesting to compare these results to the behavior of amorphous silicon films implanted with phosphorus ions to the same doses and then laser-treated in regime *C*, whereby the laser energy density is below the film melting threshold. The Raman spectroscopy data for these samples are presented in Fig. 4. Using the ratio of integral intensities of the "amorphous" and "crystalline" signal components, it is possible to estimate the volume fraction of the crystalline phase in the films studied [7, 11]. This fraction is about 20% in the unimplanted silicon film and about 25% in the film implanted with phosphorus. Thus, in agreement with published data, phosphorus accelerates crystallization in the solid-phase regime. It should be also noted that the position of the "crystalline" peak in the unimplanted film (516 cm^{-1}) differs from that in the implanted sample (513.5 cm^{-1}). Moreover, the latter peak is also additionally broadened, which indicates that the grain size in the film implanted with phosphorus is smaller than in the unimplanted sample. This can be related to an increase in the probability of nucleation in the presence of phosphorus: the higher the density of nuclei, the lower the grain size. The laser treatments in all regimes led to an increase in the conductivity of phosphorus-implanted films by several orders of magnitude. This suggests that these treatments converted shallow impurity (phosphorus) into an electrically active state.

It should be emphasized that this activation of the impurity was performed in the films deposited onto nonrefractory substrates (with a glass softening temperature below 350°C). Using this approach, it is also possible to activate shallow impurities in silicon films deposited onto substrates having even lower softening temperatures. Another advantage of this approach is the short duration of treatments. During a treatment time on the order of tens of nanoseconds, the impurity cannot travel over long distances, which is especially important for the creation of shallow *p–n* junctions.

Thus, we have demonstrated that implanted phosphorus significantly increases the probability of nucleation in the case of a phase transition involving the formation of a liquid (melt) phase of silicon (high laser energy densities). In the case of laser treatments with an energy density below a threshold corresponding to the

fusion of amorphous silicon, the influence of implanted phosphorus consists in increasing the rate of crystallization. In both cases, exposure to excimer laser radiation leads to activation of the implanted impurity.

Acknowledgments. the authors are grateful to O.I. Semenova for the preparation of amorphous films and to V.G. Seryapin for carrying out ion implantation.

REFERENCES

1. M. D. Efremov, V. A. Volodin, L. I. Fedina, *et al.*, *Abstracts of European Materials Research Society, Spring Meeting, Strasbourg, 2000*, p. O/P24.
2. P. J. Timans, W. Lerch, S. Paul, *et al.*, Solid State Technol. **47** (5), 35 (2004).
3. A. V. Dvurechenskiĭ, V. P. Popov, B. P. Kashnikov, *et al.*, Poverkhnost **9**, 77 (1986).
4. R. Grotzschel, A. V. Dvurechenskiĭ, and V. P. Popov, Fiz. Tverd. Tela (Leningrad) **28**, 3134 (1986) [Sov. Phys. Solid State **28**, 1763 (1986)].
5. L. Csepregi, E. F. Kennedy, T. J. Gallagher, *et al.*, J. Appl. Phys. **48**, 4234 (1977).
6. T. Sameshima and S. Usui, J. Appl. Phys. **70**, 1281 (1991).
7. M. D. Efremov, V. V. Bolotov, V. A. Volodin, *et al.*, Fiz. Tekh. Poluprovodn. (St. Petersburg) **36**, 109 (2002) [Semiconductors **36**, 102 (2002)].
8. M. D. Efremov, V. A. Volodin, L. I. Fedina, *et al.*, Pis'ma Zh. Tekh. Fiz. **29** (13), 89 (2003) [Tech. Phys. Lett. **29**, 569 (2003)].
9. J. E. Smith, Jr., M. H. Brodsky, B. L. Crowder, *et al.*, Phys. Rev. Lett. **26**, 642 (1971).
10. Z. Iqbal, S. Veptek, A. P. Webb, *et al.*, Solid State Commun. **37**, 993 (1981).
11. D. Beeman, R. Tsu, and M. F. Thorpe, Phys. Rev. B **32**, 874 (1985).
12. R. Beserman, Yu. L. Khait, A. Chack, *et al.*, J. Non-Cryst. Solids **299–302**, 736 (2002).
13. *Topics in Applied Physics*, Vol. 8: *Light Scattering in Solids*, Ed. by M. Cardona (Springer-Verlag, Berlin, 1975).
14. T. Sameshima and S. Usui, J. Appl. Phys. **70**, 1281 (1991).

Translated by P. Pozdeev

Technical Physics Letters, Vol. 31, No. 2, 2005, pp. 132–134. Translated from Pis'ma v Zhurnal Tekhnicheskoĭ Fiziki, Vol. 31, No. 4, 2005, pp. 1–5.

Determining the Parameters of Electron Traps in Inhomogeneous Layers by Method of Thermionic Emission

S. N. Nagornykh[a,*] and V. I. Pavlenkov[b,]**

[a] *Nizhni Novgorod State Pedagogical University, Nizhni Novgorod, Russia*
[b] *Arzamas State Pedagogical University, Arzamas, Russia*
*e-mail: * algoritm@sandy.ru; ** agpi@nts.ru*
Revised manuscript received September 2, 2004

Abstract—Quasi-stationary nonlinear variation of the density of filled electron traps in the course of thermionic emission from the surface oxide layer on a metal cathode is theoretically described. Expressions for the electron affinity, energy, and density of electron traps in this dielectric layer are obtained. Numerical estimates of the electron trap parameters are obtained based on the results of measurements of the temperature dependence of thermionic emission from the porous surface oxide layer of an iron–nickel alloy. © *2005 Pleiades Publishing, Inc.*

The kinetics of thermionic emission from the surface dielectric oxide layer on a metal electrode can be described [1–3] in terms of the quasi-stationary approximation of the Blokhintsev equation for conduction electrons. Previously, the energy of electron traps has been determined in a linear approximation with respect to the density of occupied traps, assuming that their number is small relative to the total density of electron traps [1, 4]. However, this linear description is inapplicable in the case of inhomogeneous dielectric layers where the time of emission of the conduction electrons is much shorter than the time of their capture on the empty traps. Investigations of the temperature dependence of thermionic emission from thin inhomogeneous materials are advantageous over the traditional measurements of thermostimulated currents, since the emission currents are six to seven orders of magnitude lower than the latter currents and are not influenced by contacts [5].

This Letter presents an attempt at a theoretical description of the parameters of electron traps in the case of a nonlinear variation of their density in the oxide layer. The results are applied to a porous oxide on the surface of an iron–nickel alloy used in liquid and gas filters.

Electron trap parameters. The variation of the densities of free electrons (N), traps (ν), and emission current (J) is described by the following system of equations [1, 2]:

$$\frac{dN}{dt} = p\nu - A_1(\nu_1 - \nu)N - A_2N, \quad (1)$$

$$\frac{d\nu}{dt} = -p\nu + A_1(\nu_1 - \nu)N, \quad (2)$$

$$J = LA_2N. \quad (3)$$

Here, $p = p_0\exp(-\varepsilon/kT)$ is the probability of thermal ionization of an electron trap with an energy ε below the conduction band bottom in the oxide, $A_1 = \sigma\sqrt{2kT/m}$ is the probability of electron capture by an empty trap, m is the effective electron mass, σ is the effective capture cross section, $A_2 = a_2T\exp(-\chi/kT)$ is the probability of electron emission from a filled trap into vacuum, χ is the electron affinity, ν_1 is the total density of empty and filled traps, and L is the emitting layer thickness.

In the quasi-stationary case ($dN/dt = 0$) at a constant rate of sample heating ($b = dT/dt$ = const) and a small number of filled electron traps ($\nu \ll \nu_1$), Eqs. (1) and (2) can be reduced to the following equation:

$$\frac{d\nu}{dT} + \frac{pA_2}{2b(A_1\nu_1 + A_2)}\nu + \frac{pA_1}{3b(A_1\nu_1 + A_2)}\nu^2 = 0. \quad (4)$$

Under the assumption that $A_2 \gg A_1(\nu_1 - \nu)$, this equation simplifies to

$$\frac{d\nu}{dT} - \frac{p}{2b}\left(\frac{A_1\nu_1}{A_2} - 1\right)\nu + \frac{pA_1}{3bA_2}\nu^2 = 0, \quad (5)$$

and has the following solution:

$$\nu = \exp\left(\int_{T_0}^{T} BdT\right)\left[\int_{T_0}^{T} C\exp\left(\int_{T_0}^{T} BdT\right)dT + \frac{1}{\nu_0}\right]^{-1}, \quad (6)$$

1063-7850/05/3102-0132$26.00

where

$$B = \frac{p}{2b}\left(\frac{A_1\nu_1}{A_2} - 1\right) = \frac{a_0 p}{2b}\left[\frac{\exp(\chi/kT)}{\sqrt{T}} - 1\right], \quad (7)$$

$$C = \frac{pA_1}{3bA_2} = \frac{a_0 p \exp(\chi/kT)}{3\nu_1 b\sqrt{T}}, \quad (8)$$

$$a_0 = \frac{\nu_1\sigma_0}{a_2}\sqrt{\frac{2k}{m}},$$

and ν_0 is the initial density of filled traps.

Using expressions (3) and (6), the temperature dependence $J(T)$ of the emission current density can be written as

$$J = Lp\nu. \quad (9)$$

Taking the first derivative of $J(T)$ with respect to the temperature and equating it to zero, we obtain the following expression for the maximum current density:

$$J_M = \frac{3LA_{2M}}{2A_{1M}}\left(\frac{2b\varepsilon}{kT_M^2} - p_M + \frac{A_{1M}\nu_1 p_M}{A_{2M}}\right), \quad (10)$$

where T_M is the temperature corresponding to this maximum.

The ratio of the derivative J_i' of the emission current density with respect to the temperature, taken at the temperature T_i, to the emission current density at this temperature can be written as

$$\frac{J_i'}{J_i} = \frac{1}{2b}\left(\frac{2b\varepsilon}{kT_i^2} - p_i + \frac{A_{1i}\nu_1 p_i}{A_{2i}} - \frac{2A_{1i}}{3A_{2i}L}J_i\right). \quad (11)$$

Equations (11) relative to ε and χ are valid at any nonzero temperature ($T_i \neq 0$) such that $J_i \neq 0$. Introducing the notation $\alpha_i = J_i/J_M$, $\beta_i = T_i/T_M$, and $\gamma_i = J_i'/J_M$ and using Eqs. (10) and (11), we obtain a relation

$$\sqrt{\beta_i}D_i \exp\left[-\frac{\chi}{kT_M}\left(\frac{1}{\beta_i} - 1\right)\right] + \alpha_i E_M = \frac{a_0 F_i}{2b\sqrt{T_M}}\exp\frac{\chi}{kT_M}, \quad (12)$$

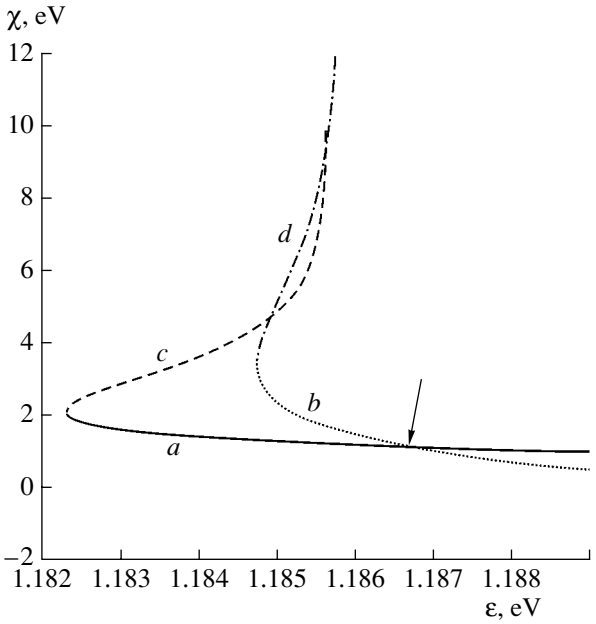

Graphical solution of a system of two equations (14): (*a*, *c*) $\chi(\varepsilon)$ curve constructed for the pair of temperatures T_1, T_2 using (+) and (–) signs at the root in the numerator on the right-hand side, respectively; (*b*, *d*) same for T_2, T_3. The arrow indicates a physically meaningful solution in the region of positive χ.

where

$$D_i = \gamma_i + \frac{p_i}{2b} - \frac{\varepsilon}{kT_i^2}, \quad E_M = \frac{b\varepsilon}{kT_M^2} - \frac{p_M}{2b},$$
$$F_i = p_i - \alpha_i p_M.$$

For two temperatures, T_1 and T_2, related as

$$T_2 = 2(T_1^{-1} + T_M^{-1})^{-1}, \quad (13)$$

a solution to the system of equations (12) with $T_i = T_1$, T_2 can be expressed as

$$\chi(\varepsilon) = \frac{kT_M T_2}{T_2 - T_M}\ln\left[\frac{\sqrt{\beta_2}F_1D_2 \pm \sqrt{\beta_2(F_1D_2)^2 - 4\sqrt{\beta_1}F_2D_1E_M(\alpha_1F_2 - \alpha_2F_1)}}{2\sqrt{\beta_1}F_2D_1}\right]. \quad (14)$$

Using the system of equations (12) with $T_i = T_2$, T_3 related by a condition analogous to formula (13), we obtain another function $\chi(\varepsilon)$ of type (14). A graphical solution of the system of two equations of the type of Eq. (14) gives the values of χ and ε.

Finally, we can use expression (9) for determining ν_0 and ν_1 for a given emission current density J. The value of a_0 in Eq. (6) and (9) can be calculated using relation (12) for a given temperature and the values of χ and ε determined as described above.

Experimental results and numerical estimates. Experiments with an oxidized iron–nickel alloy showed the typical dome-shaped temperature dependence of the thermionic emission current measured

with a channeltron in the range of currents $(1–10^4) \times 10^{-19}$ A at a constant heating rate in a vacuum of 10^{-5} Pa. The observed behavior of the thermionic current density was in qualitative agreement with relation (9).

For a heating rate of $b = 0.23$ K/s, the maximum of the emission current was observed at $T_M = 612$ K. The values of the parameters α_i, β_i, and γ_i determined from the plot of $J(T)$ for $T_1 = 562$ K, $T_2 = 584$ K, and $T_3 = 598$ K were as follows: $\alpha_i = 0.42, 0.72, 0.90$; $\beta_i = 0.918, 0.954, 0.977$; $\gamma_i = 0.023, 0.021, 0.014$ for $i = 1, 2, 3$, respectively. The graphical solution of a system of two equations (14) for the pairs of temperatures T_1, T_2 and T_2, T_3 is illustrated in the figure. This solution yields $\varepsilon = 1.187$ eV, $\chi = 1.154$ eV, and $a_0 = 10^{-9}$ K$^{1/2}$, which are close to the published reference values for iron oxide [6].

The densities of traps were calculated using formula (9) for $L = 10^{-8}$ m, $J_1 = 10^6$ m^{-2} s^{-1} (measured at $T = T_1$), and $J_2 = 1.7 \times 10^6$ m^{-2} s^{-1} (measured at $T = T_2$). These values ($\nu_1 = 2.3 \times 10^{16}$ m^{-3} and $\nu_0 = 1.0 \times 10^{15}$ m^{-3}) are consistent with real values. Therefore, the proposed method of thermionic emission can be used for the characterization of electron traps in inhomogeneous porous oxides of iron-based alloys.

REFERENCES

1. S. N. Nagornykh, M. E. Gerenrot, and I. E. Kurov, Fiz. Khim. Obrab. Mater. **5**, 32 (1982).
2. V. V. Bichevin, in *Radiation-Induced Phenomena in Solids* (Ural'sk. Politekh. Inst., Sverdlovsk, 1980), pp. 17–23 [in Russian].
3. B. M. Nosenko and V. Ya. Yaskolko, Tr. Tashkent. Univ. **221**, 84 (1963).
4. J. Kanturek, Czech. J. Phys., No. 6, 349 (1956).
5. T. V. Panchenko, Fiz. Tverd. Tela (St. Petersburg) **41**, 1006 (1999) [Phys. Solid State **41**, 916 (1999)].
6. *The Oxide Handbook*, Ed. by G. V. Samsonov (Metallurgiya, Moscow, 1978; Plenum Press, New York, 1982).

Translated by P. Pozdeev

Technical Physics Letters, Vol. 31, No. 2, 2005, pp. 135–137. Translated from Pis'ma v Zhurnal Tekhnicheskoĭ Fiziki, Vol. 31, No. 4, 2005, pp. 6–12.

Boundary Effect on the Mixing and Transport of Passive Impurities in a Nonstationary Flow

K. V. Koshel and D. V. Stepanov

Pacific Institute of Oceanology, Far-Eastern Division, Russian Academy of Sciences, Vladivostok, Russia

Received August 9, 2004

Abstract—The simplest model of a point topographic vortex situated near a linear boundary in a nonstationary incident flow is considered. The results of numerical experiments reveal a new feature in the behavior of trajectories that is not observed in absence of the boundary. A criterion for distinguishing such trajectories is proposed. © *2005 Pleiades Publishing, Inc.*

Introduction. A broad class of models exhibiting chaotic properties is offered by the Hamiltonian systems possessing one and a half degrees of freedom. By chaotic behavior we imply the exponentially fast recession of two initially close trajectories [1]. In geophysical hydrodynamics, this phenomenon is called chaotic advection [2]. The relative simplicity of Hamiltonian systems makes possible their use for at least a qualitative description of real models in geophysical hydrodynamics. However, a necessary condition is that the corresponding stream function obeys certain dynamical relations (i.e., is dynamically consistent). Such a current function can be constructed using the background flow theory [3].

Dynamically consistent stream functions and the formalism of the theory of dynamical systems were used in investigations of the chaotic behavior of fluid particles within the framework of topographic vortex models assuming elliptical [4] and Gaussian [5] vortex shapes in the nonstationary incident flow. The mechanism of chaotic mixing in a point vortex model was studied in [6]. Previously, we considered a point topographic vortex situated near a linear boundary in a nonstationary incident flow [7]. This model is equivalent to that with two stationary point vortices in the infinite region. Using a variant of the perturbation theory proposed by Gledzer [8], it was established that the thickness of a stochastic layer increases with the degree of influence of the boundary.

In this study, we used the simplest model of a point topographic vortex situated near a linear boundary in a nonstationary incident flow [7] for numerical simulation of the effect of a linear boundary on the behavior of fluid particles in the flow.

Formulation of the problem. Consider the velocity field of a two-dimensional flow of an incompressible nonviscous fluid induced by a point topographic vortex situated near a linear boundary. In a dimensionless form, the stream function and the system of equations describing the advection of particles of a passive impurity are as follows [7]:

$$\Psi = -W(t)y + \ln\left(\frac{x^2 + (y+1)^2}{x^2 + (y-1)^2}\right),$$

$$\begin{cases} \dfrac{dx}{dt} = -\dfrac{\partial \Psi}{\partial y} \\ = W(t)y - 4\left(\dfrac{x^2 - y^2 + 1}{(x^2 + (y+1)^2)(x^2 + (y-1)^2)}\right), \\ \dfrac{dy}{dt} = \dfrac{\partial \Psi}{\partial x} = -\left(\dfrac{8yx}{(x^2 + (y+1)^2)(x^2 + (y-1)^2)}\right), \end{cases} \quad (1)$$

where $W(t)$ is the velocity of the incident flow; (x, y) and t are the dimensionless coordinates and time, respectively; and the center of a submerged hill generating the vortex occurs at a point with the coordinates (0, 1). For $W(t)$ = const, system (1) has one elliptical and one or two hyperbolic singularities (depending on the incident flow velocity) [7]. The phase space is divided by a separatrix into two regions corresponding to a finite (vortex region, VR) and infinite (flow region, FR) motion. Particles occurring in the VR cannot penetrate into the FR and vice versa.

In the presence of a small periodic perturbation in the incident flow velocity, the pattern in the phase space of system (1) exhibits significant changes, whereby the trajectories of fluid particles may exhibit chaotic behavior (depending on the initial conditions) and a stochastic layer appears in the vicinity of the unperturbed separatrix, in which the VR and FR regions may exchange impurity particles. It has been established [8] that the thickness of a stochastic layer in the vicinity of the hyperbolic point is proportional to the square root of the perturbation amplitude. As the influence of the boundary grows, the stochastic layer thickness increases and becomes proportional to the cubic root of the perturbation amplitude [7]. However, as will be demonstrated below, the increase in the thickness of this layer is not

1063-7850/05/3102-0135$26.00

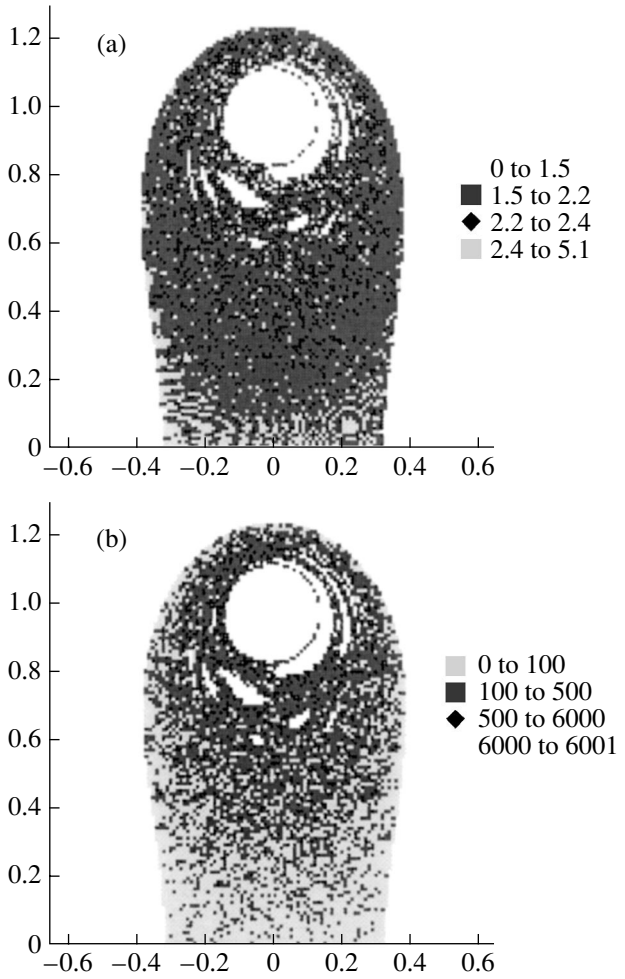

Fig. 1. Distributions of (a) the accumulated Lyapunov exponent and (b) the tracer lifetime, reduced to those in the initial moment of time (for $W_0 = 3.6$ and $\omega = 75.0$).

the only manifestation of the presence of a linear boundary in the system under consideration.

Numerical experiments. Numerical modeling was performed using the Stoer–Bulirsch method [9] with modified step. The incident flow was set as

$$W(t) = W_0(1 - \delta\sin(\omega t)), \qquad (2)$$

where $\delta = 0.1$ and the average velocity of the incident flow ($W_0 = 3.6$) corresponds to a strong influence of the boundary. In the initial moment of time, 8250 tracers were uniformly distributed in the VR. Since the fluid particles exhibit regular motion in a small vicinity of the vortex center, we ignored the initial conditions for (x_0, y_0) in the vicinity such that $\sqrt{x_0^2 + y_0^2} \le 0.05$.

The number of markers (of the total of 8250) with α values above a preset threshold for $W_0 = 3.6$ and 4.6 (strong and weak boundary effects, respectively)

α above	$W_0 = 3.6$	$W_0 = 4.6$
0.1	3991	287
0.41	1932	1
1.0	532	0
3.03	1	0

In the first experiment, we determined the frequency of the incident flow for which the number of tracers leaving the VR is maximum. A tracer was considered to be lost from the VR when its trajectory crossed the line $x = 2.0$. The integration interval was chosen within $t = 80000.0$ (after which the tracers cease to leave the VR). At an average velocity of the incident flow $W_0 = 3.6$, the optimum frequency was $\omega = 75.0$.

The degree of chaos would be naturally characterized by the extent of recession between the initially closely spaced trajectories, that is, by the Lyapunov exponent λ. However, calculation of this parameter was impossible because of the open character of the system under consideration. For this reason, we calculated the λ values gained over a finite period of time (accumulated Lyapunov exponent [5]). In addition, we determined the tracer lifetime as the time for which it stayed in the VR. The integration interval was chosen within $t = 6000.0$ (by which time most of the tracers exhibiting chaotic behavior leave the VR).

Figure 1 shows the distributions of the accumulated Lyapunov exponent (a) and the tracer lifetime (b) reduced to those in the initial moment of time. The tracer trajectories exhibit behaviors of various types depending on the initial conditions. The first type corresponds to regular trajectories occurring in islands of regular behavior, which are characterized by a small accumulated Lyapunov exponent. The second type corresponds to trajectories very rapidly leaving the VR, which have small lifetimes and large λ values. Trajectories of the third type exhibit chaotic behavior at the initial moment of time and then are trapped by a regular structure (or vice versa). These trajectories are characterized by intermediate λ values and relatively large lifetimes.

As the influence of the boundary increases, there appear trajectories whose behavior obeys none of the above scenarios. These are trajectories of the fourth type, which are characterized by large lifetimes and large λ values. In order to identify such trajectories, we introduced another characteristic of chaotic behavior, defined as the maximum distance dy between two sequential intersections of the trajectory and the Oy axis for $y < 1$. Using all three parameters (lifetime, λ, and dy), we characterized each tracer by the quantity $\alpha = \frac{t}{T}\frac{\lambda}{\lambda^*}dy$, where T is the time interval corresponding to the effective loss of the passive impurity from the VR, and λ^* is the average value of the accumulated Lyapunov exponent for all tracers.

Data illustrating the variation of the number of tracers having α values above a certain preset threshold for

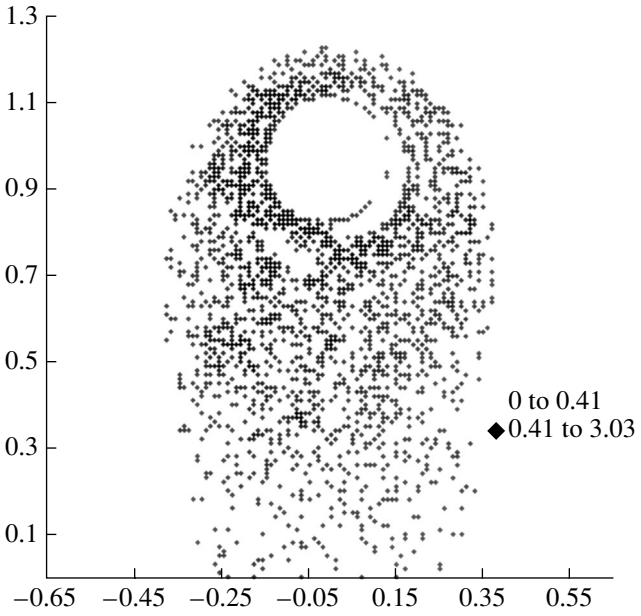

Fig. 2. Distribution of the parameter α reduced to the initial positions of markers (for $W_0 = 3.6$ and $\omega = 75.0$).

$W_0 = 4.6$ and 3.6 are given in the table. Evidently, the maximum value of $\alpha = 0.41$ for $W_0 = 4.6$ (weak boundary effect) should be considered as a criterion for identifying trajectories of the fourth type. Then, the number of trajectories belonging to this type for $W_0 = 3.6$ is on the order of 23.4% of the total number of tracers.

Figure 2 illustrates the distribution of α values reduced to those in the initial moment of time for $W_0 = 3.6$. Judging from this pattern, we may conclude that the initial positions of trajectories of the fourth type are found in the entire VR, but the region of initial conditions for such tracers is not continuous: any vicinity of a tracer of the fourth type contains tracers of the second and third type and (in the regions close to the islands of regular behavior) even of the first type.

Conclusions. We have considered a Hamiltonian system possessing one and a half degrees of freedom, which describes the motion of particles of an incompressible nonviscous fluid in a nonstationary flow incident on a point vortex situated near a linear boundary. As the boundary effect increases, there appear trajectories of the fourth type characterized by large values of both the lifetime and the accumulated Lyapunov exponent. Trajectories of this type alternatively stick to one or another island of regular behavior, thus covering a relatively large area of the VR in phase space. This behavior is typical of models of the so-called closed type [10]. It should be emphasized that the behavior of the fourth type was not revealed by the models studied previously [4–6]. This fact indicates that the boundary not only influences the chaotic properties of trajectories but generates a new type of their behavior as well.

Acknowledgments. The authors are grateful to V.V. Novotryasov for fruitful discussions of the results.

This study was supported by the Russian Foundation for Basic Research and (project. no. 03-05-65214) and the Far-Eastern Division of the Russian Academy of Sciences (project. nos. 03-3-A-07-080 and 03-3-G-07-077).

REFERENCES

1. J. M. Ottino, *The Kinematics of Mixing: Stretching, Chaos and Transport* (Cambridge University Press, Cambridge, 1989).
2. H. Aref, J. Fluid Mech. **143**, 1 (1984).
3. V. F. Kozlov, Izv. Akad. Nauk, Fiz. Atmos. Okeana **31**, 245 (1995).
4. Yu. G. Izrailsky, V. F. Kozlov, and K. V. Koshel, Phys. Fluids **16**, 3173 (2004).
5. V. F. Kozlov and K. V. Koshel, Izv. Akad. Nauk, Fiz. Atmos. Okeana **37**, 378 (2001).
6. M. V. Budyansky and S. V. Prants, Pis'ma Zh. Tekh. Fiz. **27** (12), 51 (2001) [Tech. Phys. Lett. **27**, 508 (2001)].
7. V. F. Kozlov, K. V. Koshel, and D. V. Stepanov, Dal'nevostochn. Mat. Zh. **2**, 89 (2001).
8. A. E. Gledzer, Izv. Akad. Nauk, Fiz. Atmos. Okeana **35**, 838 (1999).
9. J. Stoer and R. Bulirsch, *Introduction to Numerical Analysis* (Springer-Verlag, New York, 1976).
10. F. Sotiropoulos, Y. Ventikos, and T. C. Lackey, J. Fluid Mech. **444**, 257 (2001).

Translated by P. Pozdeev

Technical Physics Letters, Vol. 31, No. 2, 2005, pp. 138–139. Translated from Pis'ma v Zhurnal Tekhnicheskoĭ Fiziki, Vol. 31, No. 4, 2005, pp. 13–16.

Magnetron Sputter Deposition of $(SiC)_{1-x}(AlN)_x$ Solid Solution Films

M. K. Guseĭnov, M. K. Kurbanov, G. K. Safaraliev, and B. A. Bilalov

Dagestan State University, Makhachkala, Dagestan, Russia

e-mail: dgu@dgu.ru

Received June 8, 2004

Abstract—Magnetron sputtering of polycrystalline SiC–AlN targets was used to obtain films of $(SiC)_{1-x}(AlN)_x$ solid solutions on silicon carbide (6H-SiC) substrates heated to a temperature in the range T = 500–1200°C. The deposits were characterized with respect to structure, composition, and optical absorption. It is demonstrated that the films obtained on 6H-SiC substrates at $T \geq 1000$°C possess a single crystal structure. The compositions of $(SiC)_{1-x}(AlN)_x$ films are close to those of the corresponding SiC–AlN targets. © *2005 Pleiades Publishing, Inc.*

In recent years, wide-bandgap semiconductors based on solid solutions of silicon carbide (SiC) have received much attention as a potential base for the creation of new optoelectronic and high-temperature microelectronic devices. The best prospects in this respect have been demonstrated by solid solutions of the $(SiC)_{1-x}(AlN)_x$ system [1]. The synthesis of single crystals of $(SiC)_{1-x}(AlN)_x$ solid solutions was studied in [2–5]. However, no data were reported on the growth of films of such solid solutions by means of magnetron sputtering of polycrystalline SiC–AlN targets.

The aim of this study was to obtain films of $(SiC)_{1-x}(AlN)_x$ solid solutions on silicon carbide (SiC) and sapphire (Al_2O_3) substrates by means of magnetron sputtering of polycrystalline SiC–AlN targets in an argon atmosphere and to study the effect of the substrate temperature during deposition on the film structure.

Polycrystalline SiC–AlN targets with different contents of AlN (C_{AlN} = 10–50 wt %) were prepared by cold pressing of mixed submicron powders of SiC and AlN components at a pressure of 4 MPa, followed by sintering at 1700–1800°C for 60 min in a nitrogen atmosphere. The targets were sputtered in argon at a pressure of 8×10^{-2} Pa with the aid of a planar dc magnetron operating at a discharge current of 70 mA. The films were deposited at a rate of 0.1–0.15 nm/s onto single crystal plates of 6H(0001) silicon carbide polytype (6H-SiC) and Al_2O_3(0001) (sapphire) heated to 500–1200°C. Prior to deposition, the target was sputtered for 15 min aside from the substrate holder in order to attain a stationary sputter yield regime.

The structure of deposited $(SiC)_{1-x}(AlN)_x$ films with a thickness of 2–3 μm was studied by X-ray diffraction on a DRON-2 diffractometer using CuK_α radiation. The results of these measurements showed that films deposited at a substrate temperature of T = 500°C are amorphous. Deposits obtained at T > 700°C exhibited a transition to a polycrystalline structure. At $T \geq$ 1000°C, we obtained single crystal $(SiC)_{1-x}(AlN)_x$ films with a wurtzite (2H) crystal structure. There was no evidence of the presence of a second phase. The X-ray rocking curves showed that the structural perfection of $(SiC)_{1-x}(AlN)_x$ films deposited on 6H-SiC at $T \geq 1000$°C is comparable with that of SiC substrates. The $(SiC)_{1-x}(AlN)_x$ films grown on sapphire substrates at T > 1000°C exhibited an (0001)-oriented texture with 0.5°–3° grain misorientation.

Figure 1 shows typical X-ray diffractograms of a 6H-SiC substrate and a $(SiC)_{0.7}(AlN)_{0.3}$ solid solution

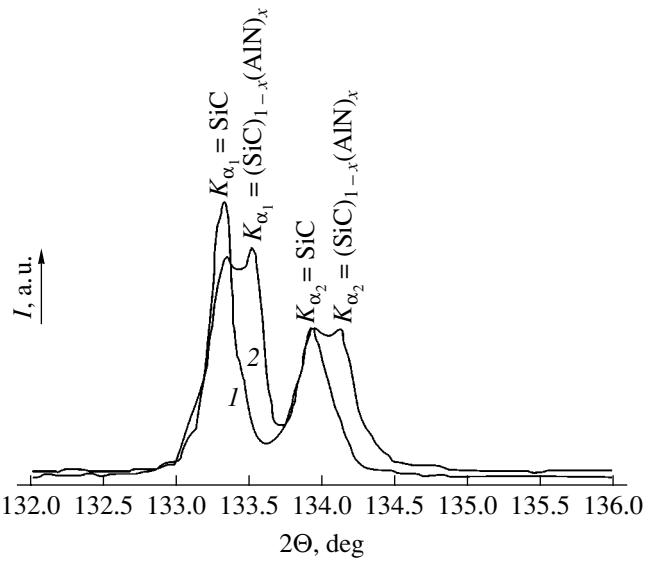

Fig. 1. X-ray diffractograms of (*1*) a 6H-SiC substrate and (*2*) a $(SiC)_{0.7}(AlN)_{0.3}$ solid solution film grown on this substrate.

1063-7850/05/3102-0138$26.00 © 2005 Pleiades Publishing, Inc.

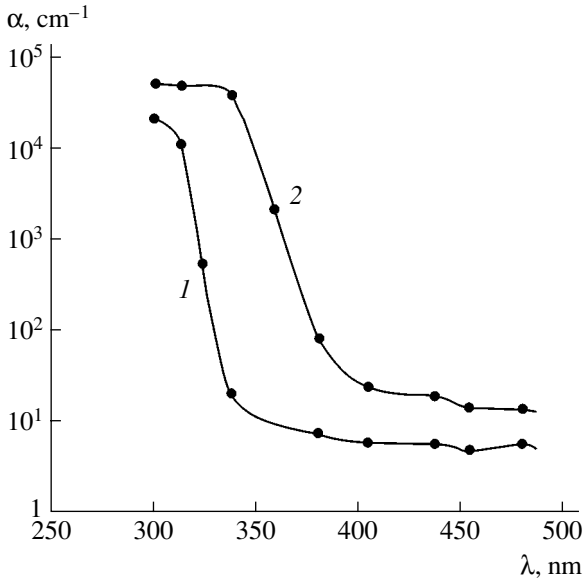

Fig. 2. Optical absorption spectra of the films of $(SiC)_{1-x}(AlN)_x$ solid solutions with $x = 0.3$ (*1*) and 0.46 (*2*) on sapphire substrates.

film grown on this substrate. At a sufficiently high resolution of the spectrograph, a filtered CuK_α radiation has to be registered in the form of a doublet ($K_{\alpha1}$ and $K_{\alpha2}$), just as is observed in the diffraction pattern presented. In addition to the peaks due to the substrate, the X-ray diffractogram shows pronounced maxima related to the solid solution. A small shift of the diffraction peaks is explained by close values of the lattice parameters of SiC and $(SiC)_{0.7}(AlN)_{0.3}$. The absence of other reflections is evidence of a single crystal character of the deposit. The angular positions of reflections shift consistently with variations in the composition, which is indicative of the formation of homogeneous solid solutions.

The elemental compositions of deposited films were studied on an electron microscope with an electron microprobe analyzer (LEO-1450). The results of these measurements showed that the distribution of solid solution components (Si, C, Al, N) is homogeneous both in depth and in the lateral direction, while the deposit composition is close to that of the corresponding SiC–AlN target.

The optical absorption spectra of the films of $(SiC)_{1-x}(AlN)_x$ solid solutions deposited onto sapphire substrates at $T = 1000°C$ were measured using a Lambda 900 spectrophotometer in a wavelength interval from 0.3 to 0.5 μm. Figure 2 shows the absorption spectra of the samples with $x = 0.3$ and 0.46. The observed shift of the absorption edge toward shorter wavelengths with increasing content of SiN in the composition reflects an increase in the bandgap width of the $(SiC)_{1-x}(AlN)_x$ solid solution.

In conclusion, the results of our investigation showed the possibility of controlled synthesis of homogeneous films of wide-bandgap $(SiC)_{1-x}(AlN)_x$ solid solutions on 6H-SiCand Al_2O_3 substrates, with the ratio of components determined by the target composition.

Acknowledgments. This study was supported by the Ministry of Education of the Russian Federation, project no. A03-2.9-555.

REFERENCES

1. R. A. Yankov, M. Voelskow, W. Kreissig, *et al.*, Pis'ma Zh. Tekh. Fiz. **23** (16), 6 (1997) [Tech. Phys. Lett. **23**, 617 (1997)].
2. Sh. A. Nurmagomedov, A. N. Pikhtin, V. N. Razbegaev, *et al.*, Pis'ma Zh. Tekh. Fiz. **12**, 1043 (1986) [Sov. Tech. Phys. Lett. **12**, 431 (1986)].
3. V. A. Dmitriev, L. B. Elfimov, I. Yu. Linkov, *et al.*, Pis'ma Zh. Tekh. Fiz. **17** (6), 50 (1991) [Sov. Tech. Phys. Lett. **17**, 214 (1991)].
4. G. K. Safaraliev, M. K. Kurbanov, N. V. Ofitserova, and Yu. M. Tairov, Izv. Ross. Akad. Nauk, Neorg. Mater., No. 6, 1 (1995).
5. M. K. Kurbanov, B. A. Bilalov, Sh. A. Nurmagomedov, and G. K. Safaraliev, Fiz. Tekh. Poluprovodn. **35**, 216 (2001) [Semiconductors **35**, 209 (2001)].

Translated by P. Pozdeev

Technical Physics Letters, Vol. 31, No. 2, 2005, pp. 140–142. Translated from Pis'ma v Zhurnal Tekhnicheskoĭ Fiziki, Vol. 31, No. 4, 2005, pp. 17–22.

Modeling Plastic Deformation and Fracture of Porous Materials

V. V. Polyakov*, A. V. Egorov, and A. A. Lependin

Altai State University, Barnaul, Altai, Russia

** e-mail: polyakov@phys.dcn-asu.ru*

Revised manuscript received September 27, 2004

Abstract—Strain hardening of a porous material was numerically modeled. The corresponding stress–strain (σ–ε) curves, the ultimate strength, and the strain at break were calculated for iron with a relative porosity in the interval from 0 to 30%. Anomalous behavior of these characteristics is observed at a porosity corresponding to the percolation transition from isolated pores to the "infinite" pore cluster. The proposed model adequately describes the available experimental data. © *2005 Pleiades Publishing, Inc.*

Plastic straining and fracture of materials possessing sharply inhomogeneous structures exhibit specific features and are still insufficiently studied. Of special interest in this respect is the behavior of porous materials, which can be considered as heterophase media with ultimately differing properties of the two phases (solid framework and pores) [1]. The behavior of such media on straining is determined by specific physical mechanisms [2]. The dependence of the strength and plasticity of materials on the characteristics of porosity can be studied by modeling these mechanisms.

This Letter presents a mathematical model describing the effect of porosity on the strain hardening and fracture of metals under tensile loading conditions.

The material was characterized by the degree of porosity P defined as the total fraction of voids. The effect of porosity on the strain hardening curves $\sigma = \sigma(\varepsilon)$ was considered taking into account the contributions of two mechanisms. The first mechanism is related to the geometric loss of strength in strained compact regions of a porous solid, which is caused by the presence of voids leading to a decrease in the effective sample cross section as compared to that in the compact material. The second mechanism is related to the nucleation and propagation of microcracks originating from the pores acting as the main stress concentrators in porous solids. Accordingly, the total strain is expressed as

$$\varepsilon = \varepsilon_1 + \varepsilon_2, \quad (1)$$

where ε_1 and ε_2 denote the contributions due to the first and second mechanisms, respectively. The strain hardening curve $\sigma_k = \sigma_k(\varepsilon_k)$ of the corresponding compact material was assumed to be known (here, σ_k and ε_k are the stress and strain at $P = 0$).

The loss of strength caused by the first mechanism is manifested in that the stress σ in a sample with cross section S is distributed only in the framework with the effective cross section S_K. Writing the force balance as $\sigma S = \sigma_K S_K$, we obtain

$$\sigma = \sigma_K \frac{S_K}{S}. \quad (2)$$

The ratio of the cross sections S_K/S can be determined using a geometric model of the porous material structure [3]. In constructing such models, it is important to take into account a change in the sample topology in the case of formation of an "infinite" cluster from isolated pores when the porosity reaches a level corresponding to the percolation threshold P_0 [4]. The fraction of closed porosity for a given P value was expressed in terms of the coefficient α defined as

$$\alpha = \begin{cases} 1, & P \le P_0, \\ 0, & P > P_0. \end{cases} \quad (3)$$

Within the framework of the unit cell method, the S_K/S ratio in the entire range of porosity variation is expressed as [3]

$$\frac{S_K}{S} = \alpha(1 - f_1^2) + (1 - \alpha)(1 - f_2^2), \quad (4)$$

where the first term on the right-hand side refers to the case of low porosity ($P \le P_0$), while the second term describes the case of high porosity exceeding the percolation threshold ($P > P_0$). The values of the coefficients f_1 and f_2 for a unit cell with cubic symmetry are expressed via the porosity P as

$$f_1^3 = P, \quad 3f_2^2 - 2f_2^3 = P. \quad (5)$$

Using formulas (2) and (4) and the known $\sigma_k = \sigma_k(\varepsilon_k)$ relation, it is possible to determine the stress σ

operating in the given porous material at a preset strain $\varepsilon_1 = \varepsilon_K$.

The loss of stress caused by the second mechanism (related to the growth of microcracks) was modeled as follows. The strain contribution ε_2 was expressed as the ratio of the crack opening δ to the average distance h between pores (corresponding to the solid framework "beam" size in the unit cell model):

$$\varepsilon_2 = \frac{\delta}{h}. \quad (6)$$

On the other hand, the crack opening δ is related to the stress intensity factor K_I as [5, 6]

$$\delta = \frac{cK_I^2}{E_K\sigma_{TK}}, \quad (7)$$

where E_K and σ_{TK} are the Young modulus and the yield stress of the compact material, respectively, and c is a factor (on the order of unity) that takes into account the presence of a plastic band.

The stress intensity factor in the compact region of the porous material is related to the crack length l as

$$K_I = \sigma_k\sqrt{\pi l} = \sigma_k\sqrt{\pi(l_0 + \Delta l)}, \quad (8)$$

where l_0 is the initial crack length, Δl is an increase in the crack length related to the change in the stress intensity factor from K_{I0} (corresponding to the onset of crack development) to the current value K_I (corresponding to the given stress σ). In the approximation of brittle fracture with subcritical crack growth, the value of Δl can be expressed as [5]

$$\Delta l = d\left(\ln\frac{K_C^2 - K_{I0}^2}{K_C^2 - K_I^2} - \frac{K_I^2 - K_{I0}^2}{K_C^2}\right), \quad (9)$$

where K_C is the critical stress intensity factor at break and d is a parameter determined by features of the crack propagation process in a particular material.

Using formulas (8) and (9) and the given values of stress in the compact part of the porous material, it is possible to calculate the stress intensity factors (as implicit functions). Then, the additional strain ε_2 is determined using relation (6).

The curves of strain hardening were calculated until the ultimate values of stress (σ_B) and strain at break (ε_B) were reached, which resulted from the action of one of the two possible mechanisms. These ultimate values were determined using the conditions derived from relations (2) and (6). The calculations were performed for iron with a degree of porosity varying from 0 to 0.3. The values of K_C, K_{I0}, and d were taken from experimental data for the compact Armco iron. The initial stress–strain curve for $P = 0$ was determined from the results of tensile tests on the same material. The values of l_0 and h were experimentally determined for the given porous material, and the percolation threshold was taken equal to $P_0 = 0.1$. The results of numerical calculations were represented as $\sigma = \sigma(\varepsilon)$ curves for various fixed values of P and as the curves of σ_B and strain ε_B versus P.

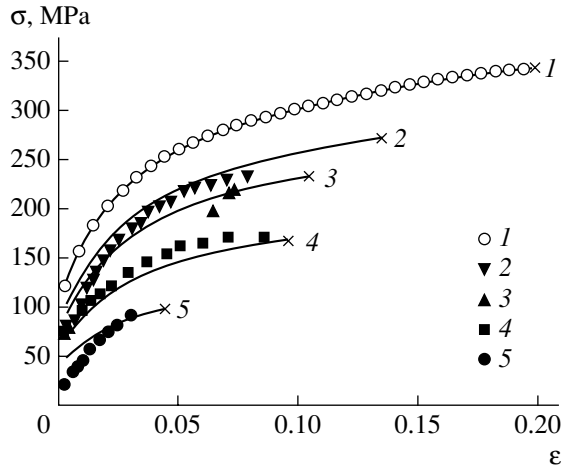

Fig. 1. Experimental (points) and calculated (curves) stress–strain diagrams for iron with various values of porosity P: (*1*) 0; (*2*) 0.05; (*3*) 0.1; (*4*) 0.15; (*5*) 0.3. Crosses indicate the break points.

Figure 1 shows the strain hardening curves of iron calculated for various values of porosity (curve *1* is the approximation of experimental data, and curves *2–5* are the results of numerical calculations for $P = 0.05$, 0.1, 0.15, and 0.3, respectively). As can be seen from this figure, the stress–strain curves are monotonic in the entire range of variables. The main feature of these curves is a rapid drop in the slope with increasing porosity, which reflects a decrease in the material resistance to straining as a result of the loss of strength caused by porosity.

Figure 2 shows the values of stress and strain at break, σ_B and ε_B, calculated as functions of P (the corresponding points are indicated by crosses in Fig. 1). As can be seen from these curves, the ultimate strain ε_B declines from a monotonic decrease with increasing porosity, which is manifested by an anomaly at $P \sim 0.1$. An analogous feature, although somewhat less pronounced, is observed in the ultimate stress σ_B. These anomalies are related to the presence of the percolation transition from isolated pores to the "infinite" pore cluster.

In order to compare the results of our model calculations to experiment, we have performed tensile tests on a series of samples made of an iron powder obtained by spraying in air (PZhRV2 grade). The samples were prepared by pressing to a preset porosity followed by sintering at 1500 K for 2.5 h in vacuum. The samples

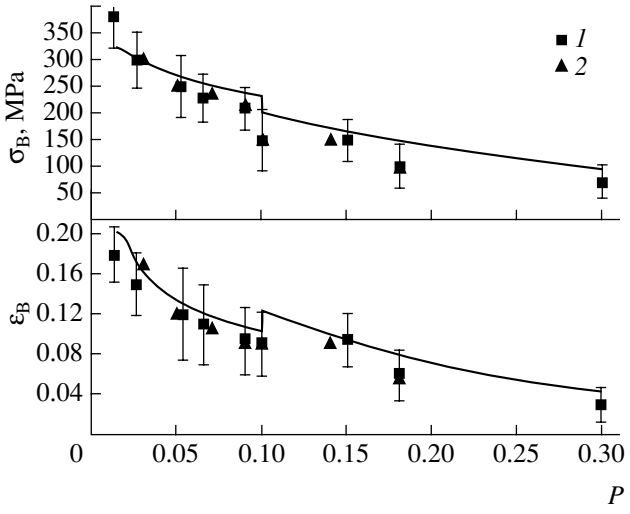

Fig. 2. Plots of the stress (σ_B) and strain (ε_B) at break versus porosity *P*. Curves show the results of numerical calculations using the proposed model; points show (*1*) the experimental results of this study and (*2*) the experimental data reproduced from [7].

had the standard shape for tensile tests with a rectangular working part of 3×3 mm cross section. The sample porosity varied within $P = 0$–0.3. The results of tensile tests were used to construct the σ–ε curves. The experimental data for particular samples are represented by points in Fig. 1. The points in Fig. 2 show the experimental data averaged over 10–12 samples with the same porosity. The observed scatter of the experimental results is related to the inhomogeneity of the porous structure of the samples studied. For comparison, Fig. 2 also presents some published experimental data [7].

As can be seen from the data in Figs. 1 and 2, the calculated curves are close to the corresponding experimental points. This is evidence of the reliability and adequacy of the proposed model, which allow it to be used for predictions of the behavior of porous materials on tensile straining. The experimental data confirm the presence of anomalies in the dependence of the ultimate mechanical characteristics of metals on the porosity of samples. Using the proposed model, it is possible to interpret the observed anomalies as being due to the percolation transition in the porous material studied.

REFERENCES

1. G. N. Dul'nev and V. V. Novikov, *Transfer Processes in Inhomogeneous Media* (Énergoatomizdat, Leningrad, 1991) [in Russian].
2. V. V. Polyakov, A. V. Egorov, and I. N. Svistun, Pis'ma Zh. Tekh. Fiz. **27** (22), 14 (2001) [Tech. Phys. Lett. **27**, 937 (2001)].
3. V. V. Polyakov and A. V. Golovin, Izv. Ross. Akad. Nauk, Met., No. 4, 81 (1995).
4. B. I. Shklovskiĭ and A. L. Éfros, Usp. Fiz. Nauk **117**, 401 (1975) [Sov. Phys. Usp. **18**, 845 (1975)].
5. A. E. Andreĭkin and N. V. Lysak, *The Method of Acoustic Emission in Fracture Studies* (Naukova Dumka, Kiev, 1989) [in Russian].
6. V. Z. Parton and E. M. Morozov, *Mechanics of Elastoplastic Fracture* (Nauka, Moscow, 1985).
7. O. I. Ban'kovskiĭ, V. F. Moiseev, E. P. Pechkovskiĭ, and N. I. Shcherban', Poroshk. Metall., No. 6, 94 (1988).

Translated by P. Pozdeev

Technical Physics Letters, Vol. 31, No. 2, 2005, pp. 143–146. Translated from Pis'ma v Zhurnal Tekhnicheskoĭ Fiziki, Vol. 31, No. 4, 2005, pp. 23–29.

Wave Theory of High-Speed Cutting Regimes in Turning of Materials

A. D. Gladun* and O. V. Vishenkova

Moscow Institute of Physics and Technology, Dolgoprudnyĭ, Moscow oblast, 141700 Russia

** e-mail: gladun@mail.mipt.ru*

Received April 12, 2004; in final form, August 3, 2004

Abstract—A theory of high-speed cutting regimes involved in turning of materials has been developed. According to this theory, the cut layer and the blade are considered as acoustic resonators coupled via a nonlinear contact stiffness and excited by the lowest antisymmetric Lamb mode. The turning process is described in terms of a parametric oscillatory system. Using the proposed theory, it is possible to determine optimum turning regimes. *© 2005 Pleiades Publishing, Inc.*

Modern metal-working industries widely employ the process of material turning in high-speed cutting regimes. The values of cutting speeds in these regimes vary for different materials, for example, within 300–1200 m/min for titanium, 300–1700 m/min for steel, and 2500–6500 m/min for aluminum. However, no physically clear notions of what is implied by a high cutting speed can be found in the literature: high as compared to what?

This Letter gives an outline of the new theory of cutting materials. According to the proposed approach, the cut layer and the blade are considered as acoustic resonators accumulating elastic energy during their contact interaction. The resonators are coupled via a nonlinear contact stiffness, which allows the turning process to be described in terms of a parametric oscillatory system. Within the framework of this theory, it is probably possible to provide a correct answer to the question of what is a measure of high cutting speed.

Consider the lowest antisymmetric Lamb mode (bending wave) in a plane-parallel plate with a thickness of $2h$, bounded by two free surfaces coinciding with the planes $x = \pm h$. We assume that the plate thickness satisfies the condition

$$\omega h \ll c_t,$$

where ω is the wave frequency and c_t is the shear wave velocity. The bending wave of small amplitude is described by the equation [1]

$$\rho\frac{\partial^2\xi}{\partial t^2} + \frac{h^2E}{3(1-\nu^2)}\Delta^2\xi = 0, \qquad (1)$$

where $\xi = \xi(y, z)$ is the displacement of a neutral surface, Δ is the two-dimensional Laplace operator, E is the Young modulus, and ν is the Poisson ratio of the plate material. Note that the shear wave velocity is related to the material parameters as

$$c_t = \sqrt{\frac{E}{2\rho(1+\nu)}}.$$

Let us find a solution to Eq. (1) in the following form:

$$\xi = \text{const}\exp\{i(\kappa z - \omega t)\}. \qquad (2)$$

Substituting expression (2) into Eq. (1), we obtain the dispersion relation

$$\omega = \kappa^2\sqrt{\frac{h^2E}{3\rho(1-\nu)}} = hc_t\kappa^2, \qquad (3)$$

where it is assumed that

$$\sqrt{\frac{2}{3(1-\nu)}} \approx 1.$$

The phase velocity v_{ph} of the bending mode can be expressed as

$$v_{\text{ph}} = \sqrt{2\pi c_t f h}, \qquad (4)$$

where $f = \omega/2\pi$. This mode has no critical frequency and exhibits dispersion. The group velocity of the wave is twice the phase velocity.

Let us consider the simplest process of turning with a straight cutting tool. High mechanical stresses (on the order of several gigapascals) and plastic strain developed in the cutting zone lead to the formation of acoustic waveguides, while finite dimensions of both the article (blank) and the tool lead to the formation of resonators. The characteristic drive frequency exciting the

1063-7850/05/3102-0143$26.00 © 2005 Pleiades Publishing, Inc.

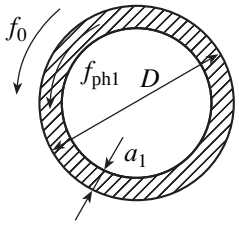

Fig. 1. Representing the cut layer in a cylindrical blank as an acoustic resonator (see the text for explanations).

bending wave in the material coincides with the lathe spindle frequency f_0. The cut layer has a thickness of

$$a_1 = s\sin\varphi,$$

a width of

$$b_1 = \frac{t}{\sin\varphi},$$

and a cross section area of $a_1b_1 = st$, where s is the blade feed per turn, t is the depth of cut, and φ is the cutting edge angle. The machining regimes are determined by the cutting speed v and the values of t and s. In the case under consideration (whereby spindle rotation is the main movement), the cutting speed is

$$v = \pi D f_0,$$

where D is the blank diameter.

Formula (4) is conveniently rewritten as

$$v_{ph1} = \sqrt{\pi c_{t1} f_1 a_1} = \pi D\sqrt{f_1\Omega_1}, \quad (5)$$

where

$$\Omega_1 = \frac{c_{t1}a_1}{\pi D^2}.$$

Here and below, subscripts 1 and 2 refer to the blank and the tool, respectively. The frequency Ω_1, which is characteristic of a given cutting regime, can be interpreted as the fundamental frequency of the resonator depicted in Fig. 1. Indeed, the wavelength λ_1 of the bending wave described by formula (5) is

$$\lambda_1 = \pi D\sqrt{\frac{\Omega_1}{f_1}}. \quad (6)$$

It is natural to assume that a stationary regime obeys the relation

$$m\lambda_1 \approx n\pi D, \quad (7)$$

where m and n are integers. Substituting formula (6) into relation (7), we obtain

$$f_1 = \frac{m^2}{n^2}\Omega_1, \quad (8)$$

which implies that $f_1 = \Omega_1$ for $m = n = 1$.

Let us introduce the angular phase velocity of the bending wave in the cut layer as

$$f_{ph1} = \frac{v_{ph1}}{\pi D}, \quad (9)$$

so that

$$f_{ph1} = \sqrt{f_1\Omega_1}. \quad (10)$$

It is also natural to assume that a stationary regime is characterized by synchronism with the drive frequency:

$$f_{ph1} = f_0. \quad (11)$$

Using expressions (8)–(11), we obtain

$$f_0 \approx \frac{m}{n}\Omega_1. \quad (12)$$

Relation (12) represents the condition of resonance in a nonlinear system [2]. Important particular cases are as follows:

(i) $m = n = 1$ (“main” resonance);

(ii) $m = 1$ (i.e., $\Omega_1 = nf_0$; resonance at the nth overtone of the drive frequency);

(iii) $n = 1$ (i.e., $f_0 = m\Omega_1$; resonance at the mth overtone of the intrinsic frequency, or a partial resonance, $\Omega_1 = f_0/m$).

Thus, real cutting regimes are characterized by the integers m and n. For high-speed regimes, we have

$$\Gamma \equiv \frac{f_0}{\Omega_1} \approx \frac{m}{n} > 1.$$

The corresponding wavelength is

$$\lambda_1 = \pi D\frac{n}{m},$$

so that the machined surface exhibits a fine structure in the feed direction.

The working layer of a blade (Fig. 2) also represents an acoustic resonator. Consider a replaceable blade having the shape of a parallelepiped (Fig. 3). Arrows in the cross section $ABCD$ indicate the direction of propa-

gation of a bending wave. The phase velocity of this wave is

$$v_{\text{ph}2} = \sqrt{2\pi c_{t2} a_2 f_2}, \quad (13)$$

where c_{t2} is the shear wave velocity in the blade, a_2 is the thickness of a working layer (in which the bending wave propagates), and f_2 is the wave frequency.

In a stationary regime, we naturally have

$$p\lambda_2 = qL, \quad (14)$$

where $\lambda_2 = \sqrt{\pi c_2 a_2 / f_2}$ is the wavelength, L is the perimeter of the *ABCD* section, and p and q are integers. This yields

$$f_2 = \frac{p^2}{q^2}\frac{\pi c_{t2} a_2}{L^2}.$$

Therefore, the fundamental frequency of this resonator is

$$\Omega_2 = \frac{\pi c_{t2} a_2}{L^2}. \quad (15)$$

The two acoustic resonators interact via a nonlinear contact stiffness, in which the spindle frequency f_0 and the induced bending wave frequency in the cut layer are mixed to yield a set of the combination frequencies $|kf_0 + lf_1|$, where k and l are positive or negative integers. The cutting edge, operating as the acoustic resonator, separates from this set an intrinsic frequency,

$$|k f_0 + l f_1| = \Omega_2,$$

such that

$$a_2 = \frac{L^2}{\pi c_{t2}}|k f_0 + l f_1|. \quad (16)$$

We may suggest that the main mechanism responsible for the appearance of roughness on the machined material surface is related to vibration of the cutting edge caused by the bending wave excited in the working layer. This implies that $a_2 \sim R_a$, where R_a is a parameter characterizing the material surface (e.g., arithmetic mean deviation of the surface profile).

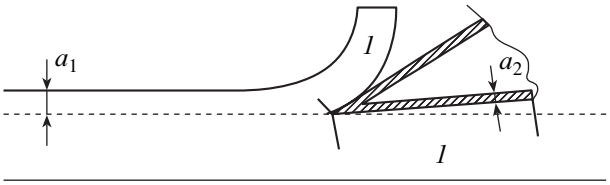

Fig. 2. Representing the working layer in a blade as an acoustic resonator (see the text for explanations).

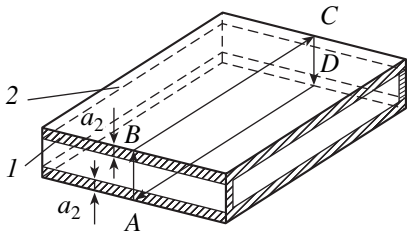

Fig. 3. Blade of a cutting tool: (*1*) main cutting edge; (*2*) secondary cutting edge (see the text for explanations).

The proposed theory was verified in special experiments, whereby a steel cylinder (grade 45 steel) with a diameter of $D = 70$ mm was turned at $t = 1$ mm in ten cutting regimes with a straight tool made of a hard alloy T15K6 with $E = 530$ GPa, $\rho = 11.3 \times 10^3$ kg/m^3, $n = 0.3$ ($c_{t2} = 4.25$ km/s), and $L = 26.5$ mm (Fig. 3). The results of these experiments are summarized in Table 1.

Table 1. Characteristics of the experimental regimes of turning a steel cylinder with a straight tool

No.	f_0, min^{-1}	s, mm	D, mm	c_{t1}, km/s	Ω_1, min^{-1}	$\Gamma = \frac{f_0}{\Omega_1}$	m	n	R_a, μm	R_z, μm	$R_{\max}$, μm
1	315	0.05	70	3	408	3/4	3	4	1.67	10.59	11.16
2	**400**	0.05	70	3	408	1	1	1	1.63	9.78	10.57
3	500	0.05	70	3	408	5/4	5	4	1.53	9.05	10.57
4	630	0.05	70	3	408	3/2	3	2	1.48	8.16	9.30
5	800	0.05	70	3	408	2/1	2	1	1.35	7.57	8.90
6	315	0.075	70	3	612	1/2	1	2	2.56	12.38	14.62
7	500	0.075	70	3	612	5/6	5	6	2.22	11.94	11.27
8	**630**	0.075	70	3	612	1	1	1	1.97	11.62	12.07
9	1000	0.075	70	3	612	5/3	5	3	1.89	10.03	12.27
10	1250	0.075	70	3	612	2/1	2	1	1.93	9.63	9.88

Note: f_0 values in bold refer to the main resonance.

Table 2. Theoretical estimates of the working layer thickness (a_2) in a cutting tool

No.	f_0, Hz	Ω_1, Hz	Γ	f_1, Hz	c_{t2}, km/s	L, mm	k	l	a_2, μm
1	5.25	6.8	3/4	3.82	4.25	26.5	3	3	1.43
2	6.67	6.8	1	6.8	4.25	26.5	2	2	1.42
3	8.33	6.8	5/4	10.62	4.25	26.5	2	1	1.44
4	10.5	6.8	3/2	15.3	4.25	26.5	1	1	1.35
5	13.33	6.8	2/1	27.2	4.25	26.5	0	1	1.43
6	5.25	10.2	1/2	2.55	4.25	26.5	6	6	2.46
7	8.33	10.2	5/6	7.08	4.25	26.5	3	3	2.43
8	10.5	10.2	1	10.2	4.25	26.5	2	2	2.17
9	16.66	10.27	5/3	28.3	4.25	26.5	1	1	2.36
10	20.83	10.2	2/1	40.8	4.25	26.5	0	1	2.15

The thickness a_2 of the working layer was estimated using formula (16) with

$$f_0 = \Gamma\Omega_1, \quad f_1 = \Gamma^2\Omega_1.$$

Calculations yield $L^2/\pi c_{t2} = 52.62 \times 10^{-9}$ (m s) and give the estimates of a_2 presented in Table 2. A comparison of data in Tables 1 and 2 shows that $a_2 \sim R_a$.

The Manly–Rowe relations for the parametric oscillations show that the system may exhibit autooscillatory regimes. The mechanism of excitation is analogous to that operating in a fiddle string driven by a bow: the rotating bank plays the role of an infinite bow. This circumstance may be of key importance for deeper insight into the physics of cutting processes and the mechanisms of fracture of the cutting blade.

REFERENCES

1. L. D. Landau and E. M. Lifshitz, *Course of Theoretical Physics*, Vol. 7: *Theory of Elasticity* (Nauka, Moscow, 1987; Pergamon, New York, 1986).
2. N. N. Bogolyubov and Yu. A. Mitropolskii, *Asymptotic Methods in the Theory of Nonlinear Oscillations* (Fizmatgiz, Moscow, 1958; Gordon and Breach, New York, 1962).
3. V. V. Migulin, V. I. Medvedev, E. R. Mustel', and V. N. Parygin, *Fundamentals of the Vibration Theory* (Nauka, Moscow, 1978) [in Russian].

Translated by P. Pozdeev

Technical Physics Letters, Vol. 31, No. 2, 2005, pp. 147–149. Translated from Pis'ma v Zhurnal Tekhnicheskoĭ Fiziki, Vol. 31, No. 4, 2005, pp. 30–36.

Plasma Opening Switch with a Ferroelectric Plasma Injector

A. E. Dubinov*, V. I. Kargin, A. S. Nemchinov, E. A. Ryaslov, S. A. Sadovoĭ, and V. D. Selemir

Institute of Experimental Physics, Russian Federal Nuclear Center, Sarov, Russia

**e-mail: dubinov@ntc.vniief.ru*

Received July 5, 2004

Abstract—A generator with a plasma opening switch employing a ferroelectric plasma injector has been designed, constructed, and studied in operation. The generator was tested in two regimes, being loaded on an electron-beam diode or vircator for the generation of bremsstrahlung (X-ray) or microwave radiation, respectively. © *2005 Pleiades Publishing, Inc.*

High-power nanosecond pulses of voltage or current are frequently obtained using generators based on inductive energy storage with plasma opening switches (POSs) [1]. Such devices usually contain extended electrodes forming a vacuum discharge gap. The electrodes are connected to a current source on one end and to a load (typically, a vacuum or plasma diode, etc.) on the other end. One or several plasma injectors are mounted on one of the electrodes between the current source and the load.

The generator with a POS operates as follows. Plasma injectors are initiated to produce plasma streams in the vacuum gap. Reaching the opposite electrode, the streams close the "current source–electrode with plasma injectors–plasma streams–opposite electrode" circuit, which serves the inductive energy store. At this instant, the current source is switched on to provide for the accumulation of magnetic energy in this store. When the accumulated energy is maximum, the resistance of the plasma is quickly increased by some means so that it becomes large compared to the load resistance. As a result, the accumulated energy is transferred to the load.

Plasma is usually injected into the gap by means of vacuum discharges along an insulator surface. For example, the plasma gun injectors described in [2] were made of pieces of a coaxial cable, in which carbon plasma was created as a result of the surface discharge between conductors along insulation at the cable end. The insulator was made of an organic polymer and was coated by a graphite suspension in alcohol prior to each pulse. The injector discharge was initiated by a 25-kV voltage pulse applied to the gun electrodes. Another plasma injector of the so-called flashboard type described in [3] comprised a thin dielectric film (Kapton, DuPont Corporation) bearing a conducting (copper) layer etched so as to form a pattern of thin electrodes. Application of a 23- to 30-kV voltage pulse led to the development of a surface discharge over the copper-free polymer surface, which served as a source of plasma in the POS.

Thus, the production of plasma in injectors of the types mentioned above requires additional sources of high-voltage pulses. The aim of this study was to develop a POS-based generator for plasma creation with reduced energy consumption.

One possible technical solution leading to a decrease in the energy required for plasma generation consists in selecting a special insulating material possessing maximum possible permittivity ε. As is known, ferroelectric materials may possess $\varepsilon > 1000$. Previously, we proposed a POS with ferroelectric plasma injectors [4]. A preliminary stage in the development of such POSs was devoted to determining the dependence of a threshold voltage U_{thr} (necessary for the surface discharge initiation in vacuum) on the permittivity ε of the insulating material. It was established that $U_{thr}(\varepsilon)$ is a monotonically decreasing function [5].

Figure 1 shows a schematic diagram of the proposed generator with POS. The main elements of the generator are (i) a pulsed inductive energy store voltage source of the BING-6 type, (ii) a coaxial system of extended electrodes forming the inductive store; (iii) a plasma injector with a ferroelectric insulator mounted on the outer electrode, and (iv) a pulsed injector voltage source of the BING-5 type. The inductive store unit was evacuated to a residual pressure of 10^{-5} Torr. The system was loaded either on a vacuum diode generating bremsstrahlung (X-ray) radiation or on a microwave generator of the vircator type. The inner and outer electrode diameters are 3 and 120 mm, respectively; the inductive store length is 150 mm. The BING-6 (BING-5) source unit had a flash capacitance of 6.6×10^{-9} F (4.5×10^{-9} F) and produced nanosecond voltage pulses with an amplitude of up to 75 kV (10 kV). Other parameters of pulsed voltage sources of the BING series (developed at the Institute of Experimental Phys-

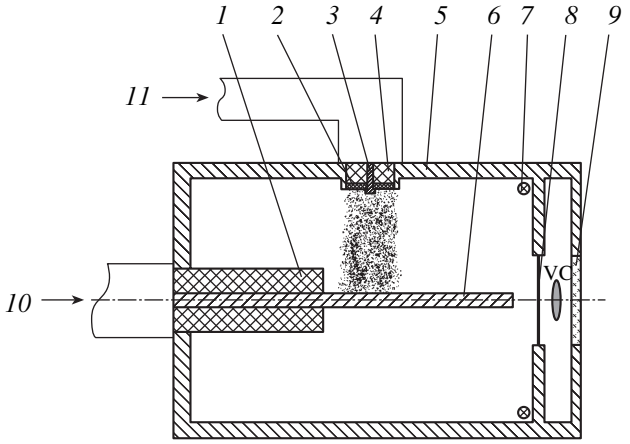

Fig. 1. Schematic diagram of a generator with POS loaded on a vircator: (*1*) inductive store insulator; (*2*) ferroelectric disk; (*3*) high-voltage electrode of plasma injector; (*4*) ceramic insulator of plasma injector; (*5*) outer electrode (anode) of the inductive store; (*6*) inner electrode (cathode) of the inductive store; (*7*) Rogowski loop; (*8*) anode grid (or foil); (*9*) microwave output window; (*10*) inductive store pulsed voltage source (BING-6); (*11*) plasma injector pulsed voltage source (BING-5); (VC) virtual cathode.

ics, Sarov) can be found in [6]. The sources were connected to electrodes by coaxial cables.

The coaxial plasma injector is made of a plasma-forming insulating material (a ferroelectric PZT ceramics of the TsTS-19 type) with $\varepsilon = 1300$, having the form of a disk with a diameter of 15 mm and a height of 2 mm. The central electrode of the injector is mounted in a 2-mm-diam hole at the disk center. A radial surface discharge was initiated on one of the disk faces between the coaxial electrodes spaced by a 5-mm-wide radial gap. The discharge plasma is injected into the interelectrode gap of the inductive store. At the moment of the inductive store shortening, the plasma stream has an electron density on the order of 10^{12} cm^{-3} (at a 10-kV voltage pulse), as measured by a probe technique described in [7]. It should be noted that the same voltage pulse applied to an injector of analogous geometry with a polyethylene insulator did not produce any surface discharge. The charging of the inductive energy store was performed with a certain delay relative to the moment of initiation of the plasma injectors. The optimum delay was found to be 0.75 μs.

Experiments with the generator described above were performed using the following measuring techniques. The inductive store current and the plasma injector discharge current were measured using shunts; the load current was measured with the aid of a Rogowski loop. The bremsstrahlung radiation pulses were measured using semiconductor detectors (SPPD-11-03), and the microwave pulse envelope was monitored by a 6D13D diode placed in a waveguide with a 72 × 34 mm cross section. The voltage drop across the load was measured using a voltage divider.

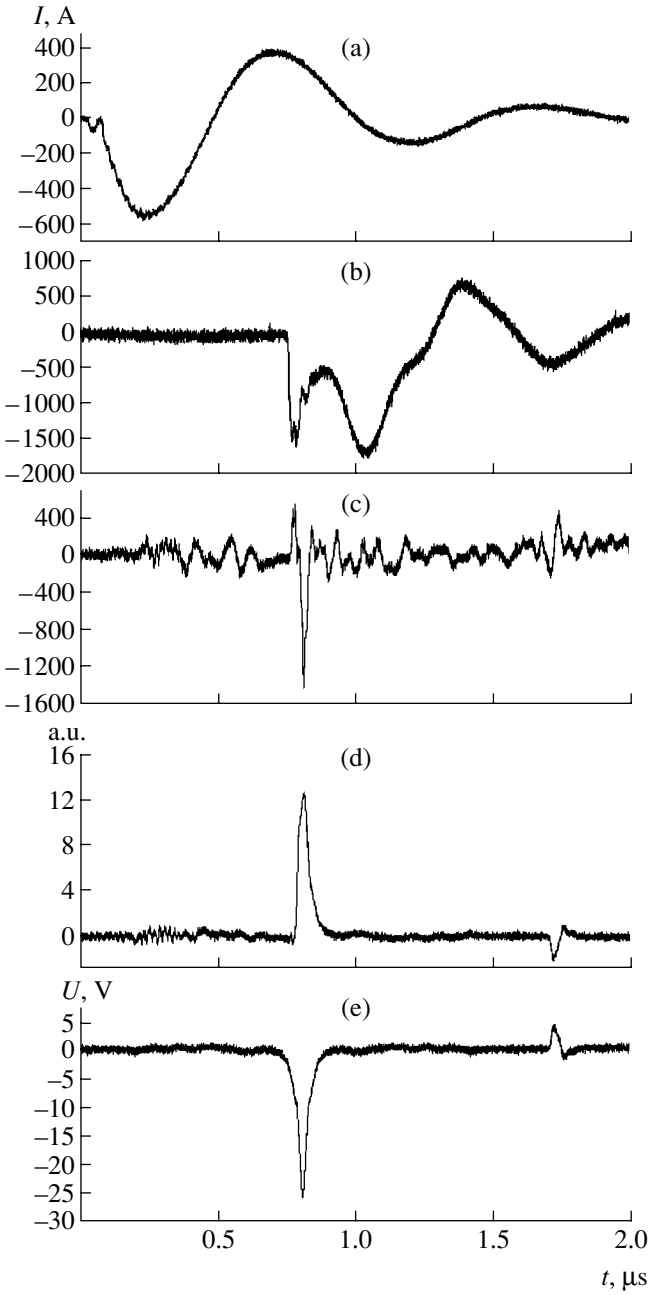

Fig. 2. Typical oscillograms of the main signals of a generator with POS: (a) plasma injector discharge current; (b) inductive store current; (c) load current; (d) X-ray pulse shape; (e) microwave radiation pulse envelope.

The results of monitoring of the output characteristics of the generator with POS are illustrated in Figs. 2a–2e, which show synchronized oscillograms of the main signals. Figure 2a presents the typical shape of the plasma injector discharge current. Figure 2b shows the waveform of the inductive storage current. As can be seen, the latter current is delayed by 0.75 μs relative to the injector pulse front. The outburst of the storage current is followed by a drop caused by a sharp increase in the plasma resistance. At this moment, the POS

switches the current into a load. Figure 2c shows the current profile in the load. At a pulse-forming line charging voltage of 75 kV, the maximum output pulse voltage was 160 kV.

In order to load the generator with POS on a vacuum electron beam diode operating in the bremsstrahlung generating regime, a 20-μm-thick tantalum foil target was mounted on the anode. The shape of the output X-ray pulse measured by a semiconductor detector for a 5-mm-long diode is presented in Fig. 2d. In order to obtain a microwave generator of the vircator type, the target was replaced by an anode grid made of a 0.15-mm-diam tantalum wire. The virtual cathode was formed in a 10-mm-long electron beam drift space between the grid and the dielectric window used for extraction of the microwave radiation (this configuration of the load is depicted in Fig. 1). The output microwave pulse had the envelope presented in Fig. 2e and a power estimated at a fraction of a megawatt.

In conclusion, we designed, constructed, and tested a generator with POS and a ferroelectric plasma injector that is capable of operating with various loads.

REFERENCES

1. R. A. Meger, R. J. Commisso, G. Cooperstein, and S. A. Goldstein, Appl. Phys. Lett. **42**, 943 (1983).
2. C. W. Mendel, Jr., D. M. Zagar, G. S. Millis, *et al.*, Rev. Sci. Instrum. **51**, 1641 (1980).
3. T. J. Renk, J. Appl. Phys. **65**, 2652 (1989).
4. A. E. Dubinov, N. N. Makarova, S. A. Sadovoĭ, *et al.*, RF Patent No. 2165684, Byull. Izobret., No. 11 (2001).
5. S. V. Bulychev, A. E. Dubinov, V. S. Zhdanov, *et al.*, in *Studies on the Physics of Gas Discharge: Collection of Scientific Works*, Ed. by V. D. Selemir and A. E. Dubinov (Institute of Experimental Physics, Sarov, 2003), p. 182 [in Russian].
6. B. G. Kudasov, S. S. Pavlov, V. A. Tananakin, *et al.*, in *Proceedings of the 11th International Pulsed Power Conference, Baltimore, 1997*, p. 1572.
7. A. E. Dubinov, I. L. L'vov, S. A. Sadovoĭ, and V. D. Selemir, in *Studies on the Physics of Gas Discharge: Collection of Scientific Works*, Ed. by V. D. Selemir and A. E. Dubinov (Institute of Experimental Physics, Sarov, 2003), p. 71 [in Russian].

Translated by P. Pozdeev

Technical Physics Letters, Vol. 31, No. 2, 2005, pp. 150–153. Translated from Pis'ma v Zhurnal Tekhnicheskoĭ Fiziki, Vol. 31, No. 4, 2005, pp. 37–43.

Radiation of a Charge Moving in a Waveguide with a Resonantly Dispersive Dielectric Layer

A. V. Tyukhtin

Institute of Radiophysics, St. Petersburg State University, St. Petersburg, Russia

e-mail: tyukhtin@niirf.spbu.ru

Received September 7, 2004

Abstract—The radiation of an ultrarelativistic point charged particle moving along the axis of a cylindrical waveguide containing a layer of resonantly dispersive dielectric medium is studied theoretically. It is shown that, in the case of a sufficiently thin waveguide, the dispersion leads to a significant contraction of the radiation, a decrease in the energy of harmonics, and an increase in the relative contribution due to the first mode as compared to the higher harmonics. These effects are less pronounced in waveguides with relatively large radii; still, they have to be taken into account, especially in determining the frequencies of harmonics. The role of the resonance dispersion is most significant in cases where the dielectric layer thickness is small compared to the waveguide radius. © *2005 Pleiades Publishing, Inc.*

The emission of Vavilov–Cherenkov radiation by charged particles moving in waveguide structures has been extensively studied (see, e.g., [1–8]). This direction of research is still of importance, particularly, in the context of development of particle accelerators employing the wake field technique [4–7]. It should be noted that one of the most significant factors in this phenomenon is related to the dispersion characteristics of a dielectric contained in the waveguide. A previous paper [8] was devoted to the radiation of a charged particle moving along the axis of a round waveguide completely filled with a dielectric medium exhibiting resonance dispersion. It was demonstrated that this dispersion significantly influences both the frequencies of excited harmonics and the radiation energy.

This Letter is concerned with the case when a dielectric medium fills only a part of the round cylindrical waveguide within a ring layer of thickness $d = a - b$, where a and b are the radii of the waveguide and the central vacuum channel, respectively. The magnetic permeability μ of the medium is assumed to be unity. The waveguide wall is assumed to be ideally conducting. Let us consider a point charge q moving at a constant velocity v along the z axis of a cylindrical coordinate system (r, φ, z).

General expressions for the potentials, fields, and particle energy losses in a system with this geometry are well known (see, e.g., review [1]). The consideration below is restricted to the ultrarelativistic case, which is of most interest from the standpoint of the wake-field acceleration of charged particles. In the limit as $v \longrightarrow c$, an expression for the radiative energy losses per unit pathlength of the charged particle can be written as follows:

$$W = \sum_m W_m = \frac{2q^2}{b^2} \times \sum_m \frac{\psi_1(s)}{f(s)\left[1 + \frac{\omega}{2(\varepsilon-1)}\frac{d\varepsilon}{d\omega}\right] - \frac{c\psi_0(s)}{b\sqrt{\varepsilon-1}}\frac{d\varepsilon}{d\omega}}\Bigg|_{\omega=\omega_m,\, s=s_m}, \quad (1)$$

where

$$s = \omega c^{-1}\sqrt{\varepsilon - 1}, \quad (2)$$

$$f(s) = \frac{\psi_1(s)}{2} + \frac{s}{2}\frac{d\psi_1(s)}{ds} - \frac{\varepsilon}{b}\frac{d\psi_0(s)}{ds} = \left(\frac{1}{2} - \varepsilon\right)\psi_1(s) + \left(\frac{\varepsilon}{sb} - \frac{sb}{2}\right)\psi_0(s) + \frac{sa}{2}[J_1(sa)N_0(sb) - J_0(sb)N_1(sa)] + \varepsilon\frac{a}{b}[J_1(sb)N_1(sa) - J_1(sa)N_1(sb)], \quad (3)$$

$$\psi_0(s) = J_1(sb)N_0(sa) - J_0(sa)N_1(sb),$$
$$\psi_1(s) = J_0(sb)N_0(sa) - J_0(sa)N_0(sb). \quad (4)$$

Here, $J_n(\xi)$ are the Bessel functions, $N_n(\xi)$ are the Neumann functions, $I_n(\xi)$ are the modified Bessel functions, and $K_n(\xi)$ are the modified Hankel functions. The eigenfrequencies ω_m in Eq. (1) are related via formula (2) to the eigenvalues s_m determined by the dispersion relation

$$sb\psi_1(s) - 2\varepsilon\psi_0(s) = 0. \quad (5)$$

1063-7850/05/3102-0150$26.00

Each term W_m in Eq. (1) represents the energy spent by the charge per unit pathlength to excite the mth harmonic (below, this value is referred to as the harmonic energy). This energy is equal (to within a factor) to the longitudinal component of the electric field at the point where the charge is situated ($W_m = -qE_z^{(m)}|_{z = vt,\, r = 0}$ [1]), while the amplitude of this field component on the waveguide axis behind the charge is twice as large: $E_{z\max}^{(m)} = 2W_m/|q|$. Once the harmonic energies are known, the field components at any point can be readily calculated using well-known relations [1].

It should be noted that the above formulas significantly simplify in the case where $s_m b \gg 1$. Assuming this condition to be valid and using asymptotic expressions for the cylindrical functions, dispersion relation (5) can be approximately rewritten as

$$\cot(sd) \approx sb/(2\varepsilon), \tag{6}$$

where $d = a - b$ is the dielectric layer thickness. In this case, Eqs. (1)–(4) yield

$$W_m \approx \frac{2q^2}{b^2}\left[1 + \frac{bds^2}{4\varepsilon} + \frac{d\varepsilon}{b} + \left(1 + \frac{bds^2}{4} + \frac{d\varepsilon^2}{b}\right)\frac{\omega}{2\varepsilon(\varepsilon - 1)}\frac{d\varepsilon}{d\omega}\right]^{-1}\Bigg|_{\omega = \omega_m,\, s = s_m}. \tag{7}$$

Let us consider the case of a medium with the permittivity

$$\varepsilon = 1 + \frac{\omega_L^2}{\omega_r^2 - \omega^2} = \frac{\omega_r^2\varepsilon_0 - \omega^2}{\omega_r^2 - \omega^2}, \tag{8}$$

where ω_r and ω_L are the resonance and Langmuir frequencies, respectively, and $\varepsilon_0 = 1 + \omega_L^2/\omega_r^2$ is the permittivity at a low (as compared to ω_r) frequency. The radiation of a charge moving in the infinite medium with such resonance dispersion was studied by Afanasiev *et al.* [9, 10], and the case of a waveguide completely filled with this medium was analyzed in [8].

In the case under consideration, the radiation frequency and the permittivity of the medium can be expressed as functions of the variable s,

$$\omega = \frac{\omega_r s}{\sqrt{s^2 + \omega_r^2 c^{-2}(\varepsilon_0 - 1)}}, \qquad \varepsilon = \frac{\omega_r s}{\sqrt{s^2 + c^{-2}\omega_r^2(\varepsilon_0 - 1)}}, \tag{9}$$

and the exact dispersion relation (5) can be rewritten as

$$sb\psi_1(s) - 2\frac{c^2 s^2 + \omega_r^2\varepsilon_0}{\omega_r^2}\psi_0(s) = 0. \tag{10}$$

The energy of the mth harmonic according to formula (1) is

$$W_m = \frac{2q^2}{b^2}\frac{\omega_r^2 - \omega_m^2}{\omega_r^2}\psi_1(s_m) \times\left[f(s_m) - \frac{2c\omega_m\sqrt{\varepsilon_0 - 1}}{b\omega_r\sqrt{\omega_r^2 - \omega_m^2}}\psi_0(s_m)\right]^{-1}. \tag{11}$$

Let us obtain approximate formulas for the condition $s_m b \gg 1$, which can be conveniently represented as

$$\frac{b\omega_r}{c}\frac{\omega_m\sqrt{\varepsilon_0 - 1}}{\sqrt{\omega_r^2 - \omega_m^2}} \gg 1. \tag{12}$$

Then, dispersion relation (6) acquires the form

$$\cot(\chi) \approx \frac{b}{2d}\chi\frac{\tilde{d}^2}{\varepsilon_0\tilde{d}^2 + \chi^2}, \tag{13}$$

where $\chi = sd$ and $\tilde{d} = d\omega_r c^{-1}$ is the dimensionless layer thickness. This relation shows that the root χ_m of the dispersion equation falls in the interval $m\pi < \chi_m < (m + 1/2)\pi$ (where $m = 0, 1, 2, \ldots$). Under condition (12), the mth harmonic energy is

$$W_m \approx \frac{2q^2}{b^2}\left[1 + \frac{b\chi_m^2}{4d\varepsilon_m} + \frac{d\varepsilon_m}{b} + \left(1 + \frac{b\chi_m^2}{4d} + \frac{d\varepsilon_m^2}{b}\right)\frac{\chi_m^2}{(\varepsilon_0 - 1)(\chi_m^2 + \tilde{d}^2\varepsilon_0)}\right]^{-1}, \tag{14}$$

where $\varepsilon_m = \varepsilon(\omega_m)$.

Now, the above results will be illustrated by several examples, whereby the waveguide with a resonantly dispersive medium is compared to the case of a nondispersive dielectric medium with $\varepsilon = \varepsilon_0$. Figures 1 and 2 show the frequencies and energies of harmonics calculated using exact formulas as functions of the d/a ratio for a relatively thin and relatively thick waveguide, respectively, with (a, b) a dispersive and (c, d) a nondispersive dielectric layer.

As can be seen, the frequencies of harmonics are monotonically decreasing functions of the relative thickness of the dielectric layer. For a relatively thin waveguide (Fig. 1), the frequencies are much lower in the presence of resonance dispersion than in the case of a nondispersive medium. Note also that the dispersion produces strong contraction of the radiation spectrum. For a waveguide completely filled ($d = a$) with the resonantly dispersive medium, the harmonic frequencies fall within the interval from $0.82\omega_r$ to ω_r; for $d < 0.3a$,

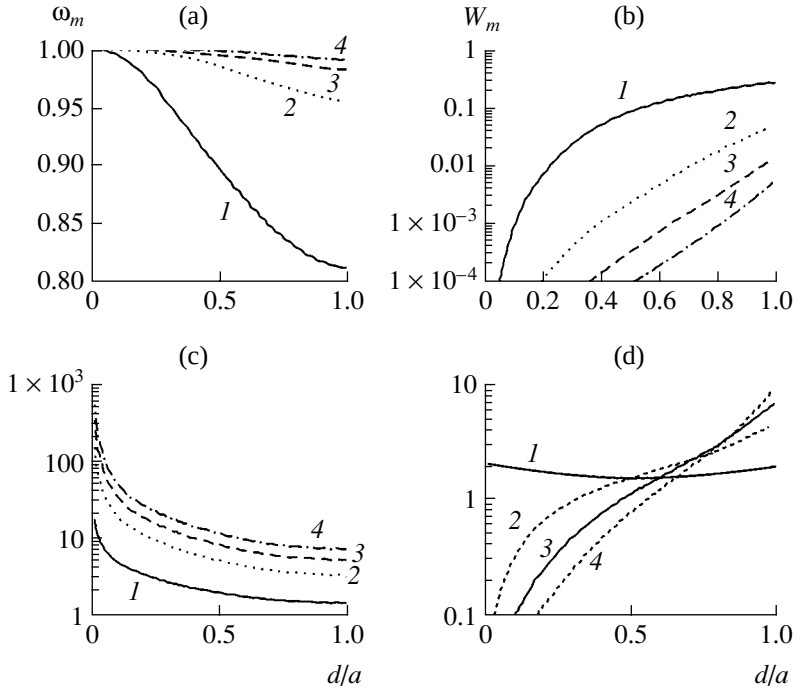

Fig. 1. Plots of the harmonic (a, c) frequencies and (b, d) energies versus relative thickness of the dielectric layer (a, b) with and (c, d) without resonance dispersion (ε = 4) in a relatively thin waveguide ($\tilde{a} \equiv a\omega_r/c = 1$). Figures at the curves indicate the mode numbers; the mode frequencies ω_m are expressed in units of ω_r, and the mode energies W_m, in units of $q^2\omega_r^2 c^{-2}$.

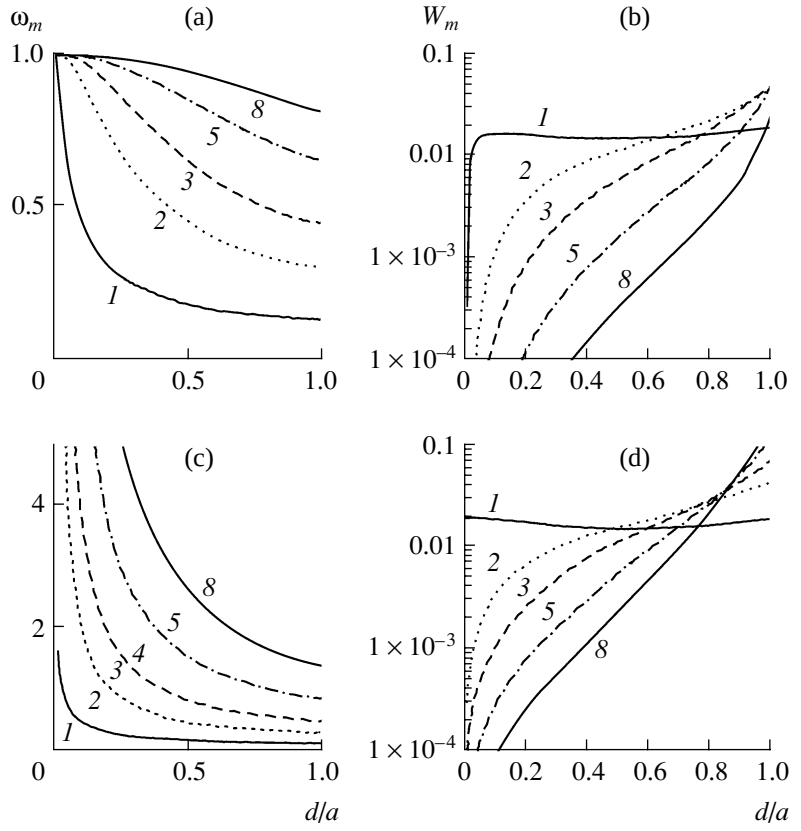

Fig. 2. Same as in Fig. 1, for a relatively thick waveguide ($\tilde{a} \equiv a\omega_r/c = 10$).

the width of this interval is less than 5% of the resonance frequency. As can be seen from a comparison of Figs. 1b and 1d, the energy of each harmonic in the presence of a dispersive medium is also much lower than that in the case of a dielectric medium without dispersion. Moreover, the energy of the first harmonic in the waveguide with a resonantly dispersive medium is always significantly higher than the energies of all higher harmonics, so that the generated field is virtually single-mode for any thickness of the dispersive dielectric layer. In the absence of dispersion, the first mode predominates only in the case of thin dielectric layers, while the system with $d \geq 0.5a$ still features a multimode field with an insignificant role played by the first harmonic.

In the case of a relatively thick waveguide (Fig. 2), the pattern significantly changes. The difference between mode frequencies in the waveguides with and without resonance dispersion is somewhat less pronounced, albeit still significant. The effect of suppression of the energy of the first harmonic in the system with dispersion is almost not manifested (except for the case of a very thin dielectric layer). The difference between energies of the higher harmonics is more pronounced. For a sufficiently thin dielectric layer, the first mode predominates in both cases; if the layer thickness is comparable to the waveguide radius, the wave field has a multimode character.

It should be emphasized that, as can be seen from Figs. 1 and 2, the difference between frequencies and energies of modes in the systems with and without dispersion increases with decreasing thickness of the dielectric layer. Thus, making allowance for the resonance dispersion is most important in cases when the dielectric layer thickness is small compared to the waveguide radius.

Acknowledgments. The author is grateful to A.D. Kanareikin for fruitful discussions.

REFERENCES

1. B. M. Bolotovskiĭ, Usp. Fiz. Nauk **75**, 295 (1961) [Sov. Phys. Usp. **4**, 781 (1961)].
2. V. P. Zrelov, *Cherenkov Radiation and Its Applications in High-Energy Physics* (Atomizdat, Moscow, 1968), Part 1 [in Russian].
3. V. I. Tsytovich, Izv. Vyssh. Uchebn. Zaved. Radiofiz. **290**, 597 (1986).
4. W. Gai, P. Schoessow, B. Cole, *et al.*, Phys. Rev. Lett. **61**, 2756 (1988).
5. J. G. Power, M. E. Conde, W. Gai, *et al.*, Phys. Rev. ST Accel. Beams **3**, 101302 (2000).
6. A. S. Vardanyan and G. G. Oksuzyan, Zh. Tekh. Fiz. **72** (4), 76 (2002) [Tech. Phys. **47**, 448 (2002)].
7. L. Schachter, Phys. Rev. E **62**, 1252 (2000).
8. A. V. Tyukhtin, Pis'ma Zh. Tekh. Fiz. **30** (14), 68 (2004) [Tech. Phys. Lett. **30**, 605 (2004)].
9. G. N. Afanasiev and V. G. Kartavenko, J. Phys. D **31**, 2760 (1998).
10. G. N. Afanasiev, V. G. Kartavenko, and E. N. Magar, Physica B **269**, 95 (1999).

Translated by P. Pozdeev

Technical Physics Letters, Vol. 31, No. 2, 2005, pp. 154–156. Translated from Pis'ma v Zhurnal Tekhnicheskoĭ Fiziki, Vol. 31, No. 4, 2005, pp. 44–48.

Classification of the Interactions of Relativistic Electrons with Laser Radiation

A. Kh. Khokonov and M. Kh. Khokonov

Kabardino-Balkarian State University, Nalchik, Kabardino-Balkaria, Russia

e-mail: khokon6@mail.ru

Received August 4, 2004

Abstract—The interactions of relativistic electrons with laser radiation are classified in terms of three Lorentz-invariant quantities, which can be determined using the laser radiation parameters and the electron energy. The proposed classification covers the entire range of electron energies and laser radiation intensities presently in use, with allowance for quantum effects and nonlinear processes of higher harmonic generation. © *2005 Pleiades Publishing, Inc.*

New sources of beams of X-ray and gamma quanta based on the interaction of laser radiation with relativistic electrons (referred to below as laser radiation sources, LRSs) offer several advantages over traditional sources employing the interaction of electrons with a substance [1]. These are (i) a high monochromaticity without a bremsstrahlung background, (ii) high directivity related to the absence of multiple scattering effects, (iii) the possibility of obtaining circularly polarized photons, and (iv) the possibility of generating short (femtosecond) X-ray and gamma-radiation pulses [2, 3].

Until recently, the main disadvantage of LRSs was a relatively low intensity of the obtained radiation beams. However, the situation has been changed by the development of lasers with an output pulse power on the order of several terawatts. The electric field component in such laser radiation is on the same order of magnitude as that of the continuous electrostatic potential field in oriented crystals [4]. Depending on the laser radiation parameters and electron energies, the form of the LRS spectrum may significantly vary: from a dipole spectrum with a single peak (terminating at a certain maximum frequency) to a continuous synchrotron radiation spectrum covering all frequencies up to $\hbar\omega \sim E$, where $E = m_0\gamma c^2$ is the electron energy, γ is the Lorentz factor, and m_0 is the electron rest mass. The electron energies accessible with modern experimental setups vary from dozens of megawatts [2, 3] up to ~10^2 GeV [5]. Therefore, it is important to develop a classification of the interactions of relativistic electrons with laser beams, which would allow the character of these interactions and the type of the corresponding LRS spectrum to be readily determined.

The intensity of the electromagnetic field of a laser beam is characterized by a Lorentz-invariant parameter (see, e.g., reviews [6])

$$v_0^2 = \frac{e^2}{m_0^2c^2}A^2 = \frac{e^2\mathscr{E}_0^2}{m_0^2c^2\omega_0^2}, \quad (1)$$

where $A = (0, \mathbf{A})$ is the 4-potential of the laser field and $\mathscr{E}_0$ is the amplitude of the electric field strength of laser radiation with a frequency of ω_0. The field is referred to as strong if $v_0 \geq 1$.

Parameter (1) can be also given an alternative meaning, according to which it characterizes how strongly the field deflects a moving electron: $v_0 \approx \theta_e\gamma$ [4], where θ_e is the angle of electron deflection in an external field with the given strength. If this angle is smaller than the characteristic value $\theta_\gamma \sim 1/\gamma$ (i.e., if $\theta_e\gamma \ll 1$), then we have $v_0 \ll 1$ (this case corresponds to the dipole approximation). In this case, the LRS spectrum consists of a single harmonic with the maximum frequency $\omega_m = 2\gamma^2\Omega_0$ (for $\hbar\omega \ll E$), where Ω_0 is the frequency of transverse oscillations of the moving electron. For example, the interaction between electron and laser beams propagating in opposite directions yields $\Omega_0 = 2\omega_0$ [4].

On the contrary, for $v_0 \geq 1$, the spectrum of radiation emitted by an electron consists of many peaks with the frequencies obeying the relation [1]

$$u_k = ak/(1 + v_0^2 + ak), \quad (2)$$

where $u_k = \hbar\omega/E$ and k is the harmonic number. Here, the Lorentz-invariant parameter is

$$a = \frac{2\hbar}{m_0^2c^2}kp = \frac{2\hbar\Omega_0\gamma}{m_0c^2}, \quad (3)$$

where k and p are the 4-momenta of the laser photon

and of the electron, respectively, and a is a parameter depending on the electron energy and determining the role of quantum effects.

If the laser field is weak, so that $\nu_0 \ll 1$ (more precisely, $\nu_0 < 0.1$) and, simultaneously, $a > 0.1$, we obtain the so-called quantum dipole approximation (or the inverse Compton effect). In this case, the RLS spectrum has a single harmonic ($k = 1$) and is described by a single parameter a [1, Eq. (9)]. Under the conditions such that $\nu_0 < 1$ and $a < 0.1$, the dipole formulas of classical electrodynamics [2, 3] are valid and we deal with the Thomson backscattering.

When the laser field intensity is high ($\nu_0 \geq 1$), the LRS spectrum exhibits a synchrotron character over a large range of a and ν_0. For the applicability of this synchrotron approximation, it is necessary that the term ν_0^2 in the denominator of Eq. (2) would dominate over ak (a sufficient condition is that $\nu_0^2 > a$).

For the applicability of classical electrodynamics in the synchrotron approximation ($\nu_0 \geq 1$), it is already insufficient that $a \ll 1$, because the spectrum contains a large number of harmonics. The role of quantum effects in the case of a synchrotron character of the LRS spectrum (constant field approximation) is determined by the invariant Schwinger parameter

$$\chi = \frac{e\hbar\left|F_{\mu\nu}p^{\nu}\right|}{m_0^2c^3} \approx \frac{2e\mathscr{E}_0\hbar\gamma}{m_0^2c^3}. \qquad (4)$$

The right-hand side of relations (3) and (4) refers to the case of the interaction between electron and laser beams propagating in opposite directions. In the constant field approximation, the classical electrodynamics is valid provided that $\chi < 0.1$ (see, e.g., [7]). The parameter χ can be expressed (to within a factor on the order of unity) as $\chi \approx a\nu_0$.

The above classification can be conveniently illustrated using a diagram in the a versus ν_0 plane on the logarithmic scale. A diagram presented in the figure classifies the interactions of laser radiation with relativistic electrons in terms of $\ln\nu_0$ (abscissa) and $\ln a$ (ordinate), so that the coordinate axes correspond to the ν_0 and a values of unity. In this coordinate system, the region of strong fields is to the right of the ordinate axis, while the region where quantum effects are manifested in the LRS spectrum occurs in the vicinity of the abscissa axis and above this axis.

The region to the left of the dashed line *MN* in the figure represents weak laser fields: $\nu_0 < 0.1$ ($\ln 0.1 = -2.3$). The classical case takes place for $a < 1$. Accordingly, the *AKN* region corresponds to the classical dipole approximation (Thomson backscattering). The quantum dipole spectrum (or the inverse Compton effect) takes place in the *AKM* region. In the last two regions, the LRS spectrum is characterized by high monochromaticity ($\Delta\omega/\omega \sim 0.25$) and displays a single peak terminating at the frequency given by formula (2) for $k = 1$. The number of photons radiated per unit time in the classical case is approximately $n \sim \alpha\nu_0^2\Omega_0$, where $\alpha = 1/137$ [4]. In the presence of quantum effects, this number decreases as compared to the classical value. For example, the classical formula overstates n by a factor of 2 in the case of $a = 1$ and by a factor of 4, in the case of $a = 7$ (see, e.g., [8, Fig. 2]).

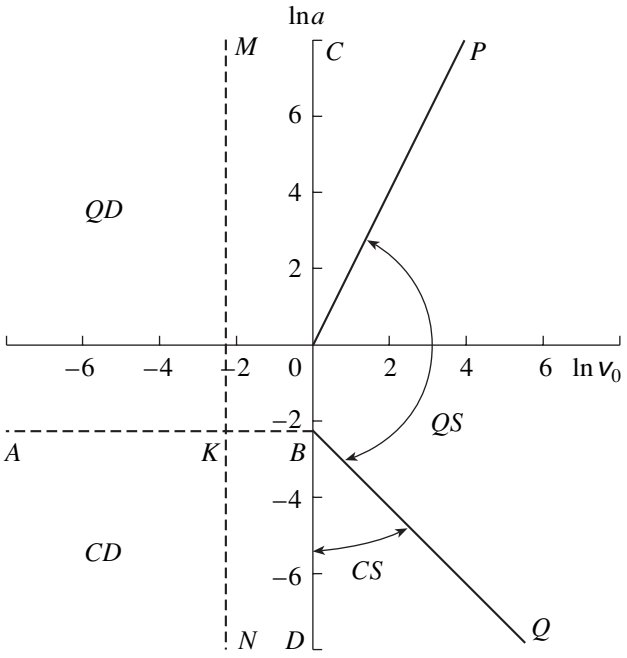

Schematic diagram illustrating the classification of interactions of relativistic electrons with laser radiation: (region *AKM*) quantum dipole (QD) spectrum; (region *AKN*) classical dipole (CD) spectrum (see [1, Eq. (9)]); (sector *QS*) quantum synchrotron approximation (see [1, Eq. (11)]); (sector *CS*) classical synchrotron approximation (see [9, Eq. (20)]); (region *MKBOP*) exact quantum-mechanical calculation taking into account the generation of higher harmonics (see [1, Eq. (7)]); (region *NKBD*) classical electrodynamics with allowance for the generation of higher harmonics [9, 10].

The condition of the quantum synchrotron approximation ($\nu_0^2 > a$ and $\nu_0 > 1$) appears as $2\ln\nu_0 > \ln a$, and the corresponding region extends to the right of the *OP* line in the figure. The LRS spectrum is determined by the quantum synchrotron formula and has a shape determined by a single parameter χ [1].

Taking into account that $\chi \approx a\nu_0$, the region of the classical synchrotron approximation ($\chi < 0.1$; $\nu_0 \geq 1$) is determined by the inequality $\ln a + \ln\nu_0 < -2.3$ and corresponds to the *CS* sector. In this case, the LRS spectrum appears as the classical synchrotron spectrum (see [9, Eq. (20)]). By the same token, the *QS* sector corresponds to the quantum synchrotron spectrum (see [1, Eq. (11)]).

The other regions in the figure require exact calculations taking into account the generation of higher harmonics. The formulas of classical electrodynamics [9, 10] are valid in the *NKBD* region, whereas the exact quantum-mechanical expressions (see [1, Eq. (7)]) have to be used in the *MKBOP* region.

The proposed classification of the interactions of relativistic electrons with laser radiation, as considered above and illustrated in the figure, has a general character depending neither on the mutual orientation of the laser and electron beams nor on the polarization of the electron beam. Thus, once the electron energy and laser radiation parameters are known, it is possible to calculate invariants by formulas (1), (3), and (4) and use the diagram to determine the character of the LRS spectrum and the type of the model to be used in calculations.

REFERENCES

1. A. Kh. Khokonov, M. Kh. Khokonov, and A. A. Kizdermishov, Zh. Tekh. Fiz. **72** (11), 69 (2002) [Tech. Phys. **47**, 1413 (2002)].
2. P. Eisenberger and S. Suckewer, Science **274**, 201 (1996).
3. R. W. Schoenlein, W. P. Leemans, A. H. Chin, *et al.*, Science **274**, 236 (1996).
4. M. Kh. Khokonov and R. A. Carrigan, Nucl. Instrum. Methods Phys. Res. B **145**, 133 (1998).
5. C. Bula, K. T. McDonald, E. J. Prebys, *et al.*, Phys. Rev. Lett. **76**, 3116 (1996).
6. V. I. Ritus, Tr. FIAN **111**, 5 (1979); **168**, 141 (1986).
7. J. Lindhard, Phys. Rev. A **43**, 6032 (1991).
8. A. Kh. Khokonov, M. Kh. Khokonov, and R. M. Keshev, Pis'ma Zh. Tekh. Fiz. **24** (20), 20 (1998) [Tech. Phys. Lett. **24**, 797 (1998)].
9. A. Kh. Khokonov, M. Kh. Khokonov, and R. M. Keshev, Nucl. Instrum. Methods Phys. Res. B **145**, 54 (1998).
10. Y. I. Salamin and F. H. M. Faisal, Phys. Rev. A **54**, 4383 (1996).

Translated by P. Pozdeev

Technical Physics Letters, Vol. 31, No. 2, 2005, pp. 157–158. Translated from Pis'ma v Zhurnal Tekhnicheskoĭ Fiziki, Vol. 31, No. 4, 2005, pp. 49–53.

A Moire Interference Technique for Studying Vortex Flame Structures

V. P. Samsonov* and I. V. Samsonova

Surgut State University, Surgut, Russia

** e-mail: svp@iff.surgu.ru*

Received September 20, 2004

Abstract—A new moire imaging technique is proposed that expands the possibilities of interference methods for studying vortex flame structures. Moire analogs of the interference patterns of a flame are obtained, which correspond to the interferometer adjustment to the fringes of finite and infinite widths. It is found that the moire analogs are identical to the original interference patterns. The main advantages of the proposed moire technique are the low cost of the experiment and the possibility of readjusting a current interference pattern for the same nonstationary optical inhomogeneity. © *2005 Pleiades Publishing, Inc.*

The main difficulties encountered in the application of interference methods to experimental investigations of the structure of nonstationary and inhomogeneous flows are related to a tedious adjustment of the interferometer and the need for readjusting it for solving various tasks in the course of one experiment. It was pointed out [1] that an interference pattern of a nonstationary optical inhomogeneity obtained at a current moment of time allows the refractive index profiles to be correctly calculated only in the absence of extrema. Vortex structures formed in a flow lead to the formation of complicated velocity, temperature, and pressure fields, which influence the refractive index distribution in the given medium.

The phase difference between interfering light waves is an integral characteristic defined as

$$\Delta\varphi = [2\pi \int_0^l (n_0 - n)dx]/\lambda,$$

where λ is the light wavelength; n_0 and n are the refractive indices of the medium in the thermal inhomogeneity and in the surrounding medium, respectively; and l is the geometric pathlength of a light ray. For an interference pattern of a vortex flow, precise determination of the direction of a local change in the phase difference $\Delta\varphi$ at a point where the interference lines form local spots or "saddles" is possible only provided that the interferometer can be instantaneously readjusted from finite to infinite fringes [2]. Unfortunately, this is impossible in a single experiment using traditional interference methods.

The above problem can be solved using a moire technique. Application of such techniques to the rearrangement of interference patterns essentially repeats the method of double exposure used for the formation of holograms. The idea of the proposed approach consists in obtaining two interference patterns (reference and object) for the same interferometer adjustment to the fringes of finite width. One of these patterns, obtained in the absence of a given optical inhomogeneity, is then superimposed onto the pattern of this very inhomogeneity. Then, one pattern is shifted relative to another and the resulting pattern is examined in the transmission mode. In this way, it is possible to rearrange the positions of interference fringes so as to obtain the necessary information concerning the direction of the phase shift of the interfering light waves at a given point of the optical inhomogeneity.

Figure 1 shows examples of the (*1*) reference and (*2*) object interference patterns. The latter pattern was obtained by placing a candle flame in the working field of a polarization shift interferometer based on a shadow device of the IAB-451 type. The interferometer was arbitrarily tuned without any special requirements concerning high-precision adjustment, working table

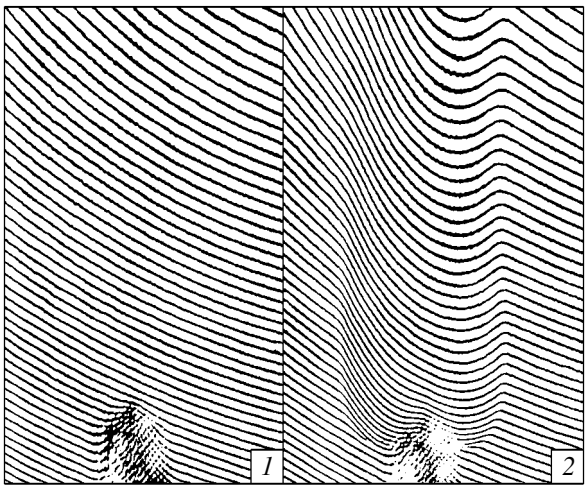

Fig. 1. Moire interference patterns of a candle flame: (*1*) reference; (*2*) object.

1063-7850/05/3102-0157$26.00 © 2005 Pleiades Publishing, Inc.

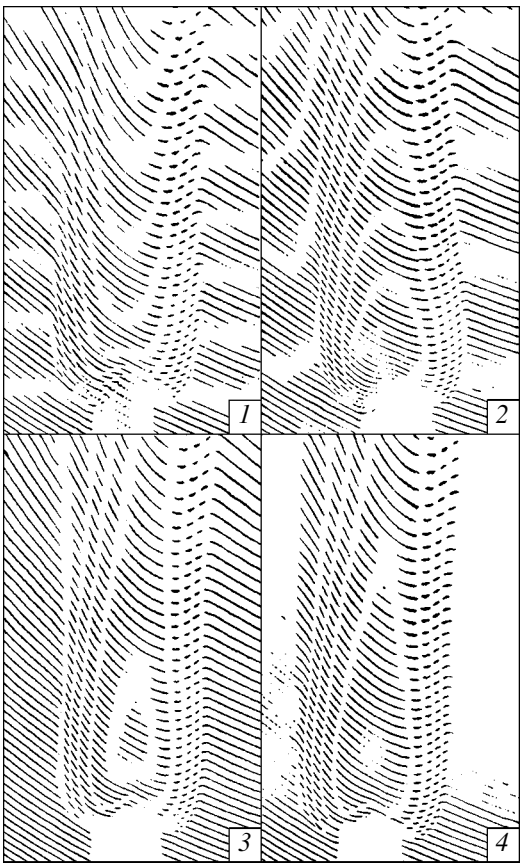

Fig. 2. Moire interference patterns of the same flame as in Fig. 1, corresponding to the interferometer adjustment to the (*1*, *3*) dark and (*2*, *4*) bright fringes of (*1*, *2*) finite and (*3*, *4*) infinite width.

shock absorber, etc. In Fig. 1, careless tuning of the interferometer is manifested in that the interference fringes have different widths, arbitrary orientation, and significant curvature. The only requirement concerning the instrument adjustment was that the number of interference fringes be sufficiently large. In this case, the resulting moire interference pattern is sufficiently detailed and the absolute error of determination of the geometric path difference between light rays is equal to the width of interference fringes in the reference pattern.

Figure 2 gives examples of the moire interference patterns of the same flame, which were obtained by superimposing patterns *1* and *2* presented in Fig. 1. The first pattern in Fig. 2 corresponds to the interferometer adjustment to fringes of finite width. As can be seen, the interference fringes exhibit downward deviation in the flame region. The direction of deviation shows that the phase difference between light waves is a continuous function with a single maximum at the flame center. The second pattern in Fig. 2 corresponds to the interferometer readjustment at which the fringes deviate upward. Patterns *3* and *4* illustrate the interferometer adjustment to the dark and bright fringes of infinite width. A comparison of these moire interference patterns to those obtained after the corresponding readjustment of the interferometer show their complete identity.

A disadvantage of the moire interference patterns is the discrete (mosaic) character and the related additional error in the determination of the phase difference between light waves at a given point of optical inhomogeneity. When the interferometer is adjusted for the fringes of finite width, the phase difference is calculated as $\Delta\varphi = 2\pi\Delta x/x_0$, where Δx and x_0 are the fringe width and its shift relative to the initial position at the given point of optical inhomogeneity. Calculating the maximum phase shift of light waves at the flame center for patterns *1* and *2* in Fig. 2, we obtain $\Delta\varphi = 9\pi$. The same result is obtained from patterns *3* and *4*. The maximum phase difference is estimated using the relation $\Delta\varphi = \pi n$, which is valid for the interferometer adjustment to the fringes of infinite width (n is the order of interference at the given point). Evidently, the additional relative error in the calculation of $\Delta\varphi$ is on the order of a sum of the relative errors involved in the determination of Δx and x_0. Patterns *1* and *2* in Fig. 1 show that this error does not exceed the distance between the interference fringes on the reference or object patterns and amounts approximately to 7–8%. It should be emphasized that Fig 1 is presented here for illustration purposes only. If necessary, the additional relative error introduced by the moire interference pattern can be reduced to a level below 0.1%.

REFERENCES

1. W. Hauf and U. Grigull, *Advances in Heat Transfer*, Vol. 6: *Optical Methods in Heat Transfer* (Academic, London, 1970).
2. S. A. Abrukov, *Shadow and Interference Methods for Studying Optical Inhomogeneities* (Kazan State University, Kazan, 1962) [in Russian].

Translated by P. Pozdeev

Technical Physics Letters, Vol. 31, No. 2, 2005, pp. 159–160. Translated from Pis'ma v Zhurnal Tekhnicheskoĭ Fiziki, Vol. 31, No. 4, 2005, pp. 54–57.

The Effective Density and Transport Properties of Compacted Carbon Nanotubes and Nanowhiskers

I. V. Zolotukhin*, I. M. Golev, A. E. Markova, S. N. Blinov, D. A. Grishin, and É. G. Rakov

Voronezh State Technical University, Voronezh, 394026 Russia
Mendeleev University of Chemical Technology, Moscow, 125190 Russia
** e-mail: paul@zolot.vrn.ru*
Received September 20, 2004

Abstract—We have studied the effective density, electric conductivity, and thermo emf of compacted carbon nanotubes (NTs) and nanowhiskers (NWs). The effective densities of NTs and NWs are 1.6 and 2.8 g/cm^3 respectively. The thermo emf of compacted NWs (33 μV/K) and NTs (7–8 μV/K) make it possible to use these materials in sensors of molecular gases and biological objects. It is also recommended to introduce NWs and NTs as fillers into glue compositions possessing increased strength and electric conductivity, which are necessary for gluing metals. © *2005 Pleiades Publishing, Inc.*

Carbon nanotubes (NTs) and nanowhiskers of nanowires (NWs) possess a number of interesting properties and attract considerable practical interest in various fields of technology [1–3]. Methods for the large-scale production of NTs and NWs have been developed (see, e.g., [4, 5]), which makes possible the characterization of these materials in macroscopic amounts. There were attempts to create ordered layer structures using the surface tension of a liquid forming a colloid solution of NTs [6]. In this context, it is important to study the density of NTs and NWs, since the density of these components have to be somewhat greater than that of the liquid medium.

We have studied carbon NWs obtained as described in [5] and NTs synthesized using the method proposed in [7]. The obtained NTs had between one and four shells and formed bundles with a diameter within 8–30 nm and a length of several microns. Carbon NWs had the form of one-dimensional structures 20 to 40 nm thick and about 1 μm long, composed of carbon layers oriented at an angle relative to the wire axis. Both materials contained small amounts of incorporated metal impurities, predominantly cobalt (~3–4 wt %) inclusions in NTs and nickel (up to 2 wt %) in NWs.

The effective densities of NTs and NWs were determined pycnometrically, using toluene ($d = 0.867$ g/cm^3) as the working medium. This liquid is well wetting graphitelike and fullerene materials. The measurements were performed at room temperature by introducing a weighed amount P of NT or NW powder into liquid toluene and determining the volume increment V. The relative error of the pycnometric measurements was 13%. The effective density, defined as $d = P/V$, was found to be 2.8 and 1.6 g/cm^3 for NWs and NTs, respectively.

The initial powders of NTs and NWs were charged into a special mold and pressed into thin plates with dimensions of 9.2 × 3.0 mm and a thickness of 0.2–0.6 mm. Using four silver electrodes arranged in the mold, it was possible to measure the electric conductivity of compacted samples. The molding pressure was 0.3–0.4 MPa. The densities of compact materials were 0.58 and 0.52 g/cm^3 for NTs and NWs, respectively.

It was found that the compact samples made of NWs possess elastic properties. As the pressure was increased to 7 MPa, the conductivity exhibited a 15–20% increase; upon unloading, the conductivity was restored to the initial level. Extracted from the mold, pressed NW samples were loose and exhibited fracture upon slight bending. Pressed NT samples fractured upon bending at an angle of 30°–40°.

The room-temperature ($T = 300$ K) specific conductivities of pressed NT and NW samples were $\sigma = 0.9 \times 10^3$ and 0.45×10^3 Ω^{-1} m^{-1}, respectively. The temperature dependences of σ for pressed NW and NT samples measured in the temperature interval $T = 290$–400 K are presented in the figure. A slight increase in σ in this temperature interval is evidence of a metallic character of the conductivity in both compacted materials.

The Seebeck coefficient was determined using the conventional hot probe technique. The differential thermo emf (S) was negative and amounted to –33 μV/K for compacted NTs and –7 μV/K for compacted NWs. The values for NTs are close to those obtained for a nanotubular deposit (S = 25 μV/K) studied previously [8]. The thermo emf of compacted NWs is comparable to the values typical of polycrystalline graphite [9].

1063-7850/05/3102-0159$26.00 © 2005 Pleiades Publishing, Inc.

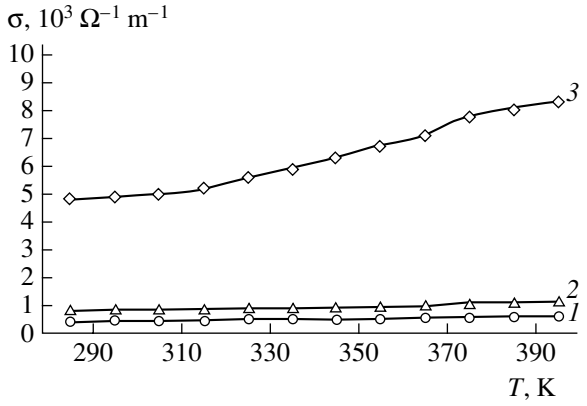

The temperature dependences of conductivity σ for compacted (*1*) NWs, (*2*) NTs, and (*3*) nanotubular deposit [8].

The above results show that the density of initial NWs exceeds that of graphite (d = 2.2 g/cm^3). This experimental result is not surprising, since the NW structure is not graphitelike. The results of electron-diffraction measurements showed the absence of indexes characteristic of graphite planes. On the other hand, the compact NW samples exhibit a rather high elasticity and behave as elastic springs on compression. From this we conclude that the NW structure is more closely packed than that of graphite and, hence, must possess a higher density.

Using the experimental data on the density and dimensions of NTs and NWs, we infer that, for an average NT bundle diameter of 20 nm and an NW diameter of 30 nm and their lengths of 3 and 1 μm, respectively, the specific surface of NTs is about 370 m^2/g and that of NWs is about 100 m^2/g. Considering their high elastic properties and relatively large electric conductivity, we may recommend using NWs as a reinforcing and conducting component in glue compositions intended for binding metallic materials.

As is known [10], the values of σ and thermo emf of compacted single-wall NTs exhibit strong variations upon adsorption of H_2, O_2, N_2 and other molecular gases. The results of our thermo emf measurements for compacted NTs (S = 33 μV/K) allow this material to be used in sensors of molecular gaseous substances and biological objects.

REFERENCES

1. R. H. Baughman, A. A. Zakhidov, and W. A. de Heer, Science **297**, 787 (2001).
2. Ph. Avouris, Chem. Phys. **281**, 429 (2002).
3. T. M. Odon, J.-L. Huang, and C. M. Lieber, Ann. Sci. **960**, 203 (2002).
4. E. G. Rakov, Khim. Tekhnol., No. 10, 2 (2003).
5. E. G. Rakov, S. N. Blinov, I. G. Ivanov, *et al.*, Zh. Prikl. Khim. (St. Petersburg) **77**, 193 (2004).
6. H. Shimoda, J. O. Sue, and H. J. Jeng, Adv. Mater. **14**, 899 (2002).
7. S. Tang, Z. Zhong, Z. Xijng, *et al.*, Chem. Phys. Lett. **350**, 19 (2001).
8. I. V. Zolotukhin, I. M. Golev, A. A. Popov, and V. P. Ievlev, Pis'ma Zh. Tekh. Fiz. **28** (16), 32 (2002) [Tech. Phys. Lett. **28**, 678 (2002)].
9. L. Yu. Maitsui, I. V. Ovsienko, and L. L. Vovchenko, Fiz. Nizk. Temp. **27**, 68 (2001).
10. J. Sumanasekera *et al.*, Phys. Rev. B **65**, 035408 (2001).

Translated by P. Pozdeev

Technical Physics Letters, Vol. 31, No. 2, 2005, pp. 161–163. Translated from Pis'ma v Zhurnal Tekhnicheskoĭ Fiziki, Vol. 31, No. 4, 2005, pp. 58–63.

Time Variation of the Mean Quantum Dot Size at the Kinetic Growth Stage

V. G. Dubrovskii[a,*] and N. V. Sibirev[b]

[a] *Ioffe Physicotechnical Institute, Russian Academy of Sciences, St. Petersburg, 194021 Russia*

[b] *Institute of Analytical Instrument Building, Russian Academy of Sciences, St. Petersburg, 198103 Russia*

** e-mail: v_dubr@mail.ru*

Received September 22, 2004

Abstract—The process of quantum dot (QD) formation in heteroepitaxial systems with lattice mismatch has been studied using theoretical and numerical methods. An analytical solution is obtained that describes time variation of the mean QD size at the kinetic growth stage. © *2005 Pleiades Publishing, Inc.*

The spontaneous formation of coherent nanodimensional islands in heteroepitaxial systems with lattice mismatch is widely used for obtaining quantum dot (QD) ensembles featuring three-dimensional (3D) quantization [1]. This paper continues theoretical investigations into the kinetics of QD formation in lattice-mismatched heteroepitaxial systems [2–5]. The aim of this study was to obtain a theoretical dependence of the mean QD size on the process time at the kinetic growth stage. Since the electrical and optical properties of QD ensembles depend to a considerable extent on the QD size, this problem is important for solving the task of creating QD ensembles with preset structures and properties [1].

Previously, we obtained a kinetic equation describing the mean lateral size of QDs at the stage of island size relaxation [2–4]:

$$\begin{cases} \tau\dfrac{dz}{dt} + \dfrac{l_0^2 N}{h_{eq}} z^{3/2} = \Phi(t), \\ z(t_*) = 0, \end{cases} \qquad (1)$$

where N is the surface number density of islands upon termination of the nucleation stage, l_0 is the mean distance between atoms on the growth surface, $\Phi(t) = H(t)/h_{eq} - 1$ is the ideal degree of system metastability, $H(t)$ is the effective thickness of a material deposited by the time t, h_{eq} is the equilibrium wetting layer thickness [6], and τ is the characteristic time of delivery of atoms from the wetting layer to islands. The function $z(t)$ is defined as $(L_*(t)/\alpha l_0)^2$, where $L_*(t)$ is the most representative (average) lateral size of islands formed at the moment of time t_* corresponding to the maximum wetting layer thickness, $\alpha = (6d_0 \cot\theta/l_0)^{1/3}$, θ is the contact angle at the island side face, and d_0 is the atomic monolayer (ML) height.

Following [4], let us introduce the dimensionless length $l(t) \equiv L_*(t)/L_R$ and dimensionless time $t \longrightarrow t/t_R$, where L_R is the characteristic lateral size of islands upon termination of the size relaxation stage and t_R is the characteristic time of this relaxation process. The L_R and t_R values are given by the formulas [4]

$$t_R = \frac{2}{3}\tau\frac{1}{\Phi_0^{1/3}}\left(\frac{h_{eq}}{l_0^2 N}\right)^{2/3}, \qquad (2)$$

$$L_R = \left(\frac{6d_0(H_0 - h_{eq})}{N}\cot\theta\right)^{1/3}, \qquad (3)$$

where $\Phi_0 = H_0/h_{eq} - 1$ is the ideal degree of system metastability upon termination of the deposition process and H_0 is the effective thickness of a deposited layer with QDs. In the case of molecular beam epitaxy (MBE) at a constant deposition rate V, the function $\Phi(t)$ involves two characteristic times: $t_{eq} = h_{eq}/V$ is the time required for the formation of a wetting layer with equilibrium thickness, and t_0 is the time of termination of the deposition stage [2]. The time variation of the degree of metastability is described by the expressions $\Phi(t) = V(t - t_{eq})/h_{eq}$ for $t < t_0$ and $\Phi(t) = V(t_0 - t_{eq})/h_{eq} = \Phi_0$ for $t > t_0$.

Introducing the notation $\varphi^3(t) = \dfrac{\Phi(t)}{\Phi_0}$, we can rewrite Eq. (2) as

$$\begin{cases} 3l\dfrac{dl}{dt} + l^3 = \varphi^3(t), \\ l(t_*) = 0. \end{cases} \qquad (4)$$

The physical meaning of Eq. (4) is as follows. For φ = const, this relation describes the time variation of the

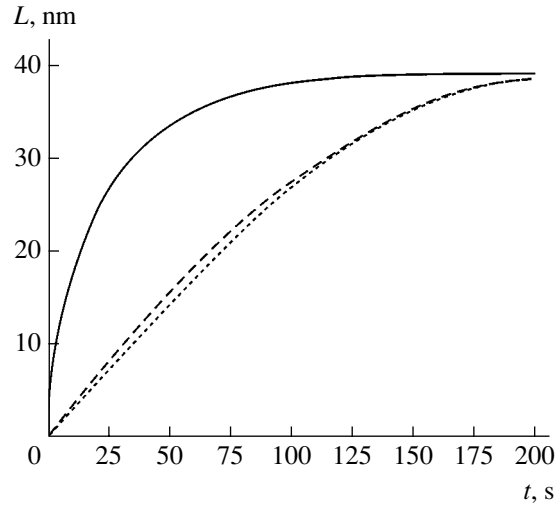

Fig. 1. The results of numerical analysis of Eqs. (4), (5), and (12) for the values of parameters typical of the Ge/Si(100) system (d_0 = 0.145 nm, h_{eq} = 2.6 ML, θ = 20°, $N = 2 \times 10^{10}$ cm^{-2}, τ = 0.0296 s, l_0 = 0.395 nm, ε = 0.07) [2] with an effective thickness of Ge deposit H_0 = 7.1 ML and a deposition rate of M = 0.03 ML/s. The solid curve shows solution (5), the dotted curve represents the exact numerical solution of Eq. (4), and the dashed curve shows approximate solution (12).

mean QD size at a constant amount of deposited material, while the slow (as compared to the rate of variation of the island size) change of φ with time reflects variation of the total amount of deposited material due to adsorption. It is assumed that the effective thickness H_0 is not much greater than the critical thickness corresponding to the transition from 2D to 3D growth, which is typical of the growth of coherent islands. For this reason, the mean QD size exhibits stabilization at a value corresponding to H_0, whereby the metastability of the system tends to zero and the secondary nucleation of islands does not take place [7].

If the φ value is independent of time, the exact solution of Eq. (4) obtained previously [4] has the form $l = \varphi\lambda(\varphi\tau)$, where the function $\lambda(t)$ is determined from the relation

$$t - t_* = \ln\left(\frac{\sqrt{1+\lambda+\lambda^2}}{1-\lambda}\right) - \sqrt{3}\arctan\left(\frac{2\lambda+1}{\sqrt{3}}\right) + \frac{\pi}{2\sqrt{3}}. \quad (5)$$

Equation (4) is solved here under the condition that

$$\varepsilon = \frac{t_R}{3(t_0 - t_{eq})} \ll 1. \quad (6)$$

The smallness of ε is provided by the hierarchy of characteristic times involved in various stages of island nucleation and growth [2–4]. Physically, condition (6) implies that island size relaxation is a more rapid process than deposition of a material layer with an effective thickness H_0. Introducing $f(\varepsilon t) = \varphi(t)$, one can readily check that the function f and its time derivative are on the same order of magnitude. A solution to Eq. (4) will be found in the form of an asymptotic series

$$l(t) = \lambda[f(\varepsilon t)t](f(\varepsilon t) + \delta(t)),$$
$$\delta(t) \equiv \sum_{k=1}^{\infty} \varepsilon^k \delta_k(t). \quad (7)$$

Substituting this series into Eq. (4) and taking into account the relations $3\lambda\lambda' f^3 + \lambda^3 f^3 = f^3$ and $3\lambda\lambda' = 1 - \lambda^3$, we arrive at a differential equation for $\delta(t)$. Equating terms of the same power in ε, we obtain

$$\delta_k'(t) + g(t)\delta_k(t) + h_k(t) = 0,$$
$$\delta_k(0) = 0, \quad (8)$$

where

$$g(t) = \frac{2 + \lambda^3[\varphi(t)t]}{3\lambda^2[\varphi(t)t]}\varphi(t), \quad (9)$$

$$h_1(t) = \left(1 + \frac{(1 - \lambda^3[\varphi(t)t])t\varphi(t)}{3\lambda^2[\varphi(t)t]}\right)f'(\varepsilon t), \quad (10)$$

and the other $h_k(t)$ functions are also readily found. Each linear equation of the type of Eq. (10) has a solution

$$\delta_k(t) = \int_0^t dt' h_k(t') \exp\left(-\int_{t'}^t g(t'')dt''\right). \quad (11)$$

Even the first approximation

$$l_1(t) = \lambda[f(\varepsilon t)t](f(\varepsilon t) + \delta_1(t)) \quad (12)$$

provides for a much more accurate approach to the true solution than $\lambda(t)$ found in [4]. Figure 1 shows the results of numerical analysis of Eqs. (5), (6), and (12) in a typical case of MBE at a constant deposition rate and a constant substrate temperature. As can be seen, expression (12) well approximates the exact solution, while solution (6) obtained previously gives obviously (sometimes, more than twofold) overstated mean QD sizes at all times. Thus, solution (12) stipulates a smoother variation of the mean QD size at the kinetic growth stage. These conclusions are confirmed by Fig. 2, which presents a comparison of the results of numerical modeling of Eqs. (5), (6), and (12) plotted as L versus the effective thickness of the deposit for the

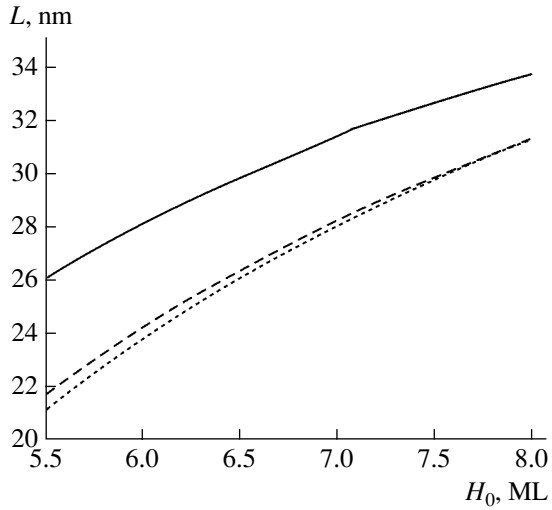

Fig. 2. A comparison of the results of numerical modeling of Eqs. (4), (5), and (12) for the Ge/Si(100) system with various effective deposit thicknesses H_0 by the time of termination of the deposition process (h_{eq} = 2.6 ML, θ = 20°, $N = 2 \times 10^{10}$ cm^{-2}). The solid curve shows solution (5), the dotted curve represents the exact numerical solution of Eq. (4), and the dashed curve shows approximate solution (12).

process of hut cluster formation in the Ge/Si(100) system [4] by the time of termination of the deposition process.

In conclusion, we have constructed an analytical solution of the equation for the mean QD size, which gives a good approximation to the exact solution. The obtained results provide an exact prediction of the mean QD size for a given effective deposit thickness and sample exposure time and can be used in investigations of the process of QD formation in heteroepitaxial systems such as InAs/GaAs and Ge/Si.

REFERENCES

1. D. Bimberg, M. Grundmann, and N. N. Ledentsov, *Quantum Dot Heterostructures* (Wiley, Chichester, 1998).
2. V. G. Dubrovskii, G. E. Cirlin, Yu. G. Musikhin, *et al.*, J. Cryst. Growth **267**, 47 (2004).
3. V. G. Dubrovskii, Yu. G. Musikhin, G. E. Tsyrlin, *et al.*, Fiz. Tekh. Poluprovodn. (St. Petersburg) **38**, 342 (2004) [Semiconductors **38**, 329 (2004)].
4. V. G. Dubrovskii, G. E. Cirlin, and V. M. Ustinov, Phys. Rev. B **68**, 075409 (2003).
5. A. V. Osipov, F. Schmitt, S. A. Kukushkin, and P. Hess, Appl. Surf. Sci. **188**, 156 (2002).
6. P. Müller and R. Kern, Appl. Surf. Sci. **102**, 6 (1996).
7. A. V. Osipov, S. A. Kukushkin, F. Schmitt, and P. Hess, Phys. Rev. B **64**, 205421 (2001).

Translated by P. Pozdeev

Technical Physics Letters, Vol. 31, No. 2, 2005, pp. 164–166. Translated from Pis'ma v Zhurnal Tekhnicheskoĭ Fiziki, Vol. 31, No. 4, 2005, pp. 64–70.

Modeling the Formation of a Deep Potential Well in a Vacuum Diode

S. A. Barengol'ts*, N. Yu. Kazarinov, G. A. Mesyats, É. A. Perel'shteĭn, and V. F. Shevtsov

Natural Sciences Center, Prokhorov Institute of General Physics, Russian Academy of Sciences, Moscow, 117924 Russia

Joint Institute for Nuclear Research, Dubna, Moscow oblast, 141980 Russia

Institute of Electrophysics, Ural Division, Russian Academy of Sciences, Yekaterinburg, 620219 Russia

** e-mail: sb@nsc.gpi.ru*

Received September 28, 2004

Abstract—The formation of a deep nonstationary potential well in the gap between the cathode flare front and the anode has been modeled with allowance for a floating potential at the boundary of an expanding plasma. It is shown that a long-lived potential well with a lifetime on the order of nanoseconds can form in the vacuum diode. The obtained results provide an explanation of the phenomenon of collective ion acceleration at the spark stage of vacuum discharge. © *2005 Pleiades Publishing, Inc.*

Introduction. Despite the fact that quite clear notions have been developed by now about the physics of spark discharge in vacuum [1], one of the most interesting effects accompanying the operation of this discharge is still the subject of discussion and controversy. The effect, which was originally observed by Plyutto [2] in a plasma diode, is manifested by the generation of anomalously accelerated positive ions in the form of short-lived clusters (bunches) moving from the cathode toward the anode. The energy of these ions is considerably higher than that corresponding to the potential difference U_A applied to the discharge gap: for instance, at U_A = 300 kV, the ion energies in a vacuum diode reach 10–15 MeV [3]. An important feature of the spectrum of light ions is that the maximum ion energy $\sim 3ZeU_A$ is proportional to the ion charge Z. These ion energies can only be attributed to the existence of strong collective interactions between electrons and ions of the cathode plasma.

A theory of the Plyutto effect in a vacuum diode has been developed [4] based on the idea of the formation of a deep nonstationary potential well [5, 6] that was previously successfully used in the model of collective ion acceleration in the case of electron beam injection in a gas. In order to demonstrate the possible appearance of a deep nonstationary potential well in a vacuum diode, the model constructed in [5] was used to solve a nonstationary one-dimensional problem concerning the formation of a virtual cathode upon injection of a high-current electron beam into a diode with an accelerating electron field [4]. According to the model adopted, a monoenergetic electron beam with an electron velocity v_0 and a density n_0 = const was injected at $t = 0$ into the half-space $x > 0$ (behind the cathode plane $x = 0$), where electrons moved in a homogeneous external electric field E_0. It was found that, provided the conditions of the potential well formation are satisfied, the depth eU of a nonstationary potential well is independent of the accelerating field: $eU = -\frac{8}{3}W$, where W is the kinetic energy of an electron.

However, the theory [4] was constructed using certain simplifying assumptions restricting the domain of validity of the results. In particular, the self-field of the electron beam was calculated for the half-space bounded by the grounded cathode plane. The analytical model used in [4, 5] had a hydrodynamic character and was valid only before the formation of a multivelocity electron flow (i.e., before the first reflection of particles) as a result of the appearance of the virtual cathode. Finally, the analytical model [4] was nonrelativistic. Recently, these limitations were analyzed in a study [7] devoted to numerical simulation of a beam entering the gap between the cathode flare front and the anode.

In a vacuum diode, the cathode flare front (expanding plasma front) moves in space and occurs in a floating potential. However, a change in the position of this front during the time of virtual cathode formation is insignificant. For this reason, the cathode flare front was assumed in [7] (as well as in [4]) to be immobile and occurring at a constant potential. The electron beam dynamics was simulated for electrons at the plasma front accelerated in the space charge field of ions, while the return of reflected electrons to the gap between the plasma front and the anode (i.e., their sec-

1063-7850/05/3102-0164$26.00

ondary reflection) was not taken into account. Since the current in the case of plasma rupture significantly exceeds the Langmuir value (corresponding to the gap between the plasma front and the anode), the problem was simplified by assuming that the gap did not contain electrons at the initial moment. The results of numerical simulation [7] generally confirmed the analytical model [6], but the use of a constant potential at the plasma front and the loss of reflected electrons led to a significantly understated lifetime of the deep potential well in the numerical experiment.

In this study, the numerical simulation has been performed with allowance for the floating potential in front of the cathode flare and the possible secondary reflection of electrons in this region. The size of the charged plasma region at the plasma front is on the order of the Debye radius, which is much smaller than the size of the neutral plasma region and the gap width between the plasma front and the anode. The electric field in this region is created by an external source and the charged plasma formed by immobile ions and backscattered electrons of the beam. For simplicity, the electric field of the ions is replaced by the field of a positively charged electrode situated at a distance d_i from the cathode (d_i is much shorter than the interelectrode distance d). Thus, the electron beam dynamics is simulated in triode geometry with a floating potential at the grid.

Numerical simulation. The simulation was performed by the particle in cell method (the same as that used in [4]). The particles (plane charged layers) move along the x axis in the gap between the plasma front and the anode in accordance with the equations of motion

$$\frac{dx}{d\tau} = \beta, \qquad \frac{d\beta}{d\tau} = \frac{eE}{mc^2}(1-\beta^2)^{3/2}, \quad \tau = ct. \tag{1}$$

Here, $\beta = v/c$ is the relative velocity of a particle, t is the current time, $E = E_0 + E_s$, and E_s is the self-field of the electron beam, defined as

$$E_s = -\frac{d\Phi}{dx}. \tag{2}$$

The self-field is determined by solving the Poisson equation

$$\frac{d^2\Phi}{dx^2} = -4\pi en, \tag{3}$$

where Φ is the scalar potential created by the beam with charge density en.

The total potential in the system is defined as

$$U = \frac{U_i}{d_i}x + \Phi \text{ for } 0 < x < d_i;$$

$$U = \frac{U_A - U_i}{d - d_i}x + \Phi \text{ for } d_i < x < d,$$

where U_i is the potential at the ion layer boundary and $x = 0$ corresponds to the boundary between neutral plasma and the ion layer. The boundary conditions were selected so as to correspond to zero potential $\Phi = 0$ at $x = 0$ and on the anode. Equation (3) was solved by method of fast Fourier transform. The fields were determined by numerical differentiation of the potential at the adjacent nodes of the lattice.

At the initial moment, particles were uniformly distributed along the beam length in the region in front of the cathode flare. Then, the particles were injected into the gap at a constant velocity. The energy of injected electrons must correspond to a potential drop across the neutral part of the plasma column. However, in order to increase the calculation speed, we used particles with the energies greater than thermal energy, though still much lower than the energies acquired in the ion layer. The number of particles was varied (depending on the conditions of the numerical experiments) from 10^5 to 3×10^5. The gap was divided by the lattice with a constant step, so that the number of nodes varied from 2^8 to 2^{12}. The charge density was determined by counting the number of particles at the lattice nodes, whereby each particle was assigned to adjacent nodes with the weights $w_i = 1 - \frac{|x - x_i|}{h}$, where x_i is the coordinate of the ith lattice node and h is the lattice step. The accuracy of the calculations was checked by comparing the results to those obtained in the previous numerical experiment [4].

Results and discussion. In the course of the simulation of the evolution of a potential U in the gap between the cathode flare front and the anode, the main parameters were selected close to the known experimental values [3], taking into account the approximate equality $U_F \approx U_A$ [8]. Figure 1 shows the evolution of the relative potential well depth U/U_A in the gap, which was calculated for the following parameters: injected current density, $j_0 = 13$ kA/cm^2; accelerating gap length, $d = 0.7$ cm; ion layer width, $d_i = 0.01d$ (for a Debye radius, $d_D \approx 50$ μm); potential difference, $U_A - U_i = 60$ kV; applied voltage $U_A = 300$ kV. The critical current density for the gap between the cathode flare front and the anode, above which a deep potential well is formed, is given by the expression [7]

$$j_{thr} = I_A \frac{\beta_0^3}{\pi(d - d_i)^2},$$

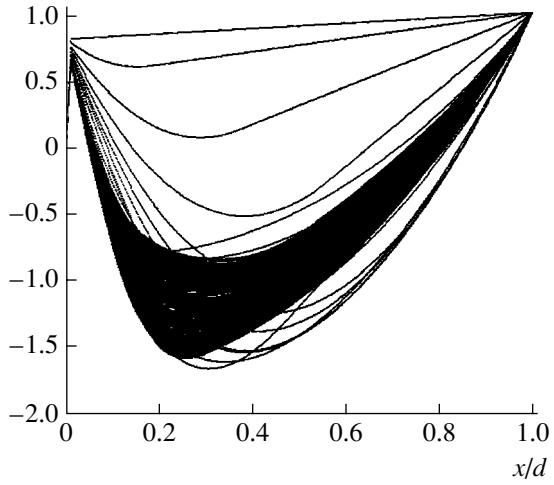

Fig. 1. Evolution of the total potential distribution in the gap between the cathode flare front and the anode (with 15-ps time intervals).

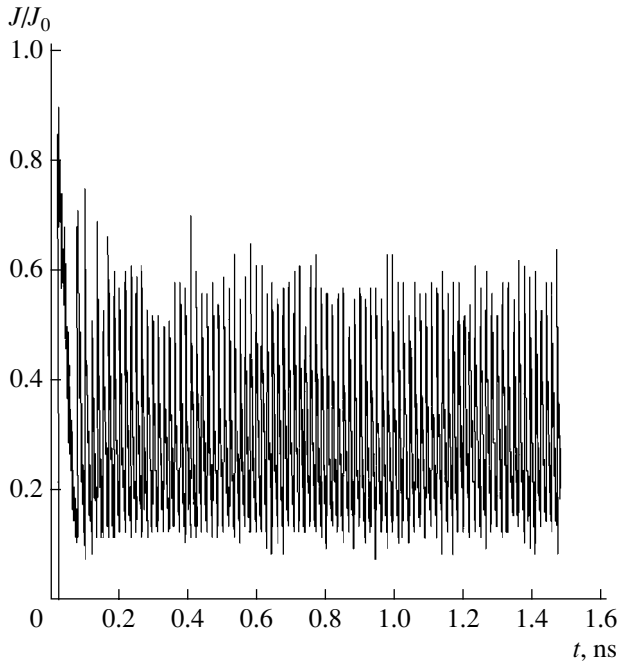

Fig. 2. Time series of the relative anode current density for an electron beam in the model vacuum diode.

where $I_A = mc^3/e \cong 17$ kA is the Alfvén current and β_0 is the relative velocity of electrons accelerated in the ion layer. For the selected parameters, $j/j_{thr} \approx 1.5$.

Figure 2 shows the ratio of the anode current to the current at the plasma front calculated for the above parameters. A comparative analysis of the data presented in Figs. 1 and 2 shows that the adopted vacuum diode model described above is characterized by a rapid formation of a deep potential well with a lifetime on the order of nanoseconds. The breakdown of the current outburst is probably determined by processes accompanying the propagation of the charged plasma region into denser layers of neutral plasma, which determines the rear front of the injected current. These processes fall outside the framework of the model under consideration and require additional investigation. As can be seen from Fig. 1, the depth of the potential well is about $2.4U_A$. The average anode current density at the outburst is about 8 kA/cm^2. Since the quasi-stationary oscillations of the anode current density in the numerical experiment are about 1.2 kA/cm^2, this result agrees well with the experimental data reported in [3].

Thus, taking into account the experimental fact of a significant increase in the potential at the cathode flare front (up to a level comparable with the applied voltage) and admitting rupture of a rare plasma at the boundary, our numerical simulation of the electron dynamics in a vacuum diode (with allowance for the floating potential and multiple reflections of electrons at the plasma front) showed the possibility of a potential well existing for a long time (on the order of nanoseconds) in the diode. In agreement with [4], this explains the collective acceleration of electrons to high energies in such diodes.

Acknowledgments. This study was supported by the Russian Foundation for Basic Research, project no. 02-02-17002.

REFERENCES

1. G. A. Mesyats, *Cathode Phenomena in Vacuum Discharge: the Breakdown, the Spark, and the Arc* (Nauka, Moscow, 2000).
2. A. A. Plyutto, Zh. Éksp. Teor. Fiz. **39**, 1589 (1960) [Sov. Phys. JETP **12**, 1106 (1960)].
3. E. D. Korop and A. A. Plyutto, Zh. Tekh. Fiz. **40**, 3534 (1970) [Sov. Phys. Tech. Phys. **15**, 1986 (1970)].
4. S. A. Barengol'ts, G. A. Mesyats, and E. A. Perel'shteĭn, Zh. Éksp. Teor. Fiz. **118**, 1358 (2000) [JETP **91**, 1176 (2000)].
5. J. W. Poukey and N. Rostoker, Plasma Phys. **13**, 897 (1971).
6. C. L. Olson and U. Schumacher, *Collective Ion Acceleration* (Springer-Verlag, Berlin, 1979).
7. S. A. Barengolts, N. Yu. Kazarinov, G. A. Mesyats, *et al.*, IEEE Trans. Plasma Sci. **31**, 847 (2003).
8. G. P. Bazhenov, O. B. Ladyzhenskiĭ, S. M. Chesnokov, and V. G. Shpak, Zh. Tekh. Fiz. **49**, 117 (1979) [Sov. Phys. Tech. Phys. **24**, 67 (1979)].

Translated by P. Pozdeev

Technical Physics Letters, Vol. 31, No. 2, 2005, pp. 167–168. Translated from Pis'ma v Zhurnal Tekhnicheskoĭ Fiziki, Vol. 31, No. 4, 2005, pp. 71–75.

Shock-Spall Asymmetry in High-Velocity Impact of Solids

I. E. Khorev

Tomsk State University of Control Systems and Radioelectronics, Tomsk, Russia

e-mail: khorev@main.tusur.ru

Received September 28, 2004

Abstract—A new, previously unreported physical phenomenon has been observed in experiments with high-velocity impact of various strikers on metal targets of finite thickness. According to this, sufficiently strong and tough structural materials (armor steel, titanium alloys, etc.) exhibit fractionation of the spall plate formed upon dynamic contact with the striker or its deformed part. This always results in an odd number of fragments (three, five, seven, etc.) of similar configuration. Systematic experiments on retained samples revealed progressive fractionation of the spall plates, with the number of fragments increasing up to eleven. Further evolution was difficult to follow because trapping of the fragments was hindered by their high velocities, which led to unavoidable additional fragmentation of the spall plates in the course of their interaction with a gradient package of trapping material (ranging from felting to sand). © *2005 Pleiades Publishing, Inc.*

The results of systematic investigations devoted to the high-velocity impact of various strikers on metal targets of finite thickness have revealed a new physical phenomenon, which it is suggested to call shock-spall asymmetry and which is observed in experiments on retained samples for a rather broad variation of the striker size (1 g to 1 kg) and shape (compact to elongated).

It was established [1] that the time of spall damage development during high-velocity collisions of various strikers (compact and elongated bullets and projectiles) with targets of finite thickness may be comparable to the time of penetration of the striker or its deformed part through the target, which leads to a contact interaction of the spall plate with the striker. In the case of a plastic target material, this results in the formation of a through hole in the spall plate, with a diameter equal to that of the projectile (or its deformed part). In sufficiently hard structural materials, the spall plate exhibits fragmentation. This pattern was confirmed by independent experiments involving X-ray radiographic monitoring of the process of striker penetration through a target and trapping of the spall plates in special devices.

This pattern of interaction between a striker and a spall plate was also confirmed by the results of parametric theoretical investigations involving the initial and boundary conditions matched with experiment. Numerical simulations of the high-velocity interaction of various strikers with targets of finite thickness and the process of target fracture in axisymmetric geometry were performed using the method of finite elements [2]. In the general case, the interaction involving finite-size bodies is modeled by a compressible viscoelastic medium. The behavior of this medium under dynamic loading conditions is characterized by the shear modulus, dynamic yield point, and parameters of the adopted kinetic model of fracture describing the nucleation and evolution of microscopic damage continuously modifying the material properties and inducing the relaxation of stresses [3].

In this study, the shock-spall fracture of structural materials was simulated based on the notions of a continuous measure of damage, which was represented by the specific volume of cracks [4]. The rate of increase in the specific volume of cracks was set as a function of the acting pressure and the existing volume of cracks. In the course of fracture, the strength properties of the medium decrease according to certain laws [5]. This approach was used for the numerical simulation and analysis of the interaction of flat targets with various strikers representing three characteristic types: platelet, compact (a ball or a cylinder with the height equal to the diameter), or elongated (a sharp-ended bullet or a rod). The results of numerical calculations showed convincing evidence that both compact (having comparable dimensions in all directions) and elongated (a sharp-ended bullet or a rod) strikers interact with a spall plate and break through this plate.

Systematic experiments on retained samples, with trapping of the spall plate fragments, showed that sufficiently strong and tough structural materials (armor steel, titanium alloys, etc.) exhibit fractionation of the spall plate formed upon dynamic contact with the striker or its deformed part. This always results in an odd number of fragments (three, five, seven, etc.) of similar configurations.

Figure 1a presents a photograph of the cross sections of a broken steel target (HB, 300 kgf/mm^2). Figure 1b shows the photographs of trapped spall plate

1063-7850/05/3102-0167$26.00

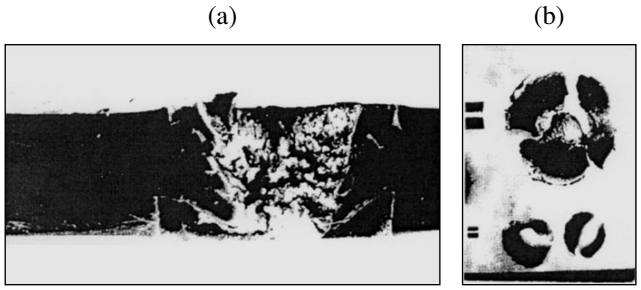

Fig. 1. Photographs of retained samples: (a) cross section of a broken target along a symmetry plane; (b) model strikers (left) and trapped broken (top) and intact (bottom) spall plates.

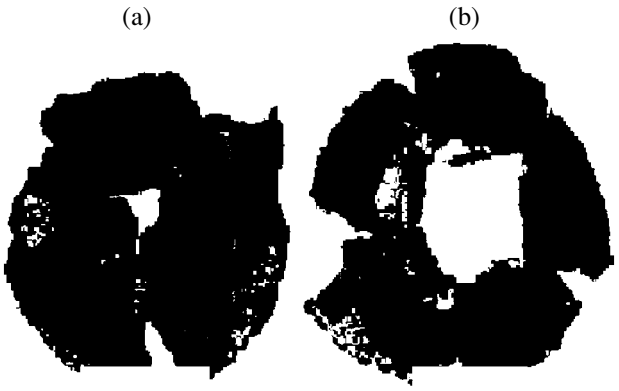

Fig. 2. Trapped fragments of spall plates formed upon perforation of a steel target by elongated strikers of different configurations (see the text).

fragments: (top) three fragments formed upon impact at a velocity of 3386 m/s and (bottom) intact spall plates not broken by a striker incident at a lower velocity (about 3010 m/s); Fig. 1b (left part) also shows the strikers of different weight (compact cylinders with the height equal to the diameter) used in this series of experiments.

Figure 2 shows the spall fragments trapped in the experiments with 22-mm-thick steel targets (HB, 300 kgf/mm^2). The three fragments in Fig. 2a were formed upon an impact at 1988 m/s using a rodlike striker with a diameter of d = 11.4 mm and an aspect ratio (the ratio of cylinder length l to diameter d) of $\lambda = l/d = 4$; five fragments in Fig. 2b were trapped upon an impact at 1688 m/s using a rodlike striker with a diameter of d = 6.7 mm and an aspect ratio of $\lambda = 12$. The results of experiments on retained samples revealed progressive fractionation of the spall plates, with the number of fragments increasing up to eleven. Further evolution was difficult to follow because trapping of the fragments was hindered by their high velocities (it is necessary either to increase the impact velocity or reduce the target thickness), which led to unavoidable additional fragmentation of the spall plates in the course of their interaction with a gradient package of trapping material (ranging from felting to sand).

Thus, a new, previously unreported physical phenomenon has been observed in experiments with dynamic loading of metals and alloys by means of the high-velocity impact of various strikers. According to this, perforation of the targets of finite thickness by a high-velocity striker (compact or elongated) is accompanied by the interaction of a spall plate with the striker. In the case of sufficiently strong and tough structural materials (armor steel, titanium alloys, etc.), the spall plate always breaks into an odd number of fragments. This phenomenon is of considerable basic interest and practical significance related to the development of a theory of the dynamic fracture of various materials, the physics and mechanics of projectiles breaking through thick and complex structures, the formation of spall fragment fluxes, etc. [6, 7]. A theoretical explanation of the observed phenomenon and development of the corresponding physicomathematical model would be of interest from both a basic and practical standpoint.

Acknowledgments. This study was supported by the Russian Foundation for Basic Research, project no. 03-01-00386.

REFERENCES

1. I. E. Khorev and V. A. Gorel'skiĭ, Dokl. Akad. Nauk SSSR **256**, 623 (1983) [Sov. Phys. Dokl. **28**, 588 (1983)].
2. G. R. Johnson, J. Appl. Mech. **44**, 95 (1977).
3. I. E. Khorev and V. A. Gorel'skiĭ, in *Proceedings of the 2nd All-Union Symposium on Detonation, Chernogolovka, 1981*, Vol. 2, pp. 149–152.
4. G. I. Kanel', S. V. Razorenov, A. V. Utkin, and V. E. Fortov, *Impact–Wave Phenomena in Condensed Media* (Yanus-K, Moscow, 1996) [in Russian].
5. G. I. Kanel' and V. V. Shcherban', Fiz. Goreniya Vzryva, No. 4, 93 (1980).
6. I. E. Khorev, S. A. Zelepugin, A. A. Konyaev, *et al.*, Dokl. Akad. Nauk **369**, 481 (1999) [Dokl. Phys. **44**, 818 (1999)].
7. A. V. Radchenko, V. E. Fortov, and I. E. Khorev, Dokl. Akad. Nauk **389**, 49 (2003) [Dokl. Phys. **48**, 126 (2003)].

Translated by P. Pozdeev

Technical Physics Letters, Vol. 31, No. 2, 2005, pp. 169–172. Translated from Pis'ma v Zhurnal Tekhnicheskoĭ Fiziki, Vol. 31, No. 4, 2005, pp. 76–82.

Instability of the Background Electron Multiplication Wave Front

S. I. Yakovlenko

Institute of General Physics, Russian Academy of Sciences, Moscow, 117924 Russia

e-mail: syakov@kapella.gpi.ru

Received September 20, 2004

Abstract—The initial stage of the development of instability in the front of an ionization wave, which is related to the multiplication of electrons at their small background density, is theoretically described. An analytical expression is obtained for the growth rate of small perturbations as a function (universal for the given gas) of the reduced field strength E/p (where E is the electric field strength and p is the gas pressure). The rate of instability development is calculated for helium, xenon, nitrogen, and sulfur hexafluoride. A new criterion of streamer formation is found. © *2005 Pleiades Publishing, Inc.*

Introduction

It was pointed out previously [1–5] that the propagation of electric discharge in a dense gas is sometimes determined by multiplication of the electrons present at a small background density rather than by the transfer of electrons or photons in the medium. The density of such electrons exhibits significant growth at a value of the applied electric field strength below (but close to) the breakdown threshold [2, 4, 5]. The most intense electron multiplication takes place at a conducting surface, where the field strength exhibits growth. The multiplication wave frequently propagates in the form of relatively narrow channels. This mechanism of discharge propagation is independent of the electric field orientation, which makes it possible to reject the well-known hypothesis of streamer propagation [6]. Solving the problem of description of the ionization wave propagation in a dense gas is also important for understanding the mechanism of high-power subnanosecond electron beam formation in gases at atmospheric pressure [7, 8].

This Letter is devoted to an analysis of the stability of the electron multiplication wave front.

Background Electron Multiplication Wave

Electron multiplication wave front velocity. It was previously demonstrated [1–5] that propagation of the background electron multiplication wave can be described using a simple model. Within the framework of this model, the electron density N_e at a point with the radius vector $\mathbf{r}$ at the time t can be expressed as

$$N_e(\mathbf{r}, t) = \begin{cases} N_0 \exp[\nu_i(E(\mathbf{r}))\mathbf{t}] & \text{for } N_0 \exp[\nu_i(E(\mathbf{r}))t] < N_{cr}, \\ N_{cr}, & \text{for } N_0 \exp[\nu_i(E(\mathbf{r}))t] \geq N_{cr}, \end{cases} \quad (1)$$

where N_0 is the background plasma density, N_{cr} is the critical value of this density that provides for the complete screening of the external field, E is the electric field strength, and ν_i is the ionization rate.

An expression for the multiplication wave front velocity obtained using relation (1) is as follows:

$$u_{fr} = \frac{\nu_i r_0}{\zeta(E_0/p)},$$
$$\zeta(E_0/p) = 2\mathrm{Ln}\left(\frac{d\ln(u_{de}(E/p)\xi(E/p))}{d\ln(E/p)}\right)_{E/p = E_0/p}, \quad (2)$$

where $E_0 = E(z(0))$ is the field strength on the front surface, r_0 is the radius of the sphere approximating the front surface, p is the neutral gas pressure, and $\mathrm{Ln} \equiv \ln(N_{cr}/N_0)$. The ionization rate $\nu_i = \alpha_i u_{de}$ is expressed as a product of the Townsend coefficient $\alpha_i(E, p) = p\xi(E/p)$ and the electron drift velocity $u_{de}(E/p)$, where $\xi(E/p)$ is the function characteristic of a given gas. It was established [9–12] (see also reviews [7, 8]) that the ionization rate $\nu_i(E/p)$ exhibits a maximum at a certain value of $E/p = (E/p)_{cr}$. In what follows, consideration will be restricted to the region of not very strong fields such that $E/p < (E/p)_{cr}$.

Factors accounting for the development of instability. As can be seen from Eq. (2), the multiplication front propagation velocity in the case of a plane wave becomes infinitely large, which implies that ionization takes place simultaneously in the entire volume. In real systems, the volume mechanism of ionization is unstable. The behavior of both streamer and spark discharge is determined by this instability.

The conclusion that a plane wave front has to be unstable is confirmed by simple considerations. Indeed, let the plane front be distorted for some reason so that

it exhibits small protrusions and depressions. The electric field lines will concentrate on the protrusions and, accordingly, the electron multiplication rate and the front propagation velocity at these points will increase. Therefore, the protrusions will tend to grow, the field will continue to concentrate, and so on.

In order to calculate the shape of the resulting plasma bunch, it is necessary to consider Eq. (1) together with a two- or even three-dimensional Laplace equation. Below, consideration is restricted to the case when the multiplication wave front perturbation can be considered to be small. The approach is analogous to that used in monograph [6] for the description of a different mechanism of the ionization front propagation.

Initial Stage of Perturbation Growth

Perturbation potential. In the absence of a perturbation, let us treat the multiplication wave front as a flat conductor propagating at a velocity v along the z axis, assuming the potential on the front surface to be zero. Variation of the unperturbed potential φ_0 as a function of the coordinate and time is described by the expression $\varphi_0 = -E_0(z - u_{fr}t)$, where E_0 is the field strength on the front surface.

Consider a small perturbation of the front surface in the form of a plane wave with a frequency ω and a wave number k. The related displacement in the direction perpendicular to the surface can be expressed as

$$\xi(x, t) = \xi_0 \exp[i(kx - \omega t)],$$

where ξ_0 is the displacement amplitude.

The perturbation gives rise to a small additive in the potential, so that $\varphi = \varphi_0 + \varphi_1$. The additive φ_1, as well as the total φ, must obey the Laplace equation $\Delta\varphi_1 = 0$ and tend to zero as $z \longrightarrow \infty$. In addition, the additive has to satisfy the condition of zero potential, $\varphi(z) = 0$, at the front of the electron multiplication wave, that is, at $z = u_{fr}t + \xi = u_{fr}t + \xi_0\exp[i(kx - \omega t)]$. In the case of a small perturbation ($k\xi_0 \ll 1$), all these conditions are met by the function $\varphi_1 = -E_0\xi_0\exp[i(kx - \omega t) - k(z - u_{fr}t)]$. Thus, the perturbed potential can be expressed as [6]

$$\varphi = -E_0\{(z - u_{fr}t) - \xi_0 \exp[i(kx - \omega t) - k(z - u_{fr}t)]\}. \quad (3)$$

Perturbation growth rate. The condition of constancy of the potential φ at the wave front can be expressed as

$$\begin{aligned} d\varphi/dt &= \partial\varphi/\partial t \\ + (\partial z/\partial t)\partial\varphi/\partial z\varphi &= \partial\varphi/\partial t + u_{fr}\partial\varphi/\partial z = 0. \end{aligned} \quad (4)$$

Substituting the expression for potential (3) into condition (4) and ignoring the dependence of the ionization wave propagation velocity u_{fr} on the field strength E, we obtain $i\omega = 0$. This implies that the small perturbation ξ in this case does not change with time (indifferent equilibrium).

However, in fact the wave propagation velocity at $E/p < (E/p)_{cr}$ increases with the electric-field strength. For a small variation of the field, $|\nabla\varphi_1|$, we have

$$u_{fr}(E) = u_{fr}(E_0) + (du_{fr}/dE)\big|_{E0}|\partial\varphi_1/\partial z|.$$

Substituting this expression into condition (4) and ignoring small terms on the order above linear with respect to ξ_0, we obtain

$$\omega = i\gamma, \quad \gamma = k(du_{fr}/dE)\big|_{E0}E_0, \quad (5)$$

where γ is the growth rate of the small perturbation amplitude. The fact that this value is positive (together with the derivative $(du_{fr}/dE)_{E0}$) indicates that the small perturbation exhibits exponential growth or, in other words, the electron multiplication wave front exhibits instability.

Discussion of Results

Perturbation growth rate as a function of the field strength. Using relation (2), the expression for perturbation growth rate (5) can be rewritten as

$$\gamma = kr_0\left(\frac{d}{dE}\frac{\nu_i}{\xi}\right)\Big|_{E = E_0}E_0. \quad (6)$$

In the case when the perturbation determines the radius of curvature of the wave front inhomogeneity, the quantity kr_0 is on the order of unity.

Based on the results obtained in [7–12], it is possible to determine universal dependences of the perturbation growth rate on the reduced field strength E/p at the wave front for $kr_0 = 1$ as

$$\gamma_0 = \left(\frac{d}{d(E/p)}\frac{\nu_i}{\zeta}\right)\Big|_{E = E_0}(E_0/p). \quad (7)$$

The results of calculations of the electron multiplication wave characteristics for helium, xenon, nitrogen, and sulfur hexafluoride are presented in the figure. It should be noted that, for $E/p < 1/2(E/p)_{cr}$, the ionization rate is significantly greater than the perturbation growth rate: $\nu_i/\gamma_0 \sim 2\text{Ln} \gg 1$. The results of calculations show that the characteristic distance traveled by the wave front during the time $1/\gamma_0$ of instability development is on the order of $u_{fr}/\gamma_0 \approx (0.3–0.8)r_0$. This implies that the streamer head splits into separate bunches with characteristic transverse size much smaller than r_0. The stability of the streamer at the initial stage of the instability development is probably related to finiteness of the screening layer and to the limited plasma conductivity [6]. In the

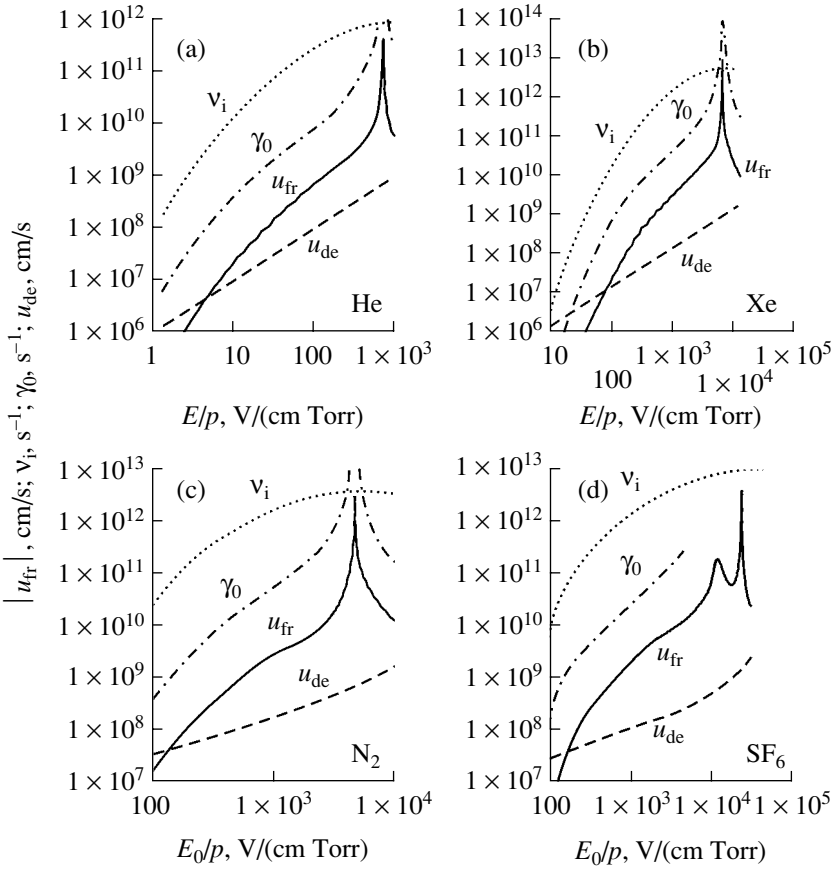

Fig. 1. Plots of the perturbation growth rate γ_0, modulus of the ionization front velocity u_{fr}, the electron drift velocity u_{de}, and the ionization rate ν_i versus reduced field strength E_0/p for (a) helium, (b) xenon, (c) nitrogen, and (d) sulfur hexafluoride calculated for $p = 1$ bar, Ln = 18.4, and $r_0 = 0.1$ cm.

electron multiplication wave, the transverse size of the inhomogeneity is also limited by the distance between particles at the background electron density ($\sim N_0^{-1/3} \sim 10^{-2}$ cm). It should be noted that it is possible in principle to obtain a spark channel in the form of a bundle consisting of many thin threads.

Criterion of streamer formation. A criterion for the transition from avalanche to streamer propagation is usually formulated as $\alpha_i d > 20$, where d is the distance between flat electrodes. This condition implies that the number of electrons formed in the avalanche is large enough to provide for a sufficiently high strength of the electric field at the avalanche head.

Evidently, this condition (at least, in the case of background ionization) is insufficient. In fact, the volume multiplication of electrons may take place before the spark channel will close the electrodes. An adequate criterion determining the transition from a volume discharge to the spark breakdown can be formulated as

$$\frac{u_{fr}(E_0)}{d} > \nu_i(E), \quad \text{or} \quad \frac{\nu_i(E_0) r_0}{\nu_i(E)\zeta(E_0) d} > 1,$$

where E is the field strength between the electrodes, which is significantly lower than the field strength E_0 at the streamer head.

Thus, if the field strength in the volume is high enough to ensure a fast volume multiplication of electrons, this time can be insufficient for the spark channel formation. Of course, the field in the volume should be also generated quite rapidly in order to eliminate the spark breakdown in the field buildup stage (this implies that the front of the voltage applied to the electrodes has to be sufficiently steep).

Conclusions. The electron multiplication wave front is unstable with respect to small perturbations in the form of protrusions and depressions. The perturbation growth rage is described by a function of the reduced field strength, which is universal for a given gas. The wave front instability leads, in particular, to streamer formation.

Acknowledgments. This study was supported by the International Scientific-Technological Center, grant no. 2706.

REFERENCES

1. S. I. Yakovlenko, Kratk. Soobshch. Fiz., No. 10, 27 (2003).
2. S. I. Yakovlenko, Kratk. Soobshch. Fiz., No. 2, 22 (2004).
3. S. I. Yakovlenko, Pis'ma Zh. Tekh. Fiz. **30** (9), 12 (2004) [Tech. Phys. Lett. **30**, 354 (2004)].
4. S. I. Yakovlenko, http://zhurnal.ape.relarn.ru/articles/2004/009.pdf.
5. S. I. Yakovlenko, Zh. Tekh. Fiz. **74** (9), 47 (2004) [Tech. Phys. **49**, 1150 (2004)].
6. É. D. Lozanskiĭ and O. B. Firsov, *Theory of Spark* (Atomizdat, Moscow, 1975) [in Russian].
7. V. F. Tarasenko and S. I. Yakovlenko, Usp. Fiz. Nauk **174**, 953 (2004) [Phys. Usp. **47**, 887 (2004)].
8. A. N. Tkachev and S. I. Yakovlenko, Cent. Eur. J. Phys. (CEJP) **2**, 579 (2004).
9. A. N. Tkachev and S. I. Yakovlenko, Pis'ma Zh. Éksp. Teor. Fiz. **77**, 264 (2003) [JETP Lett. **77**, 221 (2003)].
10. A. N. Tkachev and S. I. Yakovlenko, Pis'ma Zh. Tekh. Fiz. **29** (16), 54 (2003) [Tech. Phys. Lett. **29**, 683 (2003)].
11. A. M. Boichenko, A. N. Tkachev, and S. I. Yakovlenko, Pis'ma Zh. Éksp. Teor. Fiz. **78**, 1223 (2003) [JETP Lett. **78**, 709 (2003)].
12. A. N. Tkachev and S. I. Yakovlenko, Pis'ma Zh. Tekh. Fiz. **30** (7), 14 (2004) [Tech. Phys. Lett. **30**, 265 (2004)].

Translated by P. Pozdeev

Technical Physics Letters, Vol. 31, No. 2, 2005, pp. 173–175. Translated from Pis'ma v Zhurnal Tekhnicheskoĭ Fiziki, Vol. 31, No. 4, 2005, pp. 83–87.

Using Axisymmetric Potential in Modeling Crystal Growth from Melt

E. A. Shunikov*, Yu. P. Khukhryansky, and I. N. Arsent'ev

Voronezh State Technical University, Voronezh, 394026 Russia

Ioffe Physicotechnical Institute, Russian Academy of Sciences, St. Petersburg, 194021 Russia

** e-mail: eu_sh@mail.ru; dmitry.vinokurov@pop.ioffe.ru*

Received August 2, 2004

Abstract—A model describing the growth of $A^{III}A^{V}$ semiconductor compounds from a melt has been developed based on an axisymmetric potential of pair interaction between atoms in the growing crystal and in the melt. Numerical experiments performed according to the proposed model allowed the density of the flux of atoms deposited onto the crystal surface at the initial growth stage to be determined. © *2005 Pleiades Publishing, Inc.*

The growth of semiconductor single crystals with preset properties from melt is the main task of modern materials science for solid state microelectronics. Solving this problem requires knowledge of the function describing the interatomic interaction, which serves a base for constructing a model of the semiconductor crystal growth from the liquid phase.

In this Letter, we describe a new type of interaction potential, which takes into account some special features of the atomic arrangement in the liquid phase at the crystal surface. The proposed potential was used within the framework of the molecular dynamics simulation of the growth of a single crystal from melt. In particular, we simulated the growth of a gallium phosphide single crystal from a solution of phosphorus in gallium melt.

According to the proposed approach, the interaction of atoms in solution is described in terms of spherically symmetric Lennard-Jones and Born–Meyer potentials. In particular, the Ga–P interaction was described as

$$V(r) = \frac{D}{n-m}\left[m\left(\frac{r_0}{r}\right)^n - n\left(\frac{r_0}{r}\right)^m\right] + A_{BM}\exp\left(\frac{-r}{a}\right), \quad (1)$$

and the Ga–Ga and P–P interactions were described as

$$V(r) = A_{BM}\exp\left(\frac{-r}{a}\right), \quad (2)$$

where $r = \sqrt{x^2 + y^2 + z^2}$ and D, n, m, r_0, a, and A_{BM} are constant parameters [1].

Potentials (1) and (2) describe well the interatomic interactions in solution [2, 3], since this medium can be considered completely isotropic. However, these potentials are not as adequate for describing the interactions of atoms occurring in solution with atoms of the crystal because the potential of a particle at the liquid–solid interface is not spherically symmetric. For this reason, we suggest describing the interactions of atoms occurring in solution with atoms on the crystal (substrate) surface in terms of the axisymmetric potential

$$V(r) = 3.5\cos\left(\frac{8r}{a}\right)\exp\left(-\frac{16r^2}{a^2}\right)\exp\left(-\frac{(z-a)^2}{a^2}\right), \quad (3)$$

where $r = \sqrt{x^2 + y^2}$.

The proposed potential (3) is characterized by different numbers of extrema in various directions (Fig. 1), which allows the interaction of atoms occurring in solution with atoms of the substrate to be described more adequately. Another feature of potential (3) is the presence of a small maximum at $r \neq 0$. This maximum represents a part of the toroidal surface characterizing the activation energy of diffusion for phosphorus atoms on the crystal surface. The parameters of the potential were selected so that the calculated density of the flux of atoms deposited onto the crystal surface would agree with experimental data available for the same system supercooled by 50 K relative to the temperature of liquidus.

The main goal of this study was to determine the influence of the proposed axisymmetric potential on the mechanism of crystal growth from melt. From the standpoint of molecular dynamics, two main mechanisms are the deposition of separate atoms and the cluster growth, whereby groups (clusters) of atoms arrive at the substrate surface.

1063-7850/05/3102-0173$26.00 © 2005 Pleiades Publishing, Inc.

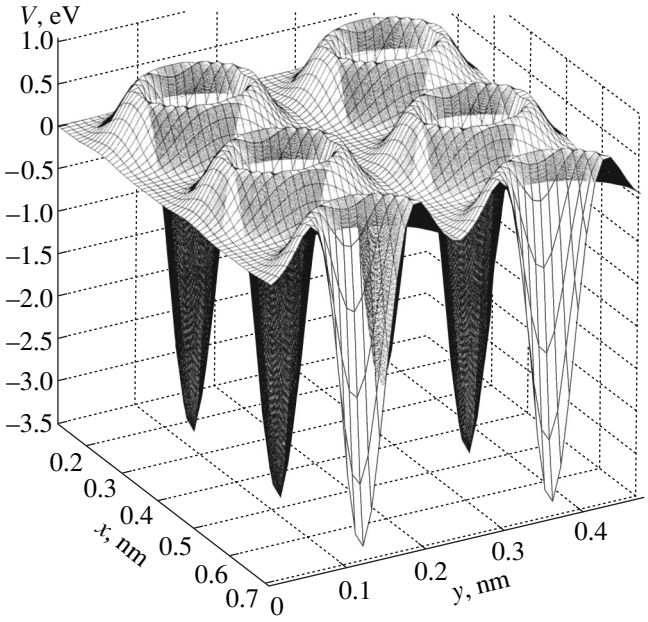

Fig. 1. The shape of the proposed axisymmetric potential at the melt–crystal interface.

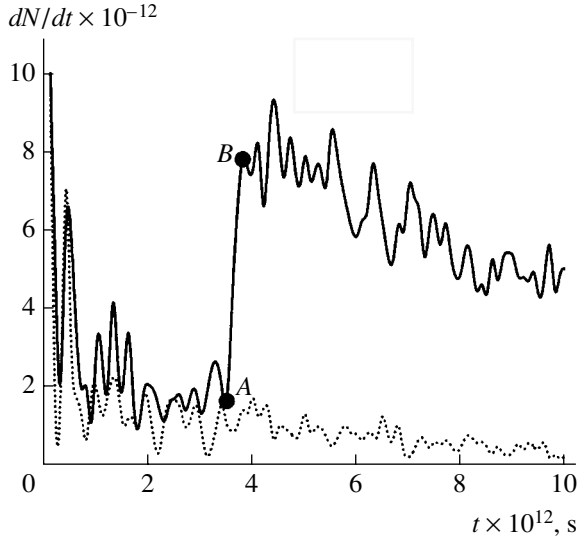

Fig. 2. Crystal growth kinetics for the bulk phosphorus concentrations x_P = 0.0667 (solid curve) and 0.0125 (dotted curve) at the initial stage of the transition process at $\Delta T = 0$.

The numerical experiments (computer simulations) were performed for various bulk concentrations of phosphorus in the melt: x_P = 0.0125, 0.025, 0.067, and 0.1 (molar fraction). The liquidus temperature was determined from the relation [4–6]

$$x(T) = \exp\left(-\frac{15992}{T} + 8.67\right), \qquad (4)$$

where $x(T)$ is the molar fraction of phosphorus in gallium melt at a given temperature T.

The results of computer simulations using proposed potential (3) and relation (4) confirmed that, in agreement with the behavior expected at the temperature of liquidus, the growth rate (defined as the difference between the rate of deposition from melt and the rate of crystal dissolution) is zero. Once this condition was satisfied, we concentrated on determining the time variation of the flux density of atoms deposited from melt onto the substrate surface for a period of time within 10^{-11} s.

The numerical experiments showed that variation of the bulk concentration of phosphorus in the melt, x_P, leads to a change in the mechanism of phosphorus deposition onto the substrate surface. For x_P in the interval from 0.025 to 0.066, the flux density kinetics of atoms deposited from melt onto the substrate surface, $dN/dt = j(t, x_P)$, exhibits a jump (Fig. 2, region *AB*) followed by a relatively smooth average decrease of $j(t)$ with time. This is explained by the onset of deposition of atomic groups (clusters). As the bulk concentration of phosphorus in solution decreases (Fig. 2, x_P = 0.0125), the mechanism changes and the deposition of phosphorus atoms proceeds predominantly in the form of separate atoms.

The situation does not qualitatively change upon a decrease in the temperature: the flux density somewhat increases, but the mechanism of deposition remains the same.

An increase in the bulk concentration of phosphorus in the melt is accompanied by the growth in both number and size of the clusters. As x_P increases to 0.1, the flux density of deposited atoms decreases, which implies that this phosphorus concentration corresponds to the predominant formation of small-size stoichiometric clusters. Therefore, phosphorus in gallium melt at $x_P \approx 0.1$ probably occurs in the form of separate atoms and P_2 molecules, the latter not entering into clusters with gallium. In solution, it is energetically more favorable to form nonstoichiometric clusters, since clusters of the maximum size were observed at small phosphorus concentrations. It should be also noted that, in the case of small phosphorus concentrations, the maximum of the cluster distribution profile was observed at a greater distance from the substrate than in the case of large concentrations. This is related to the fact that the substrate potential hinders the formation of nonstoichiometric clusters.

Computer simulations revealed an increase in the concentration of phosphorus atoms at the interface, which could be interpreted as the formation of a δ layer. This was confirmed by an increase in the concentration of clusters near the interface as compared to that in the bulk.

Using the results of calculations, we have also estimated the coefficients of diffusion for both clusters and

atoms, which have proved to be 1.5×10^{-10} m^2/s and 8.5×10^{-5} m^2/s, respectively.

Thus, using the proposed model involving an axisymmetric potential, it is possible to describe the growth of crystals from melt and to study the structure of a transition layer in the liquid phase for a period of time within ~10^{-11} s.

REFERENCES

1. W. Eckstein, *Computer Simulation of Ion–Solid Interactions* (Springer-Verlag, Berlin, 1991).
2. G.-P. Ostermeyer and V. L. Popov, Pis'ma Zh. Tekh. Fiz. **26** (6), 59 (2000) [Tech. Phys. Lett. **26**, 250 (2000)].
3. V. A. Polukhin, V. F. Ukhov, and M. M. Dzugutov, *Computer Simulation of Dynamics and Structure of Liquid Metals* (Nauka, Moscow, 1981) [in Russian].
4. M. Ilegems, M. B. Panish, and J. R. Arthur, J. Chem. Thermodyn. **6**, 157 (1974).
5. M. B. Panish, J. Cryst. Growth **27**, 6 (1974).
6. C. D. Thurmond, J. Phys. Chem. Solids **26**, 785 (1965).

Translated by P. Pozdeev

Technical Physics Letters, Vol. 31, No. 2, 2005, pp. 176–178. Translated from Pis'ma v Zhurnal Tekhnicheskoĭ Fiziki, Vol. 31, No. 4, 2005, pp. 88–94.

Magnetization and Critical Current of High-Temperature Superconductors with Artificial Pinning Centers

I. A. Rudnev*, B. P. Mikhailov, and P. V. Bobin

Moscow Engineering Physics Institute (State University), Moscow, 115409 Russia
Baikov Institute of Metallurgy and Materials Science, Russian Academy of Sciences, Moscow, 117334 Russia
** e-mail: rudnev@supercon.mephi.ru*

Received June 28, 2004

Abstract—We present new data on magnetization at $T = 4.2$ and 77 K for polycrystalline high-temperature superconductors of the $Bi_2Sr_2Ca_2Cu_3O_{10+\delta}$ system containing various amounts of nanodimensional inclusions of tantalum carbide, niobium carbide, or niobium nitride. The introduction of these nanoparticles (≤30 nm in size) leads to an increase in the magnetization and the critical current density. It is established for the first time that the dependence of the normalized critical current on the bulk concentration of indicated dopants is described by the same universal curve. The interval of the optimum dopant concentrations is found, in which the additives lead to the maximum increase in the critical current density. © *2005 Pleiades Publishing, Inc.*

The use of high-temperature superconductors (HTSCs) in power engineering, transport, technical physics, and the mining industry requires the development of long wiring conductors. Such wires must possess a high critical current density J_c, which requires the presence of either natural or artificial centers ensuring the effective pinning of magnetic flux in the conductor. Traditional methods of creating artificial pinning centers, such as irradiation with high-energy ions or neutrons, are (despite certain progress) still rather complicated and expensive. Radiation treatment of HTSC materials cannot be implemented on a commercial scale. Evidently, some other, relatively simple physicochemical methods capable of creating effective pinning centers in superconducting materials have to be developed.

One possible approach to the creation of additional pinning centers and improvement of the transport characteristics of HTSCs, which is most promising from a technological standpoint, is based on the introduction of nanoparticles of special inorganic additives (dopants) that are inert with respect to the superconducting matrix. These additives, introduced at the stage of HTSC material synthesis, have to be selected so that, on the one hand, they do not reduce the critical temperature of the initial superconductor and, on other hand, they provide effective pinning of the magnetic flux. There were attempts to dope HTSCs with nanodimensional inclusions of magnesium oxide [1, 2], carbides of niobium, tantalum, titanium, and silicon [3–6], and hafnium nitride [7]. The results of these investigations showed that doping with such additives makes it possible to increase the critical current density of HTSCs based on $(Bi,Pb)_2Sr_2CaCu_2O_{8+x}$ (Bi2212) and $(Bi,Pb)_2Sr_2Ca_2Cu_3O_{10+x}$ (Bi2223) compositions [3–7].

This Letter presents new original data on a significant increase in the magnetization of polycrystalline HTSCs at both helium ($T = 4.2$ K) and nitrogen (77 K) temperatures produced by nanoparticles of tantalum carbide, niobium carbide, or niobium nitride. The observed increase in the magnetization M means, according to the critical state model [8], an increase in the critical current density and implies the formation of effective artificial pinning centers in the doped material.

The initial Bi2223 compound was synthesized by method of carbonate coprecipitation using analytical-grade Bi_2O_3, CuO, CaO, Sr_2O_3, and Pb_2O_3 components. According to the X-ray diffraction data, the synthesized powder contained predominantly a 2223 phase (90 vol %) with small fractions of 2212 (5–10 vol %) and 2201 (2–3 vol %) phases and traces of $PbCaO_4$. The artificial pinning centers in the base matrix were created by introducing finely dispersed niobium nitride (NbN), tantalum carbide (TaC), and niobium carbide (NbC) powders with a characteristic particle size within 10–30 nm. The weight fractions of additives were varied from 0.05 to 0.2%. A mixture of the 2223 phase and nanoparticles was stirred for 30 h in a rotating vessel and then cold pressed into disks with a diameter of D = 10–12 mm and a height of h = 2–3 mm. The molding pressure in all cases was the same (100 kgf/cm^2). Then, all samples of various compositions (including control samples without additives) were simultaneously sintered for 10 h at 840°C. Upon sintering, the ceramic composites were studied by X-ray diffraction on a DRON-4 diffractometer using CuK_α radiation. All dif-

1063-7850/05/3102-0176$26.00

fraction lines in the diffractograms were assigned to known phases of the Bi–Sr–Ca–Cu–O system.

The magnetization measurements were performed by the Hall magnetometry method using two semiconductor Hall transducers counter-connected to the Hall potential leads. The first transducer (situated far from a sample) measured the external magnetic field H, while the other transducer (positioned at the sample surface) measured the magnetic induction. The differential signal obtained upon instrumental subtraction of the output signals of Hall transducers corresponded to the sample magnetization $M(H)$. The measurements were performed at liquid nitrogen (T = 77 K) and helium (4.2 K) temperatures. In the former case, the external magnetic field was generated by a copper solenoid; in the latter case, the field was generated by a superconducting NbTi solenoid.

Figure 1 shows the characteristic magnetization curves $M(H)$ measured at T = 4.2 K for the samples of Bi2223 ceramics containing NbC nanoparticles in various concentrations C = 0 (undoped control), 0.05, 0.1, and 0.2 wt %. As can be seen, the introduction of this additive leads to an increase in the sample magnetization in the entire range of magnetic fields studied. An increase in the width ΔM of the magnetization loop is indicative, according to the critical state model [8], of an increase in the critical current density. The width of the magnetization curve was defined as $\Delta M(H_0) = M_+(H_0) - M_-(H_0)$, where $M_+(H_0)$ and $M_-(H_0)$ are the values of magnetization measured in the field increase and decrease modes, respectively. Analogous results were obtained for the Bi2223 ceramics with NbN and TaC additives (see table). The critical current densities presented in the table were calculated using the formula $J_c(H_0) = 15\Delta M(H_0)/R$, which takes into account the demagnetizing factor and the field dependence of the critical current [9].

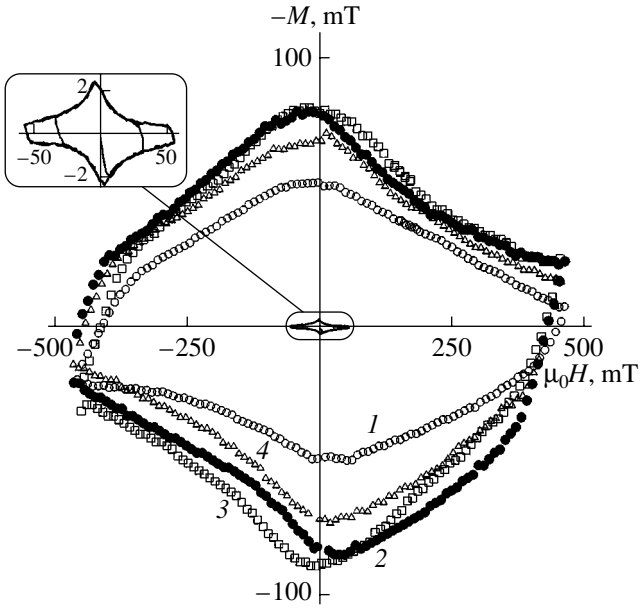

Fig. 1. Magnetization $M(H)$ (T = 4.2 K) of polycrystalline Bi2223 ceramics with various weight fractions of NbC nanoparticles: (*1*) undoped; (*2*) Bi2223 + 0.05 wt % NbC; (*3*) Bi2223 + 0.1 wt % NbC; (*4*) Bi2223 + 0.2 wt % NbC. Solid curve and the inset show the $M(H)$ curve measured for the undoped sample at T = 77 K.

As the temperature increases to T = 77 K, the shape of the magnetization curve changes and the $\Delta M(H_0)$ value sharply decreases. In order to illustrate the drop in magnetization caused by the increase in the temperature, Fig. 1 shows the data obtained at T = 4.2 K in comparison to the $M(H)$ curve measured at T = 77 K for

Characteristics of $Bi_2Sr_2Ca_2Cu_3O_{10+\delta}$ ceramic samples containing various amounts of additives in the form of nanodimensional inclusions

Additive	Weight fraction, %	Volume concentration, 10^{13} cm^{-3}	Sample size ($h \times D$), mm	J_c, A/cm^2			
				T = 77 K		T = 4.2 K	
				H = 0	H = 40 mT	H = 0	H = 440 mT
NbC	0.05	4.97	2 × 10	1440	345	38800	4400
NbC	0.2	19.9	2 × 10	1110	250	33600	4600
NbC	0.1	9.93	2 × 10	1430	380	40100	3100
TaC	0.05	2.76	2 × 10	1710	470	40700	2700
TaC	0.2	11	2 × 10	1780	540	41500	3000
TaC	0.1	5.52	2 × 10	1720	510	43900	2700
NbN	0.05	3.83	2 × 12	880	260	33600	4500
NbN	0.1	7.41	2 × 12	940	270	35200	2000
NbN	0.2	15	2 × 12	1210	355	32300	3100
–	–	–	2 × 12	870	176	19800	2700

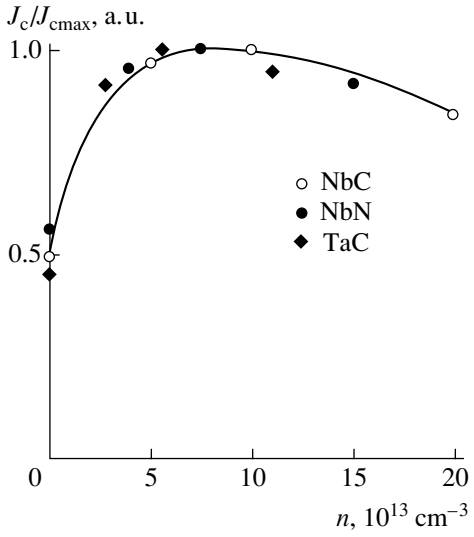

Fig. 2. Plot of the normalized critical current density at T = 4.2 K versus volume concentration of nanoparticles of various additives.

the undoped sample. It should be noted, however, that the introduction of nanoparticles leads to a significant increase in J_c both at 4.2 K and at liquid nitrogen temperature (see table).

The observed increase in magnetization implies that the introduced additives lead to the appearance of additional structural defects that play the role of artificial pinning centers. In order to optimize the dopant concentration so as to provide for the maximum increase in the critical current, it is necessary to analyze the dependence of J_c on the volume concentration n of impurities (i.e., on the number of pinning centers per unit volume), rather than on their weight fraction. Although the weight fractions of various additives were changed within the same limits (0.05–0.2 wt %), the volume concentrations of impurities (even for the same degree of dispersion or the average particle size) significantly varied because of the different densities of dopants. The volume concentrations of nanoparticles were calculated assuming that the characteristic size of particles was 20 nm and their densities were $\rho \approx 8.4$ g/cm^3 (NbN), 8.0 g/cm^3 (NbC), and 14.4 g/cm^3 (TaC) [10].

Figure 2 shows a plot of the critical current density at T = 4.2 K (normalized to the maximum value) versus volume concentration of nanoparticles (pinning centers) for various dopants. As can be seen, the curve has a universal domelike shape with a maximum in the vicinity of $n \approx (6–7) \times 10^{13}$ cm^{-3}.

Thus, the results of magnetization measurements for the samples of polycrystalline Bi2223-based HTSC doped with various amounts of nanoparticles of tantalum carbide, niobium carbide, or niobium nitride showed for the first time that these additives lead to a significant increase in the magnetization, which, in turn, implies an increase in the critical current. The most pronounced increase in the critical current density was observed for the samples doped with TaC. In a zero field, the growth in J_c was 120% at T = 4.2 K and 100% at 77 K. The maximum increase in J_c (290%) was observed at T = 77 K in a magnetic field of 40 mT. An analysis of the curve of the normalized critical current density versus the volume concentration of nanoparticles shows that this relation is described by a universal curve $J_c(n)$ with a maximum in the vicinity of the optimum concentration of nanodimensional inclusions, $n_{op} \approx (6–7) \times 10^{13}$ cm^{-3}. Using this universal curve, it is possible to predict the optimum weight fractions of the nanodimensional inclusions of other dopants with a given density and degree of dispersion (particle size). The whole body of experimental data provides convincing evidence for the possibility of increasing J_c of bismuth-containing HTSCs by introducing nanoparticles. The prospects for further increase in the magnetization and critical current density of HTSCs are related to a decrease in the characteristic size of nanoparticles to a level comparable with the coherence length (ξ = 0.2–0.7 nm).

Acknowledgments. This study was supported by the program "Directed Synthesis of Substances and Related Functional Materials with Preset Properties" of the Russian Academy of Sciences, the Ministry of Science and Education of the Russian Federation (project no. 40.012.1.1.1357) and the Federal Program "Integration" (project B0048).

REFERENCES

1. V. V. Lennikov, P. E. Kazin, V. I. Putlyaev, *et al.*, Zh. Neorg. Khim. **41**, 911 (1996).
2. W. Wey, J. S. Schwartz, K. S. Correta, *et al.*, Physica C **298**, 279 (1998).
3. B. P. Mikhailov, P. E. Kazin, V. V. Lennikov, *et al.*, Neorg. Mater. **37**, 753 (2001).
4. B. P. Mikhailov, G. S. Burkhanov, P. E. Kazin, *et al.*, Neorg. Mater. **37**, 1199 (2001).
5. B. P. Mikhailov, N. F. Tazetdinova, G. M. Leitus, *et al.*, J. Low Temp. Phys. **105**, 1553 (1996).
6. Y. C. Caj, Y. Tanaca, T. Curoda, *et al.*, Physica C **311**, 65 (1999).
7. B. P. Mikhailov, G. S. Burkhanov, P. E. Kazin, *et al.*, Neorg. Mater. **39**, 462 (2003).
8. C. P. Bean, Phys. Rev. Lett. **6**, 250 (1962); Rev. Mod. Phys. **36**, 31 (1964).
9. A. V. Kuznetsov, D. V. Eremenko, and V. N. Trofimov, Phys. Rev. B **56**, 9064 (1997).
10. *Handbook of Physical Quantities*, Ed. by I. S. Grigoriev and E. Z. Meĭlikhov (Énergoatomizdat, Moscow, 1991; CRC Press, Boca Raton, 1997).

Translated by P. Pozdeev

Technical Physics Letters, Vol. 31, No. 2, 2005, pp. 89–90. Translated from Pis'ma v Zhurnal Tekhnicheskoĭ Fiziki, Vol. 31, No. 3, 2005, pp. 1–4.

Entropy of Localized Plastic Strain Waves

L. B. Zuev

Institute of Strength Physics and Materials Science, Siberian Division, Russian Academy of Sciences, Tomsk, 634055 Russia

e-mail: levzuev@mail.tomsknet.ru

Received July 15, 2004

Abstract—Variations of the entropy in the course of generation and propagation of localized plastic strain waves in a solid is considered. It is shown that the formation of such waves leads to a decrease in the entropy, which gives ground to classify the localized plastic straining in solids as a self-organization process. © *2005 Pleiades Publishing, Inc.*

It has been established previously [1–3] that localization of plastic strain is a general property of all media and can be characterized by a macroscopic scale expressed in terms of the wavelength λ. Quantitative characteristics of this autowave process in the linear stage of strain hardening are as follows. The wave propagation velocity V_{aw} is inversely proportional to the strain hardening coefficient θ: $V_{aw} \sim 1/\theta$, where $\theta = d\sigma/d\varepsilon$; σ is the stress, and ε is the strain. The wave frequency ω obeys a quadratic dispersion law, $\omega(k) = \vartheta(k - k_0)^2 + \omega_0$, which is apparently equivalent to the relation $\omega = 1 + k^2$ known in nonlinear mechanics [4]. In the stage of prefracture, where $\sigma = \varepsilon^n$, the velocity of the fracture nuclei is proportional to the square of the parabolicity exponent n: $V_{aw} = V^*(n - q)^2$. The wavelength λ of localized plastic straining depends on the grain size D and the sample size L, as described by the relations $\lambda = \dfrac{\lambda_0}{1 + C\exp(-aD)}$ and $\lambda \sim \ln L$.

For the observed wave processes, the above parameters fall within the following limits: 3 mm $\le \lambda \le$ 20 mm, 10^{-5} m/s $\le V_{aw} \le 10^{-4}$ m/s, and 3×10^{-5} Hz $\le \omega \le 2 \times 10^{-3}$ Hz.

Wave processes involved in the plastic straining of solids have been known for a long time and described in detail [5, 6]. However, the propagation velocity as a function of the strain hardening coefficient for the plasticity waves has the form $V_{pw} \sim \theta^{1/2}$ [5], which substantially differs from the above relation for the localized strain wave, $V_{pw} \sim \theta^{-1}$. The basic character of this difference suggests that the localized plastic strain waves (autowaves [1–3]) revealed in our experiments represent wave processes of a new type. The existence of such waves was theoretically predicted by Aifantis [7]; a close approach has been developed by Naimark [8, 9].

The difference between $V_w(\theta)$ functions for strain waves of the two types leads to another divergence in the behavior of these wave processes. It is natural to assume that the strain rate during the plastic flow is proportional to the wave velocity, $\dot{\varepsilon} \sim V_w$. On the other hand, $\dot{\varepsilon} = b\rho_m V_{disl}$, where ρ_m and V_{disl} are the density and velocity of mobile dislocations, respectively, and b is the Burgers vector; therefore, $\dot{\varepsilon} \sim V_w$. In the general case, the velocity of dislocations in the region of thermoactivated straining is determined by the relation $V_{disl} \sim \exp(-G/k_B T)$ [10], where $G = U - TS + A$, U is the internal energy, S is the process entropy, A is the mechanical work, k_B is the Boltzmann constant, and T is the absolute temperature. In the case of plastic straining, $A = -\gamma\sigma$, where γ is the activation volume. Using the above relations, the strain rate can be expressed as

$$\dot{\varepsilon} \sim V_w \sim V_{disl} \sim \varepsilon_0 \exp\left(\frac{S}{k_B}\right)\exp\left(-\frac{U - \gamma\sigma}{k_B T}\right). \qquad (1)$$

For $(U - \gamma\sigma)/k_B T \approx$ const, we have $\ln V_w \sim S$.

The velocity of the localized strain wave was determined at the stage of easy glide in single crystals and at the stage of linear strain hardening in single crystals and polycrystalline samples of various metals and alloys [1–3]. This was done as described in [3], by studying variation of the position of the strain localization nucleus along the sample with time and by calculating the slope of this curve. The velocity of the plasticity wave was calculated as $V_{pw} \approx \sqrt{\theta/\rho_0}$ [5], where ρ_0 is the material density. These calculations were performed using the published values of densities and the θ values determined from the $\sigma(\varepsilon)$ curves.

The curves of $V_w(\theta)$ for the waves of the two types, which are plotted in logarithmic coordinates in the figure, are obviously equivalent to the $S(\theta)$ curves for these wave processes. In the case of plasticity waves (straight line *3*), the entropy exhibits an increase ($\Delta S > 0$) that is characteristic of all processes with energy dissipation. On the contrary, a decrease in the

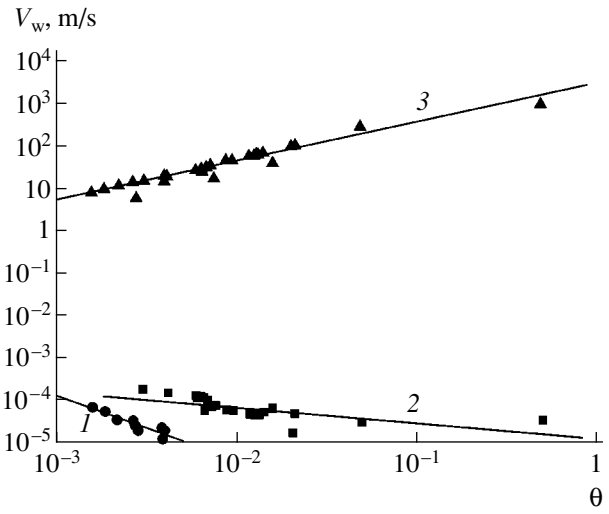

Plots of the velocities V_w of (*1*, *2*) the localized strain waves at the easy glide and linear strain hardening stages, respectively, and (*3*) the plasticity waves versus the strain hardening coefficient θ for various crystalline materials.

entropy ($\Delta S < 0$) observed for the localized strain waves (straight lines *1* and *2* for the easy glide and linear strain hardening stages, respectively) can be considered [11] a typical sign of self-ordering processes in deformable media.

As is known [12], the entropy of a system is determined by the degree of ordering, which is measured by the so-called order parameter. In application to the plastic strain localization waves, we have $S \sim \ln\theta$. Therefore, there are grounds to believe that the strain hardening coefficient plays the role of an order parameter in the process of plastic flow.

REFERENCES

1. L. B. Zuev, V. I. Danilov, and V. V. Gorbatenko, Zh. Tekh. Fiz. **65** (5), 91 (1995) [Tech. Phys. **40**, 456 (1995)].
2. L. B. Zuev, Ann. Phys. **10**, 965 (2001).
3. L. B. Zuev, V. I. Danilov, and B. S. Semukhin, Usp. Fiz. Metal. **3**, 237 (2002).
4. A. M. Kosevich and A. S. Kovalev, *Introduction to Nonlinear Physical Mechanics* (Naukova Dumka, Kiev, 1989) [in Russian].
5. H. Kolsky, *Stress Waves in Solids* (Dover, New York, 2003).
6. L. M. Shestopalov, *Straining of Metals and the Waves of Plasticity in Them* (Akad. Nauk SSSR, Moscow, 1958) [in Russian].
7. E. C. Aifantis, Int. J. Non-Linear Mech. **31**, 797 (1996).
8. O. Naimark and M. Davydova, J. Phys. IV (France) **6**, 259 (1996).
9. O. B. Naimark, Pis'ma Zh. Tekh. Fiz. **23** (13), 81 (1997) [Tech. Phys. Lett. **23**, 529 (1997)].
10. V. L. Indenbom, A. N. Orlov, and Yu. Estrin, in *Elementary Processes of Plastic Deformation of Crystals*, Ed. by V. I. Startsev (Naukova Dumka, Kiev, 1978), pp. 93–112 [in Russian].
11. H. Haken, *Information and Self-Organization* (Springer-Verlag, Heidelberg, 1988).
12. R. M. White and T. H. Geballe, *Long-Range Order in Solids* (Academic, New York, 1979).

Translated by P. Pozdeev

Technical Physics Letters, Vol. 31, No. 2, 2005, pp. 91–93. Translated from Pis'ma v Zhurnal Tekhnicheskoĭ Fiziki, Vol. 31, No. 3, 2005, pp. 5–10.

Transmutation Isotope Diffusion in YBaCuO Ceramics

R. Sh. Malkovich

Ioffe Physicotechnical Institute, Russian Academy of Sciences, St. Petersburg, 194021 Russia
e-mail: malkovich@mail.ioffe.ru

Received June 7, 2004

Abstract—The diffusion of a transmutation isotope generated in YBaCuO ceramics irradiated by high-energy charged particles is mathematically analyzed. The model is based on the assumption that copper isotope atoms created in subsurface layers of ceramic grains segregate at the grain boundaries in the course of subsequent annealing and then rapidly diffuse via intergranular regions in depth of the material and penetrate into the bulk of grains. © *2005 Pleiades Publishing, Inc.*

Irradiation of a solid by high-energy charged particles leads to the generation of a radioactive transmutation isotope impurity [1]. This source of impurity atoms has been previously used [2] for the investigation of diffusion of a transmutation copper isotope in YBaCuO ceramics. However, the values of the diffusion coefficient determined using the Fick law turned out to be lower than those obtained in the case when the impurity was introduced by the traditional method from a layer of copper deposited onto the surface of ceramics.

This discrepancy was qualitatively explained within the framework of a model proposed in [2], according to which the transmutation isotope is generated predominantly inside the grains of ceramics. In the course of subsequent annealing, the impurity atoms segregate at the grain boundaries and then rapidly diffuse via intergranular regions in depth of the material and penetrate into the bulk of grains. In this process, a limiting stage is the slow diffusion in the grain bulk. In contrast, the impurity atoms diffusing from a layer deposited onto the sample surface enter directly into the intergranular regions, rapidly diffuse there, and penetrate into grains.

This Letter presents a mathematical analysis of the process of transmutation isotope diffusion in YBaCuO ceramics.

By analogy with the Fisher concept [3], let us consider a ceramic sample representing a semi-infinite medium occupying the half-space $x \geq 0$ and separated into two parts (grain bodies) by a thin intergranular region (interlayer) perpendicular to the $x = 0$ plane (Fig. 1). The speed of diffusion in this interlayer is assumed to be much higher than that in the grain. Atoms moving in the interlayer are also capable of entering into the body. Important assumptions are that (i) the rate of diffusion in the interlayer is very high and (ii) the interlayer thickness δ is very small. This implies that the gradient of impurity (diffusant) across this layer (e.g., in the y axis direction) is absent, the impurity concentration in the layer cross section is constant, and the process of diffusion in the interlayer has a one-dimensional character. Under these conditions, we can ignore the motion of impurity in the grain body in the x direction, so that diffusion in the grain is also a one-dimensional process in the y direction. We assume that the coefficients of diffusion in the grain (D) and in the interlayer (D_1) are constant, the Fick law is valid in both media, and the grain–interlayer boundary is immobile.

Using the above assumptions, we can write equations describing the diffusion of impurity atoms in the grain and interlayer and formulate the boundary condition at $y = 0$. Consider an element $b\delta dx$ in the interlayer volume and let $c(x, t)$ be the impurity concentration in this element. The impurity diffuses from this element into the adjacent grains, and there is also a reverse diffusion flux from these grains to the interlayer. Owing to a high rate of diffusion in the interlayer and a small value of δ, the impurity concentration in the entire cross section x of the element is constant. Then, the amount of impurity dQ_c passing during a period of time dt from the given volume element to the adjacent grain through

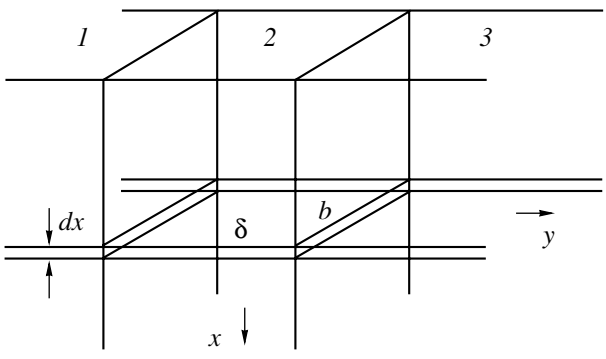

Fig. 1. Schematic diagram of the model of impurity diffusion in YbaCuO ceramics: (*1*, *3*) ceramic grains; (*2*) intergranular region (see the text for explanations).

1063-7850/05/3102-0091$26.00 © 2005 Pleiades Publishing, Inc.

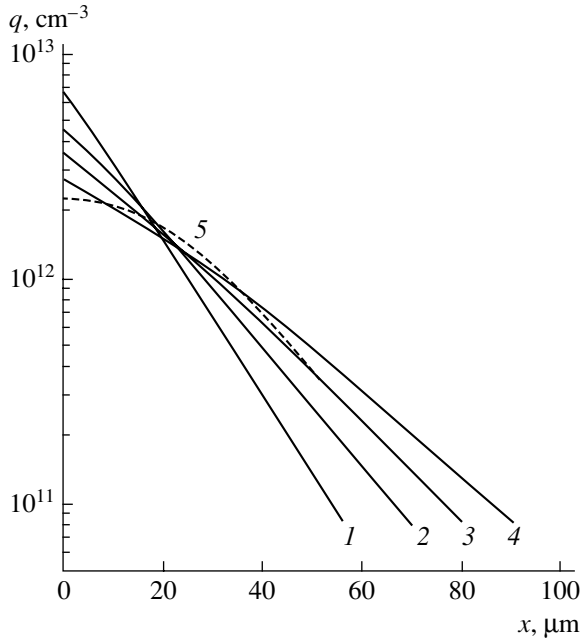

Fig. 2. The volume impurity concentration profiles in the ceramic grain: (*1*) initial distribution; (*2–4*) calculated model profiles for t = 2.75, 5.5, and 8.25 h, respectively ($D = 8 \times 10^{-13}$ cm^2/s, $D_1 = 3 \times 10^{-8}$ cm^2/s, g = 0.25, h = 0.4); (*5*) experimental diffusion profile of ^{64}Cu in YBaCuO ceramics.

a boundary area of bdx is proportional to the total content of impurity in the element,

$$dQ_c = gc(x, t)b\delta dxdt, \quad (1)$$

where g is a proportionality factor.

Further, the amount of impurity dQ_s passing during the same period of time dt from the adjacent grains to the interlayer through the same boundary area bdx is proportional to the impurity concentration in the grain $S(x, 0, t)$ in the cross section x at the boundary $y = 0$:

$$dQ_s = 2kS(x, 0, t)bdxdt, \quad (2)$$

where k is the corresponding proportionality factor.

A change dQ_D in the impurity content in the given element due to diffusion via the interlayer is

$$dQ_D = D_1\frac{\partial^2 c}{\partial x^2}b\delta dxdt. \quad (3)$$

Then, the total change dQ in the impurity content during the time dt in the volume element under consideration can be written as

$$dQ = dQ_D + dQ_s - dQ_c. \quad (4)$$

Taking into account that

$$dQ = dcb\delta dx \quad (5)$$

and using relations (1)–(5), we finally obtain the equation

$$\frac{\partial c}{\partial t} = D_1\frac{\partial^2 c}{\partial x^2} + hS(x, 0, t) - gc, \quad (6)$$

where $h = 2k/\delta$. This equation describes diffusion in the interlayer with allowance for both the impurity penetrating into grains and the reverse flux of impurity from grains into the interlayer.

The diffusion of impurity in the grain obeys the equation

$$\frac{\partial S}{\partial t} = D\frac{\partial^2 S}{\partial y^2}, \quad (7)$$

where $S = S(x, y, t)$ is the impurity concentration.

In order to formulate the boundary condition at the interlayer–grain interface $y = 0$, let us assume that there is a balance between the amounts of impurity supplied to and removed from this plane. The amount of impurity dQ_0 entering the interface area bdx from the grain body during a period of time dt is

$$dQ_0 = D\frac{\partial S}{\partial y}\bigg|_{y=0} bdxdt, \quad (8)$$

while the amount of impurity dQ_c coming to this area for the same time from the interlayer is given by relation (1). The amount of impurity dQ_{s1} leaving the plane $y = 0$ to enter the interlayer is given by an equation analogous to relation (2):

$$dQ_{s1} = kS(x, 0, t)bdxdt. \quad (9)$$

Writing the balance condition as

$$dQ_0 + dQ_c = dQ_{s1}, \quad (10)$$

we obtain the relation

$$-D\frac{\partial S}{\partial y} + kS(x, y, t) = g\delta c(x, t), \quad y = 0, \quad (11)$$

which is a generalized boundary condition [3] that takes into account both the diffusion of impurity from the interlayer to the grain and the reverse flux from the grain to the interlayer.

The other boundary conditions to be used in solving the system of Eqs. (6) and (7) are as follows:

$$\frac{\partial c}{\partial x} = 0, \quad x = 0, \quad \text{and} \quad x = \infty;$$
$$\frac{\partial S}{\partial y} = 0, \quad y = \infty. \quad (12)$$

Let us assume that the interlayer in the initial state is free from the impurity:

$$c(x, 0) = 0, \quad x \geq 0. \quad (13)$$

The initial condition for the grain corresponds to the copper transmutation isotope profile $S = S(x, y, 0)$ created in an YBaCuO ceramics by irradiation with high-energy deuterons [2]. It is assumed that, for $x = l$, we have $S(l, y, 0) = S_0(l) = \text{const}$.

Equations (6) and (7) with the boundary conditions (11) and (12) and the above initial conditions for the functions $c(x, t)$ and $S(x, y, t)$ have been solved by finite difference method. The results of numerical calculations gave the impurity concentrations in the grain, $S(x, y, t)$, and in the interlayer, $c(x, t)$. The total volume impurity concentration $q(x, t)$ in the cross section x of the grain was determined with neglect of the impurity content in the interlayer, since this layer thickness was negligibly small.

As can be seen from the calculated impurity profiles presented in Fig. 2, the volume concentration of impurity atoms in the source zone decreases with time, whereas their content in the bulk of the sample increases. The results of calculations (profile *4*) satisfactorily agree with the experimental data (curve *5*).

In conclusion, a mathematical analysis of the grain-boundary diffusion model has confirmed the assumption made previously [2], according to which a transmutation copper isotope created in the subsurface layer of YBaCuO ceramic grains segregates at the grain boundaries in the course of subsequent annealing and then rapidly diffuses via intergranular regions in depth of the material and penetrates into the bulk of grains.

Acknowledgments. The author is grateful to E.A. Skoryatina for valuable remarks.

REFERENCES

1. V. A. Didik, V. V. Kozlovskiĭ, R. Sh. Malkovich, *et al.*, Pis'ma Zh. Tekh. Fiz. **15** (12), 9 (1989) [Sov. Tech. Phys. Lett. **15**, 462 (1989)].
2. V. A. Didik, R. Sh. Malkovich, E. A. Skoryatina, *et al.*, Nucl. Instrum. Methods Phys. Res. B **160**, 387 (2000).
3. I. Kaur and W. Gust, *Fundamentals of Grain and Interphase Boundary Diffusion* (Ziegler, Stuttgart, 1989).
4. R. Sh. Malkovich, *Mathematics of Diffusion in Semiconductors* (Nauka, St. Petersburg, 1999) [in Russian].

Translated by P. Pozdeev

Technical Physics Letters, Vol. 31, No. 2, 2005, pp. 94–96. Translated from Pis'ma v Zhurnal Tekhnicheskoĭ Fiziki, Vol. 31, No. 3, 2005, pp. 11–17.

Spectral Dependence of the Optical Rectification Effect in Nanographite Films

G. M. Mikheev[a,*], R. G. Zonov[a], A. N. Obraztsov[b], A. P. Volkov[b], and Yu. P. Svirko[c]

[a] *Institute of Applied Mechanics, Ural Division, Russian Academy of Sciences, Izhevsk, Udmurtia, 426067 Russia*
[b] *Department of Physics, Moscow State University, Moscow, 119992 Russia*
[c] *Department of Physics, Joensuu University, Joensuu, Finland*
**e-mail: gmmikheev@udmnet.ru*

Received July 29, 2004

Abstract—The spectral dependence of the optical rectification effect in nanostructured carbon (nanographite) films obtained by plasmachemical deposition was studied in a wavelength range from 266 to 1900 nm. In this range, the amplitude of the electric signal observed when films were irradiated by nanosecond light pulses of constant power increases in inverse proportion to the laser wavelength. The experimental results confirm the assumptions made previously concerning the mechanism of the observed effect. It is suggested that nanographite films are promising materials for detectors of ultrashort laser pulses in the IR, visible, and UV spectral intervals and for generators of electromagnetic radiation operating in the terahertz frequency range. © *2005 Pleiades Publishing, Inc.*

When a high-power laser pulse propagates in a nonlinear optical crystal, a pulse of dielectric polarization with the shape repeating the laser pulse envelope can be induced in this crystal. If such a nonlinear optical crystal is placed between metal electrodes, the laser-induced polarization will lead to the appearance of a quasi-static (pulsed) voltage between these electrodes. The shape of the generated electric pulse reproduces the light pulse envelope. This phenomenon underlies the well-known optical rectification effect [1, 2]. Our recent publications [3, 4] reported on the optical rectification observed in nanostructured carbon (nanographite) films obtained by plasmachemical deposition [5, 6]. The electric voltage pulse, reproducing the nanosecond pulse generated by a Q-switched laser, was measured between metal electrodes pressed against a nanographite film on silicon substrate. The experimental results were explained in terms of a quadrupole contribution due to the quadratic static polarization component of the nonlinear medium.

It has been experimentally established that the voltage responsivity η of the optical rectification effect, defined as

$$\eta = U/P \quad (1)$$

(where U is the response voltage pulse amplitude and P is the laser pulse power), was different for a laser wavelength of 1064 and 532 nm. In order to elucidate the nature of the optical rectification effect in nanographite films and to provide information important for practical applications, we studied the spectral sensitivity of this effect in nanographite films in a broad wavelength range. This Letter presents the results of our investigation.

The experiments were performed on samples of plasmachemically deposited carbon films with a pronounced porous nanocrystalline graphite structure [3–6]. A nanographite film on silicon substrate was pressed with two flat conducting electrodes to a dielectric sample holder. The amplitude U of the response voltage appearing between the electrodes during laser irradiation of the film was measured using a storage oscilloscope with an input impedance of 1 MΩ, while the shape of the electric pulses could be observed using an oscilloscope with a pass band of 250 MHz and photographed by a digital camera. The sample films were exposed to the radiation of a single-mode single-frequency YAG:Nd^{3+} laser [7] generating pulses at λ = 1064 nm with a full width at half maximum (FWHM) of about 20 ns and a pulse power of 60 mJ. The laser beam diameter was 2 mm.

The pulses of radiation with other wavelengths were obtained using nonlinear optical converters (producing the second, third, and fourth harmonics of the fundamental laser mode) and a converter based on the stimulated Raman scattering effect in compressed hydrogen at a $Q_{01}(1)$ vibrational transition with a frequency shift of 4155 cm^{-1} [8]. The nonlinear optical converters were based on the KTP, DKDP, and BBO crystals and generated laser radiation with a frequency of 532, 354.7, and 266 nm, respectively. The Raman effect was excited by the first or second harmonic of the YAG:Nd^{3+} laser, which was focused by a lens with a focal distance of

1063-7850/05/3102-0094$26.00

F = 66 cm in a 86-cm-long cell with hydrogen at a pressure of P = 25 bar. In this way, it was possible to obtain sufficiently powerful pulses of the first Stokes component with a wavelength of 1907 or 683 nm. In accordance with the previous data [9], high-power radiation with λ = 683 nm was generated in both the forward and reverse directions. An important feature of this radiation, which was also used in our experiments, was a significant difference in shape of the pulses generated in the forward and reverse directions [10–12]. The Raman converter (F = 66 cm, L = 86 cm) with hydrogen at P = 3.5 bar pumped at 532 nm produced sufficiently powerful pulses of the first anti-Stokes component with a wavelength of 435.7 nm. The radiation with different wavelengths was spatially separated with the aid of a dispersive quartz prism. Thus, the main laser pulses with 1064 nm were converted into high-power pulses of radiation at six discrete wavelengths in various regions of the spectral range studied.

The voltage amplitude U of the optical rectification response signal for all spectral components was measured using the linearly (p) polarized radiation incident on the nanographite film surface at a fixed angle of 45°. The plane of incidence was perpendicular to the two parallel electrodes situated on the opposite ends of the film and spaced by about 20 mm. The power of the incident radiation was determined for each spectral component as $P = \varepsilon/\tau$, where ε is the laser pulse energy measured by the standard instrument and τ is the laser pulse width (FWHM). It should be emphasized that, as was established previously [3, 4], the shape of the response voltage pulse repeats the incident pulse shape. For this reason, the laser pulse duration at various wavelengths was determined using the shape of the response signal measured in nanographite films exposed to the corresponding spectral component. Then, the responsivity of a given film at various wavelengths was calculated using formula (1). The results were averaged over not less than 30 measurements at each wavelength.

Figure 1 shows the typical laser radiation waveforms measured for a nanographite film at (a) 1064, (b) 1907, and (c) 683 nm for the Stokes component in the forward direction, (d) 683 nm for the backward Stokes component, and (e) 266 nm. As can be seen from these data, the Stokes radiation pulses at 683 nm measured in the forward and reverse directions exhibit significantly different features, which is in good agreement with the well-known published results [10–12]. Thus, by measuring the optical rectification response signal in nanographite films, it is possible to study the laser pulse shapes in a broad spectral range.

Figure 2 shows a plot of the normalized voltage responsivity η/η_{1064} versus $1/\lambda$, where λ is the probing laser wavelength and η_{1064} is the voltage response measured at 1064 nm. As can be seen, the dependence of η/η_{1064} on $1/\lambda$ has a linear character, showing a monotonic decrease in the IR range and an increase in the UV range. Note that the extrapolated intercept of this plot

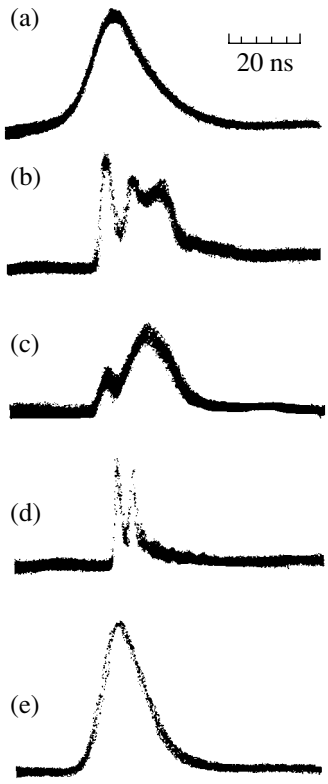

Fig. 1. Pulse waveforms: (a, e) first and fourth harmonics of the passive Q-switched YAG:Nd^{3+} laser; (b, c) the first Stokes components generated in the forward direction by a Raman converter excited by the first and second laser harmonics, respectively; (d) the first Stokes component generated in the reverse direction by the Raman converter excited by the second laser harmonic. The backward Raman effect converter was based on a vibrational transition in compressed hydrogen. The waveforms were measured as the response voltage due to the optical rectification effect in nanographite films. The amplitudes and positions of pulses are arbitrary.

with the ordinate axis gives a positive value, which implies that the responsivity of the given film in the far IR range may be nonzero. In this respect, photovoltaic converters based on the optical rectification effect in nanographite films substantially differ from the analogous photosensors based on Si, GaAs, GaP, and some other materials whose response in the IR range sharply drops to zero [13].

It was also of interest to compare the results of our experiments to theoretical conclusions derived previously [3], according to which the amplitude U of the pulsed response voltage related to the quadrupole contribution from the quadratic static polarization component of the nonlinear medium can be described as

$$U = -(4\pi S_0/\varepsilon L)\chi(\mathbf{E}\mathbf{E}^*)f(\alpha, \beta), \qquad (2)$$

where S_0 is the laser beam cross section area, $\mathbf{E}$ ($\mathbf{E}^*$) is the electric field vector, ε is the dc permittivity of the medium, L is the electrode length, $f(\alpha, \beta)$ is the func-

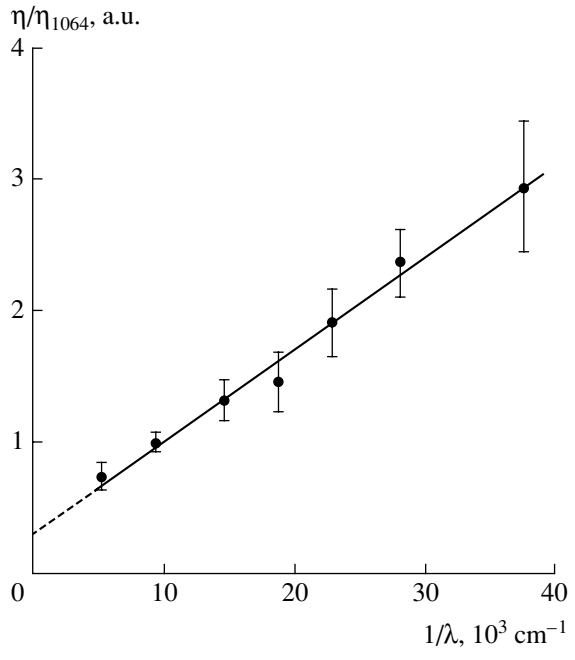

Fig. 2. An experimental plot of the normalized voltage responsivity η/η_{1064} versus $1/\lambda$ for a nanographite film exposed to nanosecond laser pulses. Dashed line shows extrapolation to the far IR range.

tion dependent on the spatial orientation of the film relative to the incident laser beam, $\chi = 2\mathrm{Re}\{2i\pi\chi_{xyyx}/\lambda\}$, λ is the laser radiation wavelength, and χ_{xyyx} is the component of the second-order nonlinear quadrupole susceptibility of the isotropic film in a rectangular coordinate system *XYZ* with the *OZ* axis directed along the normal to the film surface. If χ_{xyyx} is independent of the radiation wavelength, relation (2) leads to the direct proportionality of the optical rectification responsivity to $1/\lambda$ (i.e., to the exciting radiation frequency), in agreement with the experimental results presented above (Fig. 2). Formula (2) also suggests that the response signal must vanish at a zero frequency. However, extrapolation of the experimental plot to the region of low frequencies (Fig. 2) leads to a nonzero value of η. Apparently, a correct quantitative comparison of theoretical relation (2) to the experimental results is possible only provided that the spectral dependence of the susceptibility tensor component χ_{xyyx} is known. Nevertheless, we believe that, on the qualitative level, our experimental results are consistent with theoretical conclusions (except for the probable nonzero responsivity in the far IR range).

Thus, the results of our experimental investigation show that nanographite films can be used to convert nanosecond pulses of laser radiation in a broad spectral range into electric voltage pulses whose shape reproduces the laser pulse envelope. The coefficient of conversion of the laser pulse power in the response voltage increases in inverse proportion to the laser radiation wavelength. The experimental data are qualitatively consistent with a theory describing the optical rectification effect in terms of a quadrupole contribution due to the quadratic static polarization component of the nonlinear medium.

Acknowledgments. The authors are grateful to T.N. Mogileva for her help in performing the experiments.

This study was supported by the INTAS Foundation (grant no. 01-0254) and by the Russian Foundation for Basic Research (project no. 04-02-96011).

REFERENCES

1. J. F. Ward, Phys. Rev. **143**, 569 (1966).
2. B. N. Morozov and Yu. M. Aĭvazyan, Kvantovaya Élektron. (Moscow) **7**, 5 (1980).
3. G. N. Mikheev, R. G. Zonov, A. N. Obraztsov, and Yu. P. Svirko, Appl. Phys. Lett. **84**, 4854 (2004).
4. G. N. Mikheev, R. G. Zonov, A. N. Obraztsov, and Yu. P. Svirko, Pis'ma Zh. Tekh. Fiz. **30** (17), 88 (2004) [Tech. Phys. Lett. **30**, 750 (2004)].
5. A. N. Obraztsov, A. P. Volkov, A. I. Boronin, *et al.*, Zh. Éksp. Teor. Fiz. **120**, 970 (2001) [JETP **93**, 846 (2001)].
6. A. N. Obraztsov, A. A. Zolotukhin, A. O. Ustinov, *et al.*, Carbon **41**, 836 (2003).
7. G. M. Mikheev, D. I. Maleev, and T. N. Mogileva, Kvantovaya Élektron. (Moscow) **19**, 45 (1992).
8. B. P. Stoicheff, Can. J. Phys. **35**, 730 (1957).
9. G. M. Mikheev, Kvantovaya Élektron. (Moscow) **18**, 337 (1991).
10. M. Maier, W. Kaiser, and J. A. Giordmaine, Phys. Rev. **177**, 580 (1969).
11. R. R. Jacobs, J. Goldhar, D. Eimerl, *et al.*, Appl. Phys. Lett. **37**, 264 (1980).
12. G. Venkin, D. A. Esikov, D. I. Maleev, and G. M. Mikheev, Kvantovaya Élektron. (Moscow) **13**, 379 (1986).
13. M. Anisimova, I. M. Vikulin, F. A. Zaitov, and Sh. D. Kurmashev, *Semiconductor Photodetectors: Ultraviolet, Visible, and Near-Infrared Spectral Regions* (Radio i Svyaz', Moscow, 1984) [in Russian].

Translated by P. Pozdeev

Technical Physics Letters, Vol. 31, No. 2, 2005, pp. 97–100. Translated from Pis'ma v Zhurnal Tekhnicheskoĭ Fiziki, Vol. 31, No. 3, 2005, pp. 18–26.

Estimation of the Parameters of One-Dimensional Maps from Chaotic Time Series

D. A. Smirnov, V. S. Vlaskin, and V. I. Ponomarenko

Saratov Branch of the Institute of Radio Engineering and Electronics, Russian Academy of Sciences, Saratov, Russia

e-mail: sbire@sgu.ru

Received September 2, 2004

Abstract—The problem of constructing model maps based on the experimental chaotic time series is considered. A new method of estimation of the model parameters for one-dimensional maps is proposed, which employs a least squares procedure and calculations of the objective function using iterations of the model map in the reverse time. The results of a numerical experiment show that the proposed method provides much more accurate estimates than does the traditional approach at a moderate noise level below a certain threshold. The greater the number of parameters to be evaluated, the higher the threshold and, hence, the broader the domain of high efficiency of the new method. © *2005 Pleiades Publishing, Inc.*

Introduction. Besides their evident basic significance, methods intended for reconstructing the mathematical models of processes from the observable time series (i.e., a finite set of values of the observable η_1, …, η_N measured at sequential moments of time) have numerous applications, from the calculation of the characteristics of nonlinear elements of electrical circuits [1] to the description of biochemical processes in the living cell [2]. The task of modeling based on the time series is referred to as the "identification of systems" [3] or "reconstruction of dynamical systems" [4, 5]. At present, the approaches to solving this task are developed within the framework of nonlinear dynamics [1, 2, 6] and frequently employ maps [7–9], since even low-dimensional maps are capable of describing complicated dynamics encountered in various real systems. For example, the Poincaré maps of strongly dissipative nonlinear systems (such as the Lorentz and Rössler systems) are frequently one-dimensional with a high precision [10].

This study is devoted to this special case of modeling and is aimed at evaluating the parameters of a one-dimensional map from the corresponding time series. This problem has been repeatedly studied [11–15], and various methods for such estimation have been developed. Theoretically, the longer the time series (i.e., the greater N), the larger the possibility of obtaining highly precise estimates of the target parameters. However, the known methods encounter serious difficulties in practical implementation in the case of systems featuring chaotic regimes. We proposed a new method, which allows more accurate estimates to be obtained from long chaotic series for a not too high noise level. Our approach is based on the idea of iteration in the reverse time that was previously suggested for the processing of time series with nonlinear noise filtration [16] and for the separation of a sum of chaotic signals into components [17].

Formulation of the problem and description of the standard approach. Let us consider a one-dimensional map

$$x_{n+1} = f(x_n, \mathbf{a}), \tag{1}$$

where x is a dynamical variable and $\mathbf{a}$ is a P-dimensional vector of parameters. The time series is generated by map (1) in a chaotic regime for the parameters $\mathbf{a} = \mathbf{a}^{(0)}$ and the initial condition $x_1 = x_1^{(0)}$, and is assumed to be noisy as described by the variable $\eta_n = x_n + \xi_n$, where ξ_n is a sequence of independent random quantities distributed according to the normal law with a zero mean and a variance of σ_ξ^2. The form of function f is known, while the $\mathbf{a}^{(0)}$ and $x_1^{(0)}$ values are unknown and the task is to determine the estimates $\hat{\mathbf{a}}$ with maximum accuracy.

Theoretically, the most effective variant is provided by method of least squares, whereby x_1 and $\mathbf{a}$ are determined so as to make the realization of map (1) close to the observed time series, that is, to minimize the objective function

$$S(x_1, \mathbf{a}) = \sum_{n=0}^{N-1} (\eta_{n+1} - f^{(n)})(x_1, \mathbf{a})^2, \tag{2}$$

where $f^{(n)}$ is the nth iteration of the f map and

1063-7850/05/3102-0097$26.00

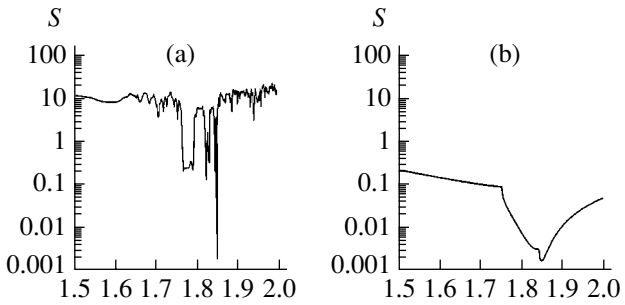

Fig. 1. Objective functions for the quadratic map (4) constructed at $N = 20$, $a^{(0)} = 1.85$, and $x_1^{(0)} = 0.3$: (a) for forward iterations, $x_1 = x_1^{(0)}$, function (2); (b) for backward iterations, $x_N = x_N^{(0)}$, function (3).

$f^{(0)}(x, \mathbf{a}) \equiv x$. However, this variant is effective only provided that the global minimum of function (2) can be found.[1]

In practice, the minimization procedure is performed using iterative methods [18], according to which the initial x_1 and $\mathbf{a}$ values are set by a starting guess followed by a descent to a minimum. However, finding a global minimum of objective function (2) in the case of long chaotic series is practically impossible because the number of local minima is very large [15] (an example of iteration for a time series of quite moderate length is presented in Fig. 1a). It is the starting guess that determines which minimum will be attained.

The usual practice it to try a large number M of starting guesses and then select the deepest minimum. Guesses are taken from a certain region presumably containing true values of the parameters to be determined. In particular, this region frequently represents a parallelepiped with the side lengths Δ_x (with respect to the initial condition) and Δ_i (with respect to the a_i values): these Δ_x and Δ_i values will be referred to below as the starting uncertainty intervals. However, the global minimum for a long chaotic series can be found only using an enormously large M or extremely small Δ_x and Δ_i such that can hardly be realized in practice. An acceptable approach consists in that certain practically "reasonable" values of M, Δ_x, and Δ_i are set and the initial series is divided into segments of length L, in which the global minimum (2) can be found within a reasonable time. The final "forward" estimate, obtained as an empirical mean of the values obtained for these segments, is denoted $\hat{\mathbf{a}}_f$. Estimates obtained in the short segments can be strongly biased, and then the forward estimate is significantly biased as well. This deviation is not eliminated on increasing the length N of the initial series. It is also senseless to increase L, since this will hinder determination of the global minimum of function (2). This is a basic limitation of the standard method.

Idea behind the new method. We suggest using the least squares procedure in combination with backward iteration of the model map in the reverse time, that is, to minimize the objective function

$$S(x_N, \mathbf{a}) = \sum_{n=0}^{N-1} (\eta_{N-n} - f^{(-n)})(x_N, \mathbf{a})^2, \qquad (3)$$

where $f^{(-n)}$ is the nth iteration of map (1) in the reverse time. For the time reversal, the Lyapunov exponent becomes negative and the sensitivity of the map trajectory with respect to the initial condition decreases. For this reason, we may expect that the number of local minima in the objective function of type (3) is not as large (Fig. 1b).[2] The process of minimization of the new objective function (3) is also performed numerically for a certain set of M, Δ_x, and Δ_i values, but the results of our numerical experiment showed that the proposed method is not sensitive with respect to this choice. For this reason, below we use $M = 1$ and set Δ_x and Δ_i values to be the same as those for $\hat{\mathbf{a}}_f$.

Since the chaotic regime can be exhibited only by a nonmonotonic one-dimensional map, the unavoidable problem of a non-single-valued inverse map arises: during iterations in the reverse time, it is necessary to decide which root of the equation $x_{n+1} - f(x, \mathbf{a}) = 0$ has to be selected as x_n (x_{n+1} is the value of the variable obtained in the preceding iteration step in the reverse time). We select the root closest to the corresponding value of the observable η_n. The final "backward" estimate will be denoted $\hat{\mathbf{a}}_b$.

Numerical experiment. The error of estimation of a single parameter $\hat{a}$ is usually determined in mathematical statistics as the square deviation from the true value, $\varepsilon = \langle(\hat{a} - a^{(0)})^2\rangle$, where the angle brackets denote the mathematical expectation. In the case of several parameters ($P > 1$), let ε_i be the error of estimation for $\hat{a}_i$ and ε be the total error defined as $\varepsilon = \sum_{i=1}^{P} \varepsilon_i$.

In the numerical experiment, we calculated the errors ε for the estimates $\hat{\mathbf{a}}_f$ and $\hat{\mathbf{a}}_b$ by averaging over an ensemble of 1000 time series (for a fixed set of $\mathbf{a}^{(0)}$, $x_1^{(0)}$, N, σ_ξ^2). The objective functions (2) and (3) were

[1] The efficiency of the least squares method is related to the fact that it coincides with the maximum likelihood method in the case of a normal noise. However, the results of our numerical experiment (not presented here) show that fitting by least squares also provides sufficiently accurate estimates for other noise distributions.

[2] It should be emphasized that applicability of the proposed method is restricted to one-dimensional maps, since the trajectory of a multidimensional dissipative system in the reverse time is even more sensitive with respect to the parameters, and the objective function (3) has a large number of local minima.

minimized by the quasi-Newtonian method.[3] Then, initial guesses were generated as random values uniformly distributed in the corresponding starting uncertainty intervals.

Estimation of a single parameter. The test was performed for a typical chaotic system representing the quadratic map

$$x_{n+1} = 1 - ax_n^2, \tag{4}$$

with $a = a^{(0)} = 1.85$ and $x_1 = x_1^{(0)} = 0.3$ (the same values as in [11–13, 15]). The length of the time series was $N = 100$. The value of $\hat{a}_f$ was determined for $M = 10$ and the uncertainty intervals $[\eta_n - 0.1, \eta_n + 0.1]$ with respect to x_n and [1.5, 2.0] with respect to a.[4] The task of selecting the length L for a single time series is rather complicated [15] and will not be considered here. We have used an ensemble of time series for preliminarily determining L such that a minimum value of the error ε ($L = 10$, Fig. 2a) was ensured.

Figure 2b shows a comparison of the best forward estimate $\hat{a}_f$ to the backward estimate $\hat{a}_b$. The new method provides for a more accurate estimate provided that the noise level does not exceed the threshold value $\sigma^2_{\xi,thr} \approx 0.019$.[5] Calculation of the new estimate ($\hat{a}_b$) is much faster, since it involves only one starting guess. At a higher nose level, the error of $\hat{a}_b$ rapidly increases as a result of frequent errors in selecting the root of equation during backward iterations.

The results of our experiments showed that the pattern outlined above is retained with increasing length N of the series. The variances of $\hat{a}_f$ and $\hat{a}_b$ estimates depend on N according to the power law $\sigma^2_{\hat{a}} \propto N^{-\alpha}$. For the variance of $\hat{a}_f$, the exponent is approximately the same ($\alpha \approx 1.1$) for any noise level. The variance of the new estimate at a small noise level decreases faster than the variance of $\hat{a}_f$ (e.g., $\alpha \approx 1.7$ for $\sigma^2_\xi = 0.0001$); for a noise level on the order of the threshold, the exponent is approximately the same for both estimates.

[3] Our experiments showed that this method gives the same results as the nonsmooth optimization methods, which are somewhat more effective in the case of rapidly oscillating functions.

[4] The value of M is limited by the computational time, while the starting uncertainty intervals are determined by the lack of a priori information. A considerable growth of M (increasing the segment length L) may provide somewhat better estimates, but the qualitative conclusions will remain the same.

[5] For practical applications, this threshold noise level can be expressed in terms of the percentage signal to noise ratio (with respect to the standard deviation). The "pure" signal variance for system (4) is 0.38. Therefore, a noise variance of 0.01 corresponds to the signal to noise ratio of 16% (which is a quite significant noise).

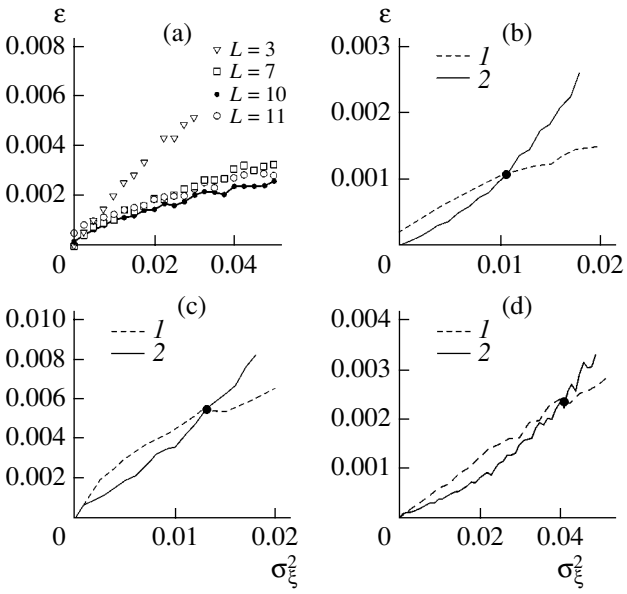

Fig. 2. Plots of the errors of estimated parameters versus noise variance: (a) $\hat{a}_f$ estimates of the parameter a in map (4) for various L, (b) $\hat{a}_f$ ($L = 10$) and $\hat{a}_b$ estimates of the parameter a in map (4); (c) total error of $\hat{\mathbf{a}}_f$, $\hat{\mathbf{a}}_b$ estimates of all the three parameters in map (5); (d) total error of $\hat{a}_{f,1}$ and $\hat{a}_{b,1}$ estimates of the parameter a_1 in map (5); (*1*) in the direct time; (*2*) in the reverse time.

Estimation of three parameters. In order to study the influence of the number of model parameters, we have used the same quadratic map,

$$x_{n+1} = a_1 + a_2 x_n - a_3 x_n^2, \tag{5}$$

but with three unknown parameters. The time series were generated for $a_1^{(0)} = 1.0$, $a_2^{(0)} = 0.0$, $a_3^{(0)} = 1.85$ and the same $x_1^{(0)} = 0.3$. Figure 2c shows the total error of $\hat{\mathbf{a}}_f$ for all three parameters (determined for the optimum segment length $L = 8$ and the uncertainty intervals $a_1 \in [0.8, 1.2]$, $a_2 \in [-0.2, 0.2]$, other parameters being the same as above) and the error of $\hat{\mathbf{a}}_b$. As can be seen, the new estimates obtained for a lower noise level are again more accurate than $\hat{\mathbf{a}}_f$. Moreover, the threshold noise variance is approximately 30% higher ($\sigma^2_{\xi,\mathrm{thr}} \approx 0.013$), which implies expansion of the region where the proposed method is advantageous to the standard approach. The results of estimation of the separate parameters a_2 and a_3 are close to those in Fig. 2c, while the threshold noise variance for a_1 is three times as high ($\sigma^2_{\xi,\mathrm{thr}} \approx 0.043$) (Fig. 2d). Thus, the region of advantageous application of our method increases to an even greater extent in cases when only the parameter a_1 (e.g.,

playing a special role) has to be evaluated with a higher precision.

As the number P of evaluated parameters increases (in practice, this number can frequently be about a dozen), the threshold noise level must grow. At a very large P, the traditional least squares method with iterations in the direct time may fail to be applicable, since the required number of starting guesses may become unreasonably high. In such cases, the proposed method is advantageous irrespective of the noise level.

Conclusions. The procedure of modeling based on the time series always involves the stage of evaluating the system parameters for a selected structure of model equations. In the case of chaotic time series, it might seem that very accurate estimates can be obtained because the model trajectory is sensitive to the values of parameters. However, long chaotic time series hinder the finding of the global minimum of an objective function (the sum of square deviations) because of its complicated "relief" involved in the model map calculations by iterations in the direct time. The time series has to be divided into segments, which makes the estimation procedure less effective.

A new variant of realization of the least squares method proposed in this paper for the reconstruction of one-dimensional maps employs the principle of iteration in the reverse time. This method, which almost eliminates the problem of local minima, ensures faster convergence. In addition, the new method provides much more accurate estimates at a moderate noise level (not exceeding a certain threshold signal to noise ratio, typically on the order of 10%). The greater the number of parameters to be evaluated, the higher the threshold level. Therefore, the proposed approach will be especially useful in practice for constructing multiparametric model maps.

Acknowledgments. This study was supported by the Russian Foundation for Basic Research (project no. 02-02-17578), the US Civilian Research and Development Foundation for Independent States of the Former Soviet Union (CRDF Award No. REG-006), the Presidential Program (project no. MK-1067.2004.2), and the Russian Science Support Foundation.

REFERENCES

1. R. Hegger, H. Kantz, F. Schmuser, *et al.*, Chaos **8**, 727 (1998).
2. I. Swameye, T. G. Muller, J. Timmer, *et al.*, Proc. Natl. Acad. Sci. USA **100**, 1028 (2003).
3. L. Ljung, *System Identification—Theory for the User* (Prentice-Hall, Englewood Cliffs, 1987).
4. V. S. Anishchenko, T. E. Vadivasova, and V. V. Astakhov, *Nonlinear Dynamics of Chaotic and Stochastic Systems* (Saratov. Gos. Univ., Saratov, 1999) [in Russian].
5. G. G. Malinetskiĭ and A. B. Potapov, *Modern Problems of Nonlinear Dynamics* (Editorial URSS, Moscow, 2000) [in Russian].
6. D. A. Smirnov, I. V. Sysoev, E. P. Seleznev, and B. P. Bezruchko, Pis'ma Zh. Tekh. Fiz. **29** (19), 69 (2003) [Tech. Phys. Lett. **29**, 824 (2003)].
7. O. L. Anosov, O. Ya. Butkovskiĭ, and Yu. A. Kravtsov, Radiotekh. Élektron. (Moscow) **42**, 313 (1997).
8. A. M. Feĭgin, Ya. I. Mol'kov, D. N. Mukhin, and E. M. Loskutov, Izv. Vyssh. Uchebn. Zaved., Radiofiz. **44**, 376 (2001).
9. D. Smirnov and B. Bezruchko, Phys. Rev. E **68**, 046209 (2003).
10. S. P. Kuznetsov, *Dynamical Chaos* (Fizmatlit, Moscow, 2001) [in Russian].
11. L. Jaeger and H. Kantz, Chaos **6**, 440 (1996).
12. P. E. McSharry and L. A. Smith, Phys. Rev. Lett. **83**, 4285 (1999).
13. K. Judd, Phys. Rev. E **67**, 026212 (2003).
14. W. Horbelt and J. Timmer, Phys. Lett. A **310**, 269 (2003).
15. V. F. Pisarenko and D. Sornette, Phys. Rev. E **69**, 036122 (2004).
16. J. D. Farmer and J. J. Sidorowich, Physica D **47**, 373 (1991).
17. Yu. V. Andreyev, A. S. Dmitriev, and E. V. Efremova, Phys. Rev. E **65**, 046220 (2002).
18. J. E. Dennis and R. Schnabel, *Numerical Methods for Unconstrained Optimization and Nonlinear Equations* (Prentice-Hall, Englewood Cliffs, N.J., 1983).

Translated by P. Pozdeev